NASA-CR-197102

NUMERICAL STUDY OF THE EFFECTS OF ICING ON VISCOUS FLOW OVER WINGS

NASA Grant NAG-3-768

Final Report

FINAL
IN-02-CR
[illegible]
30465
P. 156

Submitted to

NASA Lewis Research Center
Cleveland, OH 44135

Attn.: Dr. Mark Potapczuk
Icing and Cryogenics Branch

Prepared by

L. N. Sankar
Professor, School of Aerospace Engineering
Georgia Institute of Technology, Atlanta, GA 30332-0150

October 1994

(NASA-CR-197102) NUMERICAL STUDY OF THE EFFECTS OF ICING ON VISCOUS FLOW OVER WINGS Final Report (Georgia Inst. of Tech.) 156 p
N95-14803
Unclas
G3/02 0030465

INTRODUCTION

This report summarizes the progress made under the NASA Grant NAG-3-768 titled "Numerical study of the effects of icing on viscous flow over wings". The work was carried out by Dr. L. N. Sankar, the principal investigator, and Dr. Oh J. Kwon with the assistance of the following graduate research assistants: Mr. Jiunn-Chi Wu, Mr. Ashok Bangalore and Mr. Napporn Phaengsook. Another student, Mr. Olympio Mello, not supported under this project, also contributed to the work reported.

The research effort lead to the development of 2-D and 3-D computational tools for the prediction of viscous flow over iced wings and airfoils. Much of the work has already been published. Here is the list of all the publications, supported by the present grant.

Refereed Publications:

18. Wu, Jiunn-Chi, Huff, D. and Sankar, L.N., "Evaluation of Three Turbulence Models in Static Airloads and Dynamic Stall Predictions," Journal of Aircraft, Vol. 27, No. 4, April 1990, pp382-384.

Invited Conference Keynote Presentation

1. Sankar, L. N., Kwon, O. J., Bangalore, A., Phaengsook, N. and Mello, O., "Effects of Icing on the Performance of Lifting Surfaces," Invited Lecture, Workshop on Aircraft Icing and Transition, Ecole Polytechnique, University of Montreal, Montreal, Canada, September 20-21, 1993.

Conference Presentations with Proceedings (Non-Refereed)

1. Potapczuk, M. G., Bragg, M. B. , Kwon, O. J. and Sankar, L. N., "Simulation of Iced Wing Aerodynamics," Proceedings of the AGARD Conference on Effects of Adverse Weather on Aerodynamics, AGARD CP-496, April 29 - May 1, 1991.

Conference Presentations without Proceedings (Non-Refereed)

1. Wu, Jiunn-Chi, Huff, D. and Sankar, L. N., "A Comparison of Three Turbulence Models for the Prediction of Steady and Unsteady Airloads," AIAA Paper 89-0609.

2. Kwon, O. J. and Sankar, L. N., "Numerical Simulation of the Effects of Icing on the Aerodynamic Characteristics of a Rectangular Wing," AIAA 28th Aerospace Sciences Meeting, Reno, Nevada, January 1990.

3. Kwon, O. J. and Sankar, L. N., "Numerical Study of the Effects of Icing on the Hover Performance of Rotorcraft," AIAA Paper 91-0662, January 1991.

4. Kwon, O. J. and Sankar, L. N., "Numerical Investigation of Performance Degradation of Wings and Rotors due to icing," AIAA Paper 92-0412.

5. Sankar, L. N., Phaengsook, N. and Bangalore, A., "Effects of icing on the Aerodynamic Performance of High Lift Airfoils," AIAA Paper 93-0026.

6. Mello, O. A. F. and Sankar, L. N., "A Hybrid Navier-Stokes/Full Potential Method for the Prediction of Iced Wing Aerodynamics," AIAA Paper 94-0489

7. Bangalore, A., Phaengsook, N. and Sankar, L. N., "Application of a Third Order Upwind Scheme to Viscous Flow over Clean and Iced Wings," AIAA Paper 94-0485.

During the final year of this grant ((January 1, 1994 - December 31, 1994), work was completed on an efficient hybrid procedure that may be used to study clean and iced wing aerodynamics. This work resulted in the Ph. D. dissertation of Mr. Olympio Mello. A draft copy of Mr. Mello's Ph. D. thesis dissertation is enclosed as an appendix. A revised copy of Mr. Mello's dissertation will be mailed to the sponsor in January 1995, after Mr. Mello successfully defends his thesis work.

APPENDIX

An Improved Hybrid Navier-Stokes/Full-Potential Method for Computation of Unsteady Compressible Viscous Flows

A Thesis

Presented to The Academic Faculty

by

Olympio Achilles de Faria Mello

In Partial Fulfillment of the Requirements for the Degree

Doctor of Philosophy in Aerospace Engineering

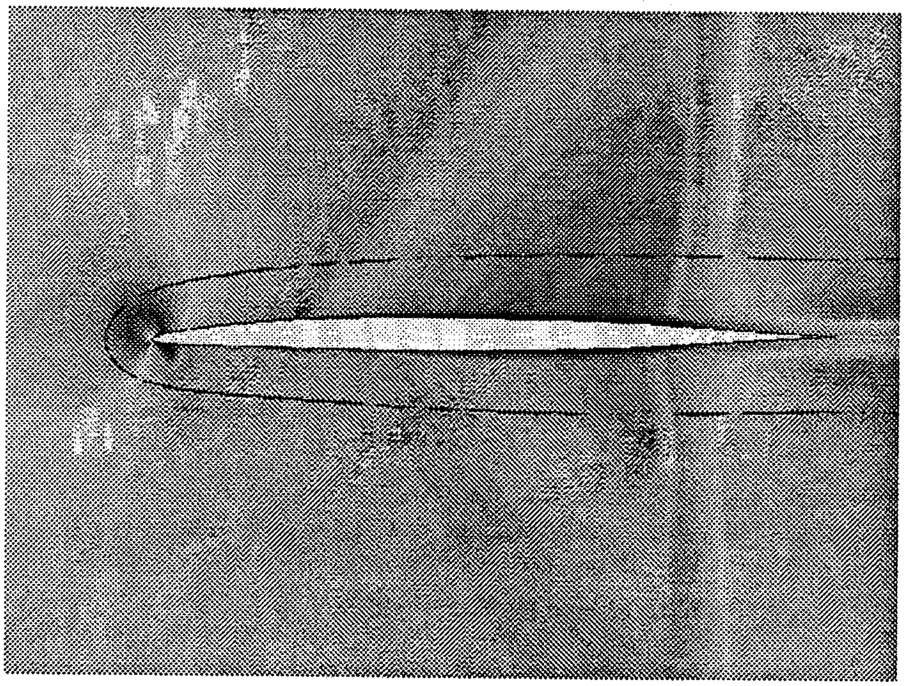

Georgia Institute of Technology

November 1994

An Improved Hybrid Navier-Stokes/Full-Potential Method for Computation of Unsteady Compressible Viscous Flows

A Thesis
Presented to
The Academic Faculty

by

Olympio Achilles de Faria Mello

In Partial Fulfillment
of the Requirements for the Degree
Doctor of Philosophy in Aerospace Engineering

Georgia Institute of Technology

November 1994

TABLE OF CONTENTS

I. INTRODUCTION 1

1.1. Overlook 1

1.2. Unsteady Transonic Flow and Aeroelastic Problems 3

1.3. Historical Perspective 6

1.4. Structure of The Present Work 11

II. NAVIER-STOKES FORMULATION 12

2.1. Mathematical Formulation 12

2.2. Numerical Formulation 15

2.2.1. Discretization 15

2.2.2. Linearization 18

2.2.3. Approximate Factorization 19

2.2.4. Diagonal Form 20

2.2.5. Numerical Dissipation 23

2.2.6. Turbulence Model 24

2.2.7. Numerical Boundary Conditions 26

2.2.7.1. Solid Surface Boundary 27

2.2.7.2. Wing Root Boundary 27

2.2.7.3. Far Field Boundaries 28

III. FULL-POTENTIAL FORMULATION 29

3.1. Mathematical Formulation 29

3.2. Numerical Formulation 32
  3.2.1. Discretization 32
  3.2.2. Density Biasing 35
  3.2.3. Strongly Implicit Procedure 36
  3.2.4. Numerical Boundary Conditions 37
    3.2.4.1. Wing Root Boundary 38
    3.2.4.2. Far Field Boundary 38
IV. NAVIER-STOKES/FULL POTENTIAL COUPLING 42
4.1. Partitioning of Computational Domain 42
4.2. Original Viscous-Inviscid Interface Boundary Conditions 43
4.3. Improved Viscous-Inviscid Interface Boundary Conditions 45
  4.3.1. Interface Boundary Conditions for the Navier-Stokes Solver 46
  4.3.2. Interface Boundary Conditions for the Full-Potential Solver 52
V. RESULTS AND DISCUSSION 54
5.1. Rectangular Wing Study 54
  5.1.1. Configuration 54
  5.1.2. Surface Pressure Distributions 56
  5.1.3. Convergence Histories 63
5.2. F-5 Wing Studies 66
  5.1.1. Configuration 66
  5.2.2. Steady Flow Simulations 69
  5.2.3. Unsteady Flow Simulations 83
VI. CONCLUSIONS AND RECOMMENDATIONS 111
6.1. Conclusions 111
6.2. Recommendations 112

A. APPLICATION OF THE HYBRID NAVIER-STOKES/FULL-POTENTIAL METHOD TO AN ICED WING 115

A.1. Configuration 115

A.2. Surface Pressure Distributions 116

REFERENCES 126

VITA 139

LIST OF TABLES

5.1. Spanwise Stations Where Experimental Data is Available for the F-5 Wing 68
5.2. Test Cases for Unsteady Flow 85

LIST OF ILLUSTRATIONS

Figure

1.1. Partitioning of Computational Domain into Inner and Outer Zones 2

1.2. Mixed Flow Regions in Transonic Flow 4

1.3. Flutter Dynamic Pressure Variation with Mach Number (after Ref. 2) 5

4.1. Partitioning of Computational Domain into Inner and Outer Zones 43

4.2. Waves Contributing to Fluxes at $k = KMATCH$ Interface 46

5.1. Computational Grid for the Rectangular NACA 0012 Wing 55

5.2. Surface Pressure Distributions for the Rectangular Wing at α=4° 58

5.3. Surface Pressure Distributions for the Rectangular Wing at α=8° 60

5.4. Lift Distribution for the Rectangular Wing at α=4 and 8° 63

5.5. Residual Histories in Potential and Navier-Stokes Zones 64

5.6. Residual History in Navier-Stokes Zone with Original and Improved Interface Boundary Conditions (Rectangular Wing at α=4°) 65

5.7. F-5 Wing Experimental Lay-Out 67

5.8. Computational Grid for the F-5 Wing 69

5.9. Steady Surface Pressure Distributions, $M_\infty = 0.6$ 73

5.10. Steady Surface Pressure Distributions, $M_\infty = 0.8$ 74

5.11. Steady Surface Pressure Distributions, $M_\infty = 0.9$ 76

5.12. Steady Surface Pressure Distributions, $M_\infty = 0.95$ 79

5.13. Density Contours at 81.7% Span, $M_\infty = 0.95$ 82

5.14. Nodal Lines for F-5 Pitching Oscillations 86
5.15. Time History of the Lift Coefficient at 64.1% Span, M_∞=0.95, F=40 Hz 88
5.16. Unsteady Surface Pressure Distributions, $M_\infty = 0.6$, f=20 Hz 95
5.17. Unsteady Surface Pressure Distributions, $M_\infty = 0.6$, f=40 Hz 97
5.18. Unsteady Surface Pressure Distributions, $M_\infty = 0.9$, f=40 Hz 99
5.19. Unsteady Surface Pressure Distributions, $M_\infty = 0.95$, f=40 Hz 105
A.1. Simulated Glaze Ice Accretion 116
A.2. Computational Grid for Rectangular Wing with Simulated Glaze Ice Accretion 119
A.3. Surface Pressure Distributions for Iced Wing at α=4° 120
A.4. Surface Pressure Distributions for Iced Wing at α=8° 122
A.5. Lift Distribution for Iced Wing at α=4 and 8° 125

LIST OF SYMBOLS

a	Speed of sound
$\mathbf{A} = \partial\mathbf{E}/\partial\mathbf{Q}$, $\mathbf{C} = \partial\mathbf{G}/\partial\mathbf{Q}$	Flux Jacobian matrices
$\tilde{\mathbf{A}}$, $\tilde{\mathbf{B}}$, $\tilde{\mathbf{C}}$	Jacobian matrices for the small-perturbation Euler equations
$A_1, A_2, A_3, A_4, A_5, A_6$	Auxiliar metric terms, defined in Eq. (3.6)
c	Reference chord
c_1, c_2, c_3, c_4, c_5	Characteristics for small-perturbation Euler equations
c_p (in Prandtl number)	Specific heat at constant pressure
C_P	Pressure coefficient
C_{P_i}	Unsteady pressure coefficient
c_r	Root chord
$\mathbf{D}_e^{n,n+1}$	Explicit fourth order dissipation
e	Total energy
$\mathbf{E}, \mathbf{F}, \mathbf{G}$	Inviscid flux vectors
F	Frequency of oscillations (Hertz)
$\mathbf{I}$	Identity matrix
i, j, k	Indices corresponding to a point in the computational domain
J	Jacobian of the transformation between cartesian and curvilinear coordinates
k (in Prandtl number)	Thermal conductivity

$k = KMATCH$	Computational plane corresponding to the interface between the inner zone and the outer zone
$[L]$, $[U]$	Sparse lower and upper matrices resulting from the approximate factorization in the strongly implicit procedure
ℓ_m	Mixing length
M	Mach number
$[M]$	Matrix of coefficients in FPE solver
$O(\Delta\tau)$	Order of error in finite-difference approximation
p	Pressure
$\mathrm{Pr} = \mu c_p/k$	Prandtl number
$\mathrm{Pr_T} = \mu_\mathrm{T} c_p/k_\mathrm{T}$	Turbulent Prandtl number
q	Total flow speed
$\mathbf{Q}$	Vector of unknown flow properties
R	Riemann invariant
$\mathbf{R}, \mathbf{S}, \mathbf{T}$	Viscous flux vectors
R_5, S_5, T_5	Auxiliar variables for viscous fluxes, given in Eq. (2.7)
$\mathrm{Re} = \rho_\infty a_\infty c/\mu_\infty$	Reynolds number based on the free-stream speed of sound
Re( ),Im( )	Real and imaginary parts of a complex number
T	Temperature
$\mathbf{T}_\xi$, $\mathbf{T}_\zeta$	Eigenvector matrices
u,v,w	Cartesian components of velocity
U,V,W	Contravariant components of velocity
x,y,z	Cartesian coordinates
α	Angle of attack

δ	Difference operator corresponding to standard second-order central difference
$\bar{\delta}$	Difference operator corresponding to half-point central difference
$\delta \mathbf{q}$	Vector of perturbations on the primitive variables
$\partial_\xi(\cdot)$, $\partial(\cdot)/\partial\xi$, $(\cdot)_\xi$	Partial derivative
Δ_ξ , ∇_ξ	Forward and backward difference operators
ε_E	Coefficient of explicit numerical dissipation
ε_I	Coefficient of implicit numerical dissipation
ϕ	Full potential
φ	Perturbation potential
ϕ_1 , ϕ_2, ϕ_3	Auxiliar variables in numerical dissipation
γ	Ratio of specific heats
$\kappa = \omega c / a_\infty$	Reduced frequency
λ	Eigenvalue
Λ_ξ and Λ_ζ	Diagonal matrices of eigenvalues
μ	Viscosity
μ_T	Eddy viscosity
ρ	Density
ξ, η, ζ	Coordinates in curvilinear system
τ	Time
$\tau_{xx}, \tau_{xy}, \tau_{xz}, \tau_{yy}, \tau_{yz}, \tau_{zz}$	Shear stresses
$\omega = 2\pi F$	Frequency of oscillations (rad/sec)
$\lvert\omega\rvert$	Mean vorticity

Subscripts

i,j,k	Indexes denoting a point in the computational grid
T	Turbulent
∞	Conditions at free-stream

Superscripts

n,n+1	Time level
*	Sonic conditions

SUMMARY

An improved hybrid method for computing unsteady compressible viscous flows is presented. This method divides the computational domain into two zones. In the outer zone, the unsteady full-potential equation (FPE) is solved. In the inner zone, the Navier-Stokes equations are solved using a diagonal form of an alternating-direction implicit (ADI) approximate factorization procedure. The two zones are tightly coupled so that steady and unsteady flows may be efficiently solved. Characteristic-based viscous/inviscid interface boundary conditions are employed to avoid spurious reflections at that interface. The resulting CPU times are less than 60% of the required for a full-blown Navier-Stokes analysis for steady flow applications and about 60% of the Navier-Stokes CPU times for unsteady flows in non-vector processing machines. Applications of the method are presented for a rectangular NACA 0012 wing in low subsonic steady flow at moderate and high angles of attack, and for a F-5 wing in steady and unsteady subsonic and transonic flows. Steady surface pressures are in very good agreement with experimental data and are essentially identical to Navier-Stokes predictions. Density contours show that shocks cross the viscous/inviscid interface smoothly, so that the accuracy of full Navier-Stokes equations can be retained with a significant savings in computational time.

CHAPTER I

INTRODUCTION

1.1. Overview

The development of computational fluid dynamics has brought to the industry and research communities a variety of methodologies based on the transonic small disturbance equation (TSD), full-potential equation (FPE), Euler equations and Navier-Stokes equations[1]. TSD- and FPE-based methods have been extensively used to compute complex configurations. These methods, in some cases, have been coupled to interactive boundary layer analyses to allow solution of problems where viscous effects can be included in a limited way.

For problems where substantial separation occurs, the TSD and FPE techniques coupled with interactive boundary-layer analysis are not adequate, since the concept of a boundary layer is no longer applicable. For these cases, Navier-Stokes methods are clearly needed. However, these are still computationally expensive and have seen limited practical use for complete configurations due to this factor. This becomes especially evident for problems where extensive computations are needed, such as the prediction of transonic flutter[2].

The present method is an extension of the work initiated by Sankar et al.[1], who developed a zonal Navier-Stokes/Full-Potential solver, which was subsequently extended to rotors by Tsung and Sankar[3] The approach used here is to solve the Full-Potential Equation in an outer zone, away from solid surfaces and viscous regions, and solve the Navier-Stokes equations in an inner zone, where viscous effects are essential. This approach is schematically illustrated in Fig. 1.1. This results in a highly efficient solver that retains the accuracy of the Navier-Stokes methodology near the solid surface, and the simplicity of a potential flow solver away from solid surfaces.

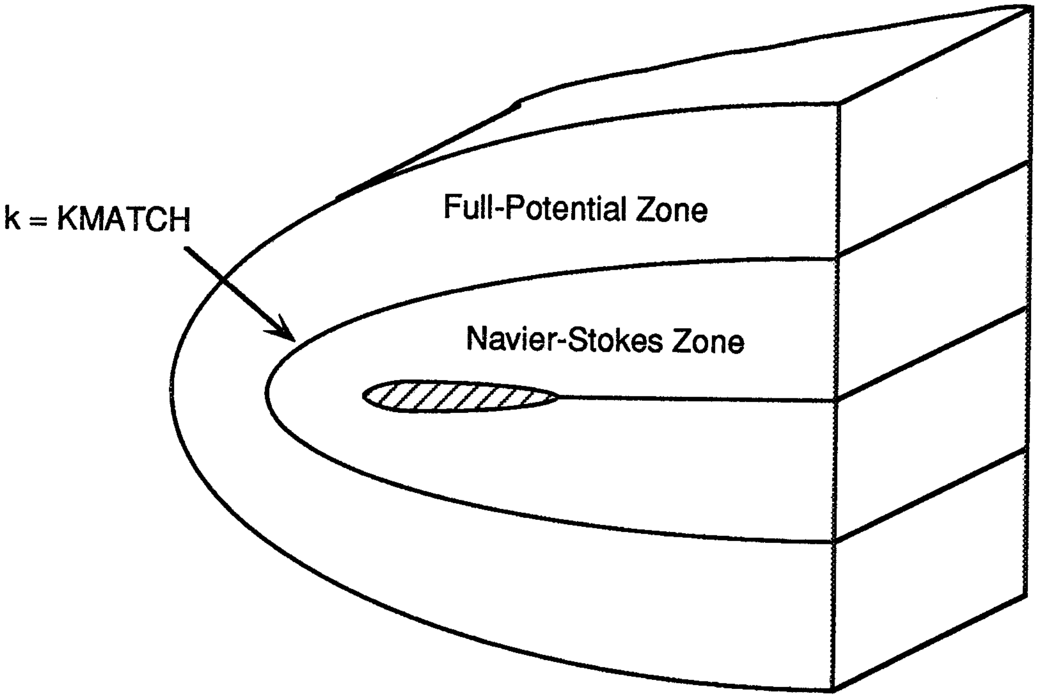

Fig. 1.1: Partitioning of Computational Domain into Inner and Outer Zones.

The Full-Potential solver used in the outer zone solves the unsteady compressible FPE in strong conservation form using the artificial compressibility concept and employing a strongly implicit procedure[4,5]. The Navier-Stokes solver used in the inner zone was developed by Sankar et al. and extensively tested in a variety of problems[6-12]. It employs a diagonal form[13] of an alternating-direction implicit (ADI) approximate factorization procedure[14].

Historically, coupling potential flow to viscous flow via boundary-layer analysis has proved troublesome at the separation point and in the recirculation region. Since we are computing the full Navier-Stokes equations in time-dependent form in the inner region, the above difficulties associated with boundary-layer methods are avoided.

1.2. Unsteady Transonic Flow and Aeroelastic Problems

Transonic flow is characterized by the presence of regions of supersonic flow embedded in a subsonic region, as illustrated in Fig. 1.2. Mathematically, the governing equations are inherently non-linear, a fact that has prevented the application of traditional analytical tools and early numerical methods to the analysis of such a flow condition. In addition, transonic flows tend to be more unsteady and three-dimensional than purely subsonic and supersonic flows[15]. Despite these difficulties, flight in the transonic range is highly desirable for commercial airplanes which achieve their best cruise performance at transonic speeds[16]. This flow regime is also encountered by modern high performance aircraft during maneuvers[17], helicopter rotor blades[18], turbomachinery[19], launch vehicles in their initial stages of flight[20] re-entry bodies at hypersonic speeds and even bluff bodies at subsonic speeds[21].

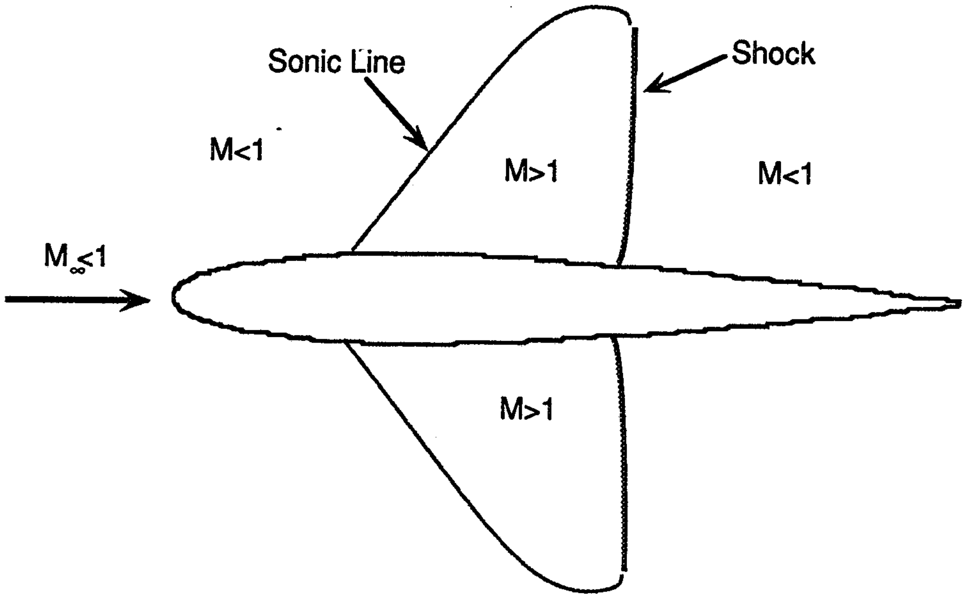

Fig. 1.2: Mixed Flow Regions in Transonic Flow.

In non-steady flow situations, The presence of a supersonic region embedded in a subsonic region causes downstream disturbances to be propagated upstream with a considerable time lag, which results in significant out-of-phase forces.

It has been known for quite some time[22,23] that transonic flow conditions are critical for flutter, with the flutter dynamic pressure being substantially reduced for Mach numbers near unity, in a phenomenon that has been called "transonic dip"[2,24]. This problem is illustrated in Fig. 1.3, from Ref. 2. The severity of flutter at transonic speeds is linked to the presence of moving shock waves over the wing surface[25]. Tijdeman[24,26] identified the following types of shock motion:

- "Sinusoidal Shock-Wave Motion (Type A): The shock moves almost sinusoidally and remains present during the complete cycle of oscillation, although its strength varies. Due to the dynamic effect, phase shifts exist between the model motion and shock position and between shock strength and shock position. The maximum shock strength is not reached during the maximum downstream position of the shock, as in quasi-steady flow, but during its upstream motion.

- Interrupted Shock-Wave Motion (Type B): This motion is similar to Type A, but now the magnitude of the periodic change in shock strength becomes larger than the mean steady shock strength and, as a consequence, the shock wave disappears during a part of its backward motion.

- Upstream-Propagated Shock Waves (Type C): At slightly supercritical Mach number a third type of periodic shock-wave motion is observed, which differs completely from the preceding types. Periodically a shock wave is formed on the upper surface of the airfoil. This shock moves upstream while increasing its strength, The shock wave weakens again, but continues its upstream motion, leaves the airfoil from the leading edge, and propagates upstream into the oncoming flow as a (weak) free shock wave. This phenomenon is repeated periodically and alternates between upper and lower surface."

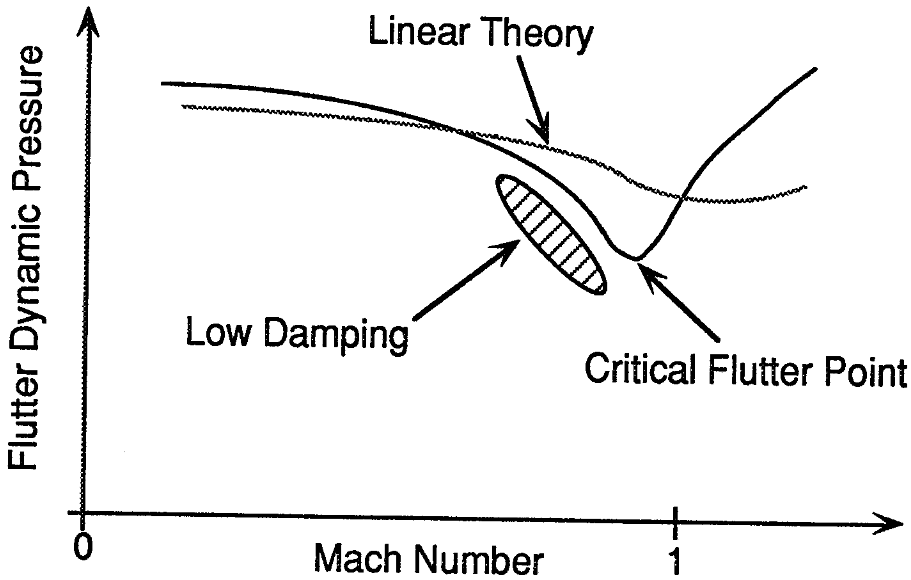

Fig. 1.3: Flutter Dynamic Pressure Variation with Mach Number (after Ref. 2).

From the above considerations, it is clear that accurate flutter predictions depend on the ability of the computational fluid dynamics procedure to predict correct shock strength and location, in a time-accurate fashion. Other aeroelastic problems, such as tail buffet[2,17], are more demanding and require advanced turbulence models, since significant separation is characteristic to this phenomenon.

1.3. Historical Perspective

Numerical computation of unsteady transonic flows has been one of the major challenges to aerodynamicists. Consequently, progress in this area has followed closely the development of Computational Fluid Dynamics (CFD). Reviews of the state of the art have been published every few years[15,27–30,17]. AGARD conferences have been the focus of much of the pertinent work, and they have had specific reviews[31–33].

Early studies on unsteady transonic flow were impractical because of the inherent nonlinearity of that flow range, which prevented the use of the available analytical tools, such as panel and doublet- and vortex-lattice methods[35,36]. So transonic flutter predictions had to rely on experiments[22,34].

The numerical computation of transonic flows was initiated by the pioneering work of Murman and Cole[37], which gave rise to substantial development in methods for solution of the Transonic Small Disturbance (TSD) equation. Early attempts at numerical solution on harmonically oscillating airfoils[38] were obtained in a two-step process, first solving the steady nonlinear problem using the steady transonic small disturbance equation and then solving a linear perturbation equation for small perturbations about this steady solution.

Time-accurate solutions to the TSD equation were obtained by Ballhaus et al.[39,40] This formulation was used by Ballhaus and Goorjian[41] to construct the code LTRAN2, which would later be subsequently improved and heavily used in its various forms. These methodologies proved to be effective, although limited by their restriction to weak shocks and slender bodies.

In parallel to this thrust in numerical methods, experimental investigations by Tijdeman[24] at the NLR in The Netherlands gave new insights into the physics of transonic flow, especially shock motion[21]. Subsequent experimental investigations by Tijdeman et al. at NLR[42–44] and the AGARD standard aeroelastic configurations[45,46] provided essential experimental data to be used in validation of computational fluid dynamics methods. In addition, unsteady aerodynamic data were also published in a compendium form by AGARD[47].

At this time, Euler and Navier-Stokes computations were still too costly, and the unsteady two-dimensional Euler computation performed by Magnus and Yoshihara[48] is noteworthy. An explicit time-marching procedure was used, with two Cartesian (a fine and a coarse) grids and an overlapping body-fitted grid near the airfoil. Another unsteady transonic computation using MacCormack's explicit time-marching procedure for the Euler equations was made by Lerat and Sidès[49].

A new wave of evolution in transonic flow computation came with methods for solution of the two-dimensional Full-Potential Equation (FPE)[50–52] which could handle arbitrary bodies, but were still limited by low transonic Mach numbers. The two-dimensional method of Sankar et al.[51] was subsequently extended to three-dimensions[4,5] in the USIPWING code and applied to unsteady flows past AGARD standard configurations[53] and a F-5 fighter wing[54]. Several improvements were also made in these methods, such as approximate non-reflecting far field boundary conditions[52] and entropy-corrected density biasing[55–59].

The two-dimensional TSD-based code LTRAN2 also benefited from improvements such as approximate non-reflecting far field boundary conditions[60,61] and viscous corrections[62]. At the same time, research at ONERA[63–65] emphasized a strong coupling between unsteady inviscid two-dimensional TSD solutions and integral boundary-layer methods. Meanwhile, LTRAN2 was extended to three dimensions by Borland and Rizzetta[66–68], in what became the XTRAN3S code, to be widely used in the following years[69–72]. Another code which evolved from this formulation was the CAP-TSD (Computational Aeroelasticity Program - Transonic Small Disturbance) code[73–78], which found wide use in the research and industry communities.

Euler methods evolved significantly with the advent of implicit schemes[14,79] which allowed larger time steps. These methods were used by Levy[80, 81] to study transonic buffet, and by Steger and Bailey[82] to study aileron buzz. Sankar et al. presented unsteady three-dimensional computations for fighter wings[83,84] and rotor blades[85]. In that method, artificial dissipation[86] is used for numerical stability. The method was later extended to Navier-Stokes computations about rotor blades[6,87], a fighter aircraft configuration[7,11] and a wing with an oscillatory flap[88]. An upwind differencing capability using Roe's flux-difference splitting[89,90] has been recently included in that code[91,92]. Reductions in CPU times for steady transonic[1] and rotor blade[1,93] flows have been obtained by using the Navier-Stokes/Full-Potential zonal decomposition approach. For unsteady transonic flow, CPU times were also reduced with the application of the GMRES (Generalized Minimum Residual) technique[30,94]

A similar approach for the Euler equations was used by Guruswamy[95]. At NASA Ames, Holst et al.[96–98] extended Pulliam and Steger's ARC3D code[86] to the solution of the thin-layer Navier-Stokes, in a new code called TNS (Transonic Navier-Stokes).

Other two- and three-dimensional Euler/Navier-Stokes methods have been developed using upwind differencing by flux-vector splitting[99,100] and flux-difference splitting[89,90]. Notable examples of the former are the CFL2D and CFL3D finite volume codes developed at NASA Langley by Thomas et al., initially for steady flow[101–103] and later extended to unsteady flows[104,105]. The CFL3D code has been applied to and F/A-18 forebody configuration using a multiple-block approach[106–108].

The unstructured grid approach has received increasing attention in the past several years. These methods can represent virtually any complex geometry and adaptive meshes can be used to obtain local refinement in regions of the flow where gradients are larger. However, they bring additional needs for appropriate data structures[109,110] and grid refinement techniques[110,111]. The mesh generation itself has been the subject of much research[110,112,113]. At NASA Langley, Batina et al.[114–117] have developed an unstructured implicit Euler finite-volume solver for unsteady transonic flow analysis, which has been successfully applied to a NACA 0012 airfoil pitching harmonically and to an ONERA M6 wing and a F/A-18 aircraft configuration[116].

To cope with the larger demands of unsteady Navier-Stokes computations for complex aircraft configurations, as well as to facilitate computation of moving surfaces, zonal structured grid approaches have been recently used[96,118–122]. Among these is the code ENSAERO[120,121], which is in development at NASA Ames for the prediction of aeroelastic responses by simultaneously integrating the Euler/Navier-Stokes equations and the modal structural equations of motion using aeroelastically adaptive grids. These zonal approaches bring up the question of conservative treatment of zonal interfaces[123].

Problems that have received considerable attention in recent research include complete aircraft computations[106–108,116], and delta wing oscillations[124–126]. In the experimental arena, a new development is NASA Langley's Benchmark Aeroelastic Models Program[127], designed to provide well documented data sets for validation of CFD methods.

From the recent work on unsteady transonic flow about complex aircraft configurations, two trends may be identified: First, the research community is developing techniques for solution of the unsteady Navier-Stokes analysis over the complete aircraft, using appropriate approaches to deal with the complex configurations and large computational resources needed, mainly unstructured grids and multi-block structured grids. On the other hand, there is still work to improve the transonic small-disturbance code CAP-TSD[128] which allows practical, fast computations that may be used in the design phase. This latter observation shows the gap between research and practical application in this area: Very complex methods being developed but a much simpler code being actually used. There is clearly a need to bridge the gap, by providing the more realistic representation of the complex Navier-Stokes methods with substantially reduced computational expense. The hybrid Navier-Stokes/Full-Potential method described in this work is an attempt at filling this gap.

1.4. Structure of The Present Work

The remaining of this thesis is organized as follows: First, the mathematical and numerical formulation of the Navier-Stokes and Full-Potential solvers are discussed in Chapters II and III, respectively. Next, the coupling between the FPE and NS solvers is described in Chapter IV. In Chapter V, applications of this method to a rectangular NACA 0012 wing in subsonic steady flow and to a F-5 wing in transonic steady and unsteady flow are discussed. The thesis concludes with an assessment of the hybrid method's prediction capabilities and limitations and recommendations for future work.

CHAPTER II

NAVIER-STOKES FORMULATION

In the present Chapter, the mathematical formulation of the Navier-Stokes equations is presented and subsequently the numerical method is described.

2.1. Mathematical Formulation

The vector form of the full Reynolds-averaged, 3-D Navier-Stokes equations based on an arbitrary curvilinear coordinate system can be written as:

$$\mathbf{Q}_\tau + \mathbf{E}_\xi + \mathbf{F}_\eta + \mathbf{G}_\zeta = \mathbf{R}_\xi + \mathbf{S}_\eta + \mathbf{T}_\zeta \tag{2.1}$$

where **Q** is the vector of unknown flow properties; **E**, **F**, **G** are the inviscid flux vectors; and **R**, **S**, **T** are the viscous flux vectors. Eq. (2.1) may be written in non-dimensional form, using as non-dimensionalization quantities ρ_∞ for density, a_∞ for velocity, c (reference chord) for length, μ_∞ for viscosity, and $\rho_\infty a_\infty^2$ for pressure, as:

$$\mathbf{Q}_\tau + \mathbf{E}_\xi + \mathbf{F}_\eta + \mathbf{G}_\zeta = \frac{1}{\mathrm{Re}}\left(\mathbf{R}_\xi + \mathbf{S}_\eta + \mathbf{T}_\zeta\right) \tag{2.2}$$

where $\mathrm{Re}=\rho_\infty a_\infty c/\mu_\infty$ is the Reynolds number based on the free-stream speed of sound. The resulting non-dimensional flux vectors are:

$$\mathbf{Q}=\frac{1}{J}\left\{\begin{array}{c}\rho\\ \rho u\\ \rho v\\ \rho w\\ e\end{array}\right\}\quad;\quad \mathbf{E}=\frac{1}{J}\left\{\begin{array}{c}\rho U\\ \rho uU+\xi_x p\\ \rho vU+\xi_y p\\ \rho wU+\xi_z p\\ (e+p)U-\xi_t p\end{array}\right\}\quad;\quad \mathbf{F}=\frac{1}{J}\left\{\begin{array}{c}\rho V\\ \rho uV+\eta_x p\\ \rho vV+\eta_y p\\ \rho wV+\eta_z p\\ (e+p)V-\eta_t p\end{array}\right\}\quad;$$

$$\mathbf{G}=\frac{1}{J}\left\{\begin{array}{c}\rho W\\ \rho uW+\zeta_x p\\ \rho vW+\zeta_y p\\ \rho wW+\zeta_z p\\ (e+p)W-\zeta_t p\end{array}\right\}\quad;\quad \mathbf{R}=\frac{1}{J}\left\{\begin{array}{c}0\\ \xi_x\tau_{xx}+\xi_y\tau_{xy}+\xi_z\tau_{xz}\\ \xi_x\tau_{xy}+\xi_y\tau_{yy}+\xi_z\tau_{yz}\\ \xi_x\tau_{xz}+\xi_y\tau_{yz}+\xi_z\tau_{zz}\\ \xi_x R_5+\xi_y S_5+\xi_z T_5\end{array}\right\}\quad;$$

$$\mathbf{S}=\frac{1}{J}\left\{\begin{array}{c}0\\ \eta_x\tau_{xx}+\eta_y\tau_{xy}+\eta_z\tau_{xz}\\ \eta_x\tau_{xy}+\eta_y\tau_{yy}+\eta_z\tau_{yz}\\ \eta_x\tau_{xz}+\eta_y\tau_{yz}+\eta_z\tau_{zz}\\ \eta_x R_5+\eta_y S_5+\eta_z T_5\end{array}\right\}\quad;\quad \mathbf{T}=\frac{1}{J}\left\{\begin{array}{c}0\\ \zeta_x\tau_{xx}+\zeta_y\tau_{xy}+\zeta_z\tau_{xz}\\ \zeta_x\tau_{xy}+\zeta_y\tau_{yy}+\zeta_z\tau_{yz}\\ \zeta_x\tau_{xz}+\zeta_y\tau_{yz}+\zeta_z\tau_{zz}\\ \zeta_x R_5+\zeta_y S_5+\zeta_z T_5\end{array}\right\}\qquad (2.3)$$

where J is the Jacobian of the transformation between Cartesian and curvilinear coordinates, given by:

$$J=\left[y_\xi\left(x_\zeta z_\eta-x_\eta z_\zeta\right)+y_\eta\left(x_\xi z_\zeta-x_\zeta z_\xi\right)+y_\zeta\left(x_\eta z_\xi-x_\xi z_\eta\right)\right]^{-1}\qquad (2.4)$$

U, V and W are the contravariant components of velocity, given by:

$$
\begin{aligned}
U &= \xi_t + \xi_x u + \xi_y v + \xi_z w \\
V &= \eta_t + \eta_x u + \eta_y v + \eta_z w \\
W &= \zeta_t + \zeta_x u + \zeta_y v + \zeta_z w
\end{aligned}
\tag{2.5}
$$

The pressure p is related to the total energy e and kinetic energy by:

$$
p = (\gamma - 1)\left[e - \frac{1}{2}\rho\left(u^2 + v^2 + w^2\right)\right] \tag{2.6}
$$

The shear stresses are given by:

$$
\begin{aligned}
\tau_{xx} &= \mu\left[\frac{4}{3}\left(u_\xi \xi_x + u_\eta \eta_x + u_\zeta \zeta_x\right) - \frac{2}{3}\left(v_\xi \xi_y + v_\eta \eta_y + v_\zeta \zeta_y + w_\xi \xi_z + w_\eta \eta_z + w_\zeta \zeta_z\right)\right] \\
\tau_{xy} &= \mu\left[\left(u_\xi \xi_y + u_\eta \eta_y + u_\zeta \zeta_y\right) + \left(v_\xi \xi_x + v_\eta \eta_x + v_\zeta \zeta_x\right)\right] \\
\tau_{xz} &= \mu\left[\left(u_\xi \xi_z + u_\eta \eta_z + u_\zeta \zeta_z\right) + \left(w_\xi \xi_x + w_\eta \eta_x + w_\zeta \zeta_x\right)\right] \\
\tau_{yy} &= \mu\left[\frac{4}{3}\left(v_\xi \xi_y + v_\eta \eta_y + v_\zeta \zeta_y\right) - \frac{2}{3}\left(u_\xi \xi_x + u_\eta \eta_x + u_\zeta \zeta_x + w_\xi \xi_z + w_\eta \eta_z + w_\zeta \zeta_z\right)\right] \\
\tau_{yz} &= \mu\left[\left(v_\xi \xi_z + v_\eta \eta_z + v_\zeta \zeta_z\right) + \left(w_\xi \xi_y + w_\eta \eta_y + w_\zeta \zeta_y\right)\right] \\
\tau_{zz} &= \mu\left[\frac{4}{3}\left(w_\xi \xi_z + w_\eta \eta_z + w_\zeta \zeta_z\right) - \frac{2}{3}\left(u_\xi \xi_x + u_\eta \eta_x + u_\zeta \zeta_x + v_\xi \xi_y + v_\eta \eta_y + v_\zeta \zeta_y\right)\right]
\end{aligned}
\tag{2.7}
$$

and

$$
\begin{aligned}
R_5 &= u\tau_{xx} + v\tau_{xy} + w\tau_{xz} + \frac{\mu}{\Pr(\gamma - 1)}\left(\xi_x \partial_\xi a^2 + \eta_x \partial_\eta a^2 + \zeta_x \partial_\zeta a^2\right) \\
S_5 &= u\tau_{xy} + v\tau_{yy} + w\tau_{yz} + \frac{\mu}{\Pr(\gamma - 1)}\left(\xi_y \partial_\xi a^2 + \eta_y \partial_\eta a^2 + \zeta_y \partial_\zeta a^2\right) \\
T_5 &= u\tau_{xz} + v\tau_{yz} + w\tau_{zz} + \frac{\mu}{\Pr(\gamma - 1)}\left(\xi_z \partial_\xi a^2 + \eta_z \partial_\eta a^2 + \zeta_z \partial_\zeta a^2\right)
\end{aligned}
\tag{2.8}
$$

where $\Pr = \mu c_p / k$ is the Prandtl number and a is the speed of sound. The notation $\partial_\xi a^2$ is a short form for $\partial(a^2)/\partial\xi$.

In turbulent flows, the molecular viscosity μ appearing in Eqs. (2.7) and (2.8) is replaced by $\mu + \mu_T$, and the quantity $\mu/\Pr$ in Eq. (2.8) is replaced by $\mu/\Pr + \mu_T/\Pr_T$, where μ_T is an eddy viscosity and $\Pr_T$ is the turbulent Prandtl number.

2.2. Numerical Formulation

In this section the finite-difference numerical formulation of the Navier-Stokes equations (2.2) is discussed. First, the finite-difference discretization of the derivatives is described. Next, the linearization of the resulting non-linear system of equations and its approximate factorization into two block-tridiagonal systems of equations are discussed. Finally the numerical implementation is described.

2.2.1. Discretization

The time derivative, $\mathbf{Q}_\tau$, of equation (2.2) is approximated using two-point backward difference at the new time level 'n+1':

$$\mathbf{Q}_\tau = \frac{\mathbf{Q}^{n+1} - \mathbf{Q}^n}{\Delta\tau} + O(\Delta\tau) = \frac{\Delta\mathbf{Q}^{n+1}}{\Delta\tau} + O(\Delta\tau) \tag{2.9}$$

where ‘n’ refers to the time level at which all quantities are known, and ‘n+1’ is the new time level. All spatial derivatives are approximated by standard second-order central differences and are represented by the difference operators δ, e.g.:

$$(\mathbf{E}_\xi)_{i,j,k} = (\delta_\xi \mathbf{E})_{i,j,k} + O(\Delta\xi^2) = \frac{\mathbf{E}_{i+1,j,k} - \mathbf{E}_{i-1,j,k}}{2\Delta\xi} + O(\Delta\xi^2) \tag{2.10}$$

Note that the choice of $\Delta\xi = \Delta\eta = \Delta\zeta = 1$ in the computational space is made for convenience.

The streamwise and normal derivatives, $\mathbf{E}_\xi$ and $\mathbf{G}_\zeta$, are evaluated implicitly at the new time level 'n+1'. The spanwise derivative, $\mathbf{F}_\eta$, is evaluated explicitly at the old time level 'n', but uses the ‘n+1’ values as soon as they become available. Thus, the left side of the discretized form of Eq. (2.2) becomes

$$\frac{\mathbf{Q}^{n+1}_{i,j,k} - \mathbf{Q}^{n}_{i,j,k}}{\Delta\tau} + \frac{\mathbf{E}^{n+1}_{i+1,j,k} - \mathbf{E}^{n+1}_{i-1,j,k}}{2} + \frac{\mathbf{F}^{n}_{i,j+1,k} - \mathbf{F}^{n+1}_{i,j-1,k}}{2} + \frac{\mathbf{G}^{n+1}_{i,j,k+1} - \mathbf{G}^{n+1}_{i,j,k-1}}{2} \tag{2.11}$$

This semi-explicit treatment of the spanwise derivative enables the scheme to solve implicitly for $\Delta\mathbf{Q}^{n+1}$ at all points at a given spanwise station at a time. To eliminate any dependency the solution may have on the sweeping direction, the solver reverses the direction of spanwise sweeping with every sweep, i.e. for every other sweep, Eq. (2.11) is replaced by:

$$\frac{\mathbf{Q}^{n+1}_{i,j,k} - \mathbf{Q}^{n}_{i,j,k}}{\Delta\tau} + \frac{\mathbf{E}^{n+1}_{i+1,j,k} - \mathbf{E}^{n+1}_{i-1,j,k}}{2} + \frac{\mathbf{F}^{n+1}_{i,j+1,k} - \mathbf{F}^{n}_{i,j-1,k}}{2} + \frac{\mathbf{G}^{n+1}_{i,j,k+1} - \mathbf{G}^{n+1}_{i,j,k-1}}{2} \tag{2.12}$$

The viscous terms $\mathbf{R}_\xi$, $\mathbf{S}_\eta$ and $\mathbf{T}_\zeta$ are evaluated explicitly, using half-point central differences denoted here by the difference operator $\bar{\delta}$, so that the computational stencil for the stress terms uses only three nodes in each of the three directions. For example, in the computation of $\mathbf{R}_\xi$, the term $\left(\xi_x^2\mu u_\xi\right)_\xi$ appears and is discretized as follows:

$$\left(\xi_x^2\mu u_\xi\right)_\xi = \bar{\delta}\left(\xi_x^2\mu u_\xi\right) + O\left(\Delta\xi^2\right) = \frac{\left(\xi_x^2\mu u_\xi\right)_{i+1/2,j,k} - \left(\xi_x^2\mu u_\xi\right)_{i-1/2,j,k}}{\Delta\xi} + O\left(\Delta\xi^2\right)$$

$$\approx \frac{\left(\xi_x^2\mu\right)_{i+1/2,j,k}\dfrac{u_{i+1,j,k}-u_{i,j,k}}{\Delta\xi} - \left(\xi_x^2\mu\right)_{i-1/2,j,k}\dfrac{u_{i,j,k}-u_{i-1,j,k}}{\Delta\xi}}{\Delta\xi}$$

$$\approx \frac{\dfrac{\left(\xi_x^2\mu\right)_{i,j,k}+\left(\xi_x^2\mu\right)_{i+1,j,k}}{2}\dfrac{\left(u_{i+1,j,k}-u_{i,j,k}\right)}{\Delta\xi} - \dfrac{\left(\xi_x^2\mu\right)_{i,j,k}+\left(\xi_x^2\mu\right)_{i-1,j,k}}{2}\dfrac{\left(u_{i,j,k}-u_{i-1,j,k}\right)}{\Delta\xi}}{\Delta\xi} \qquad (2.13)$$

$$= \frac{1}{2}\left\{\left[\left(\xi_x^2\mu\right)_{i,j,k}+\left(\xi_x^2\mu\right)_{i+1,j,k}\right]\left(u_{i+1,j,k}-u_{i,j,k}\right) - \left[\left(\xi_x^2\mu\right)_{i,j,k}+\left(\xi_x^2\mu\right)_{i-1,j,k}\right]\left(u_{i,j,k}-u_{i-1,j,k}\right)\right\}$$

Explicit treatment of the stress terms still permits the use of large time steps since the Reynolds numbers of interest here are fairly large.

With the above described time and space discretizations, the discretized form of Eq. (2.2) becomes:

$$\Delta\mathbf{Q}^{n+1} + \Delta\tau\left(\delta_\xi\mathbf{E}^{n+1} + \delta_\eta\mathbf{F}^{n,n+1} + \delta_\zeta\mathbf{G}^{n+1}\right) = \frac{\Delta\tau}{\mathrm{Re}}\left(\bar{\delta}_\xi\mathbf{R}^{n,n+1} + \bar{\delta}_\eta\mathbf{S}^{n,n+1} + \bar{\delta}_\zeta\mathbf{T}^{n,n+1}\right) \qquad (2.14)$$

Note that all viscous terms include η-derivatives, for which known values at the new time level 'n+1' are used, hence the notation $\bar{\delta}_\xi\mathbf{R}^{n,n+1}$.

2.2.2. Linearization

The time and space discretizations described above lead to a system of non-linear, block penta-diagonal matrix equations for the unknown $\Delta\mathbf{Q}^{n+1} = \mathbf{Q}^{n+1} - \mathbf{Q}^{n}$, Eq. (2.14), since the convection fluxes **E**, **F**, **G** are non-linear functions of the vector of unknown flow properties $\mathbf{Q}$. Equation (2.14) is then linearized using the Jacobean matrices $\mathbf{A} = \partial\mathbf{E}/\partial\mathbf{Q}$ and $\mathbf{C} = \partial\mathbf{G}/\partial\mathbf{Q}$, given by:

$$\begin{pmatrix} \mathbf{A} \\ \text{or} \\ \mathbf{C} \end{pmatrix} = \begin{bmatrix} k_t & k_x & k_y & k_z & 0 \\ k_x\phi^2 - u\theta & \Theta - k_x\gamma_2 u & k_y u - k_x\gamma_1 v & k_z u - k_x\gamma_1 w & k_x\gamma_1 \\ k_y\phi^2 - v\theta & k_x v - k_y\gamma_1 u & \Theta - k_y\gamma_2 v & k_z v - k_y\gamma_1 w & k_y\gamma_1 \\ k_z\phi^2 - w\theta & k_x w - k_z\gamma_1 u & k_y w - k_z\gamma_1 v & \Theta - k_z\gamma_2 w & k_z\gamma_1 \\ \theta\left(\phi^2 - b\right) & k_x b - \gamma_1 u\theta & k_y b - \gamma_1 v\theta & k_z b - \gamma_1 w\theta & k_t + \gamma\theta \end{bmatrix} \tag{2.15}$$

where:

$$k = \begin{cases} \xi & \text{for } \mathbf{A} \\ \zeta & \text{for } \mathbf{C} \end{cases} \quad ; \quad \phi^2 = \frac{\gamma - 1}{2}\left(u^2 + v^2 + w^2\right) \quad ; \quad \theta = k_x u + k_y v + k_z w \quad ;$$

$$\Theta = k_t + \theta \quad ; \quad \gamma_1 = \gamma - 1 \quad ; \quad \gamma_2 = \gamma - 2 \quad ; \quad b = \frac{\gamma e}{\rho} - \phi^2 \tag{2.16}$$

The linearization is obtained as follows:

$$\mathbf{E}^{n+1} = \mathbf{E}^{n} + \underbrace{\left(\frac{\partial\mathbf{E}}{\partial\mathbf{Q}}\right)^{n}}_{\mathbf{A}^{n}} \underbrace{\left(\mathbf{Q}^{n+1} - \mathbf{Q}^{n}\right)}_{\Delta\mathbf{Q}^{n+1}} + O\left(\Delta\tau^2\right) = \mathbf{E}^{n} + \mathbf{A}^{n}\Delta\mathbf{Q}^{n+1} + O\left(\Delta\tau^2\right) \tag{2.17}$$

and similarly for $\mathbf{G}^{n+1}$. Applying these linearized flux vectors to Eq. (2.14) yields:

$$\begin{aligned}&\left[\mathbf{I}+\Delta\tau\left(\delta_\xi \mathbf{A}^n+\delta_\zeta \mathbf{C}^n\right)\right]\Delta\mathbf{Q}^{n+1}=\mathbf{RHS}^{n,n+1}\\ &=-\Delta\tau\left(\delta_\xi \mathbf{E}^n+\delta_\eta \mathbf{F}^{n,n+1}+\delta_\zeta \mathbf{G}^n\right)+\frac{\Delta\tau}{\mathrm{Re}}\left(\overline{\delta}_\xi \mathbf{R}^{n,n+1}+\overline{\delta}_\eta \mathbf{S}^{n,n+1}+\overline{\delta}_\zeta \mathbf{T}^{n,n+1}\right)\end{aligned} \tag{2.18}$$

where **I** is the identity matrix.

2.2.3. Approximate Factorization

Eq. (2.18) is a system of linear, block penta-diagonal matrix equations, which is considerably expensive to solve. The approach used here is to employ the approximate factorization of Beam and Warming[14]:

$$\left[\mathbf{I}+\Delta\tau\left(\delta_\xi \mathbf{A}^n+\delta_\zeta \mathbf{C}^n\right)\right]\Delta\mathbf{Q}^{n+1}=\left[\mathbf{I}+\Delta\tau\,\delta_\xi \mathbf{A}^n\right]\left[\mathbf{I}+\Delta\tau\,\delta_\zeta \mathbf{C}^n\right]\Delta\mathbf{Q}^{n+1}+O\left(\Delta\tau^3\right) \tag{2.19}$$

which allows the system of equations (2.18) to be written as:

$$\left[\mathbf{I}+\Delta\tau\,\delta_\xi \mathbf{A}^n\right]\left[\mathbf{I}+\Delta\tau\,\delta_\zeta \mathbf{C}^n\right]\Delta\mathbf{Q}^{n+1}=\mathbf{RHS}^{n,n+1} \tag{2.20}$$

Note that there is no loss of temporal accuracy, because the error incurred due to the approximate factorization is of order $O\left(\Delta\tau^3\right)$. The system of equations (2.20) may now be solved in two steps, each involving only a block-tridiagonal system of equations:

$$\left[\mathbf{I}+\Delta\tau\,\delta_\xi \mathbf{A}^n\right]\Delta\mathbf{Q}^{*n+1}=\mathbf{RHS}^{n,n+1}$$
$$\left[\mathbf{I}+\Delta\tau\,\delta_\zeta \mathbf{C}^n\right]\Delta\mathbf{Q}^{n+1}=\Delta\mathbf{Q}^{*n+1} \tag{2.21}$$

2.2.4. Diagonal Form

The computational work required to solve the systems of equations (2.21) may be reduced by employing the diagonal algorithm of Pulliam and Chaussee[13]. Since the flux Jacobian matrices **A** and **C** have a complete set of eigenvalues and a corresponding set of distinct eigenvectors, the similarity transformations may be used to diagonalize **A** and **C**:

$$\mathbf{A}=\mathbf{T}_\xi \Lambda_\xi \mathbf{T}_\xi^{-1} \quad ; \quad \mathbf{C}=\mathbf{T}_\zeta \Lambda_\zeta \mathbf{T}_\zeta^{-1} \tag{2.22}$$

where the diagonal matrices Λ_ξ and Λ_ζ may be concisely expressed as:

$$\Lambda_\xi=\mathrm{diag}\left[U,U,U,U+a\sqrt{A_1},U-a\sqrt{A_1}\right]$$
$$\Lambda_\zeta=\mathrm{diag}\left[W,W,W,W+a\sqrt{A_6},W-a\sqrt{A_6}\right] \tag{2.23}$$

where $A_1=\xi_x^2+\xi_y^2+\xi_z^2$ and $A_6=\zeta_x^2+\zeta_y^2+\zeta_z^2$. The eigenvector matrices are given by:

$$\mathbf{T}_k =$$

$$\begin{bmatrix} \tilde{k}_x & \tilde{k}_y & \tilde{k}_z & \alpha & \alpha \\ \tilde{k}_x u & \tilde{k}_y u - \tilde{k}_z \rho & \tilde{k}_z u + \tilde{k}_y \rho & \alpha\left(u + \tilde{k}_x a\right) & \alpha\left(u - \tilde{k}_x a\right) \\ \tilde{k}_x v + \tilde{k}_z \rho & \tilde{k}_y v & \tilde{k}_z v - \tilde{k}_x \rho & \alpha\left(v + \tilde{k}_y a\right) & \alpha\left(v - \tilde{k}_y a\right) \\ \tilde{k}_x w - \tilde{k}_y \rho & \tilde{k}_y w + \tilde{k}_x \rho & \tilde{k}_z w & \alpha\left(w + \tilde{k}_z a\right) & \alpha\left(w - \tilde{k}_z a\right) \\ \begin{matrix}\left[\tilde{k}_x \phi^2/\gamma_1 + \right.\\ \left.\rho\left(\tilde{k}_z v - \tilde{k}_y w\right)\right]\end{matrix} & \begin{matrix}\left[\tilde{k}_y \phi^2/\gamma_1 + \right.\\ \left.\rho\left(\tilde{k}_x w - \tilde{k}_z u\right)\right]\end{matrix} & \begin{matrix}\left[\tilde{k}_z \phi^2/\gamma_1 + \right.\\ \left.\rho\left(\tilde{k}_y u - \tilde{k}_x v\right)\right]\end{matrix} & \alpha\left[\frac{\phi^2 + a^2}{\gamma_1} + a\tilde{\theta}\right] & \alpha\left[\frac{\phi^2 + a^2}{\gamma_1} - a\tilde{\theta}\right] \end{bmatrix} \tag{2.24}$$

and

$$\mathbf{T}_k^{-1} =$$

$$\begin{bmatrix} \tilde{k}_x f - \rho^{-1}\left(\tilde{k}_z v - \tilde{k}_y w\right) & \tilde{k}_x u g & \tilde{k}_x v g + \tilde{k}_z \rho^{-1} & \tilde{k}_x w g - \tilde{k}_y \rho^{-1} & -\tilde{k}_x g \\ \tilde{k}_y f - \rho^{-1}\left(\tilde{k}_x w - \tilde{k}_z u\right) & \tilde{k}_y u g - \tilde{k}_z \rho^{-1} & \tilde{k}_y v g & \tilde{k}_y w g + \tilde{k}_x \rho^{-1} & -\tilde{k}_y g \\ \tilde{k}_z f - \rho^{-1}\left(\tilde{k}_y u - \tilde{k}_x v\right) & \tilde{k}_z u g + \tilde{k}_y \rho^{-1} & \tilde{k}_z v g - \tilde{k}_x \rho^{-1} & \tilde{k}_z w g & -\tilde{k}_z g \\ \beta\left(\phi^2 - a\tilde{\theta}\right) & \beta\left(\tilde{k}_x a - \gamma_1 u\right) & \beta\left(\tilde{k}_y a - \gamma_1 v\right) & \beta\left(\tilde{k}_z a - \gamma_1 w\right) & \beta\gamma_1 \\ \beta\left(\phi^2 + a\tilde{\theta}\right) & -\beta\left(\tilde{k}_x a + \gamma_1 u\right) & -\beta\left(\tilde{k}_y a + \gamma_1 v\right) & -\beta\left(\tilde{k}_z a + \gamma_1 w\right) & \beta\gamma_1 \end{bmatrix} \tag{2.25}$$

where

$$\alpha = \frac{\rho}{\sqrt{2}a} \quad ; \quad \beta = \frac{1}{\sqrt{2}\rho a} \quad ; \quad \tilde{k}_{x,y,z} = \frac{k_{x,y,z}}{\sqrt{k_x^2 + k_y^2 + k_z^2}} \quad ;$$

$$\tilde{\theta} = \tilde{k}_x u + \tilde{k}_y v + \tilde{k}_z w \quad ; \quad f = \left(1 - \phi^2/a^2\right) \quad ; \quad g = (\gamma - 1)/a^2 \tag{2.26}$$

Applying the similarity transformations (2.22) to Eq. (2.20) and using the identities $\mathbf{I} = \mathbf{T}_k \mathbf{T}_k^{-1}$ yields:

$$\left[\left(\mathbf{T}_\xi \mathbf{T}_\xi^{-1}\right)^n + \Delta\tau\,\delta_\xi\left(\mathbf{T}_\xi \Lambda_\xi \mathbf{T}_\xi^{-1}\right)^n\right]\left[\left(\mathbf{T}_\zeta \mathbf{T}_\zeta^{-1}\right)^n + \Delta\tau\,\delta_\zeta\left(\mathbf{T}_\zeta \Lambda_\zeta \mathbf{T}_\zeta^{-1}\right)^n\right]\Delta\mathbf{Q}^{n+1} = \mathbf{RHS}^{n,n+1} \tag{2.27}$$

The fundamental simplification of the diagonal algorithm is obtained by moving $\mathbf{T}_\xi$ and $\mathbf{T}_\zeta$ outside the difference operators δ_ξ and δ_ζ, respectively:

$$\mathbf{T}_\xi^n\left[\mathbf{I} + \Delta\tau\,\delta_\xi \Lambda_\xi^n\right]\mathbf{N}^n\left[\mathbf{I} + \Delta\tau\,\delta_\zeta \Lambda_\zeta^n\right]\left(\mathbf{T}_\zeta^{-1}\right)^n \Delta\mathbf{Q}^{n+1} = \mathbf{RHS}^{n,n+1} \tag{2.28}$$

where $\mathbf{N} = \mathbf{T}_\xi^{-1}\mathbf{T}_\zeta$. This simplification introduces and error because $\mathbf{T}_\xi$ and $\mathbf{T}_\zeta$ are functions of (ξ, η, ζ) and cannot be arbitrarily brought in or out the derivatives. It is however believed[13] that the errors introduced are of order $O(\Delta\tau^2)$ and have the effect of making the scheme first order accurate in time, the same order as the previous approximations.

The solution of Eq. (2.28) still involves two block-tridiagonal systems, but now the blocks are diagonal matrices. The solution of Eq. (2.28) is obtained through the following steps:

$$\begin{aligned}
&\left[\mathbf{I} + \Delta\tau\,\delta_\xi \Lambda_\xi^n\right]\Delta\mathbf{Q}^{*n+1} = \left(\mathbf{T}_\xi^{-1}\right)^n \mathbf{RHS}^{n,n+1} \\
&\left[\mathbf{I} + \Delta\tau\,\delta_\zeta \Lambda_\zeta^n\right]\Delta\mathbf{Q}^{**n+1} = \left(\mathbf{N}^{-1}\right)^n \Delta\mathbf{Q}^{*n+1} \\
&\Delta\mathbf{Q}^{n+1} = \mathbf{T}_\zeta^n \Delta\mathbf{Q}^{**n+1}
\end{aligned} \tag{2.29}$$

Note that the interim variables $\Delta\mathbf{Q}^*$ and $\Delta\mathbf{Q}^{**}$ may be stored in the same memory locations as $\Delta\mathbf{Q}$, conserving the available memory.

2.2.5. Numerical Dissipation

The use of standard central differences to approximate the spatial derivatives can give rise to the growth of high frequency errors in the numerical solution with time. To control this growth, a set of 2nd/4th order non-linear, spectral radius based, explicit artificial dissipation terms are added to the discretized equations. A second order implicit dissipation is used to help the overall numerical stability of the scheme[86,129]. The systems of equations in (2.29) are modified as follows:

$$\begin{aligned}&\left[\mathbf{I}+\Delta\tau\,\delta_\xi\Lambda_\xi^n-\Delta\tau\,\varepsilon_I\nabla_\xi\phi_1\Delta_\xi J\right]\Delta\mathbf{Q}^{*n+1}=\left(\mathbf{T}_\xi^{-1}\right)^n\left(\mathbf{RHS}^{n,n+1}-\mathbf{D}_e^{n,n+1}\right)\\&\left[\mathbf{I}+\Delta\tau\,\delta_\zeta\Lambda_\zeta^n-\Delta\tau\,\varepsilon_I\nabla_\zeta\phi_3\Delta_\zeta J\right]\Delta\mathbf{Q}^{**n+1}=\left(\mathbf{N}^{-1}\right)^n\Delta\mathbf{Q}^{*n+1}\end{aligned}\tag{2.30}$$

where ε_I is the coefficient of implicit numerical dissipation, ∇_ξ and Δ_ξ denote backward and forward difference operators, respectively, ϕ_1 and ϕ_3 are defined as:

$$\begin{aligned}(\phi_1)_{i,j,k}&=\left[J^{-1}\left(U+a\sqrt{A_1}\right)\right]_{i+\frac{1}{2},j,k}\left[1+\sqrt{\max\left(\frac{V+a\sqrt{A_4}}{U+a\sqrt{A_1}},\frac{W+a\sqrt{A_6}}{U+a\sqrt{A_1}}\right)_{i+\frac{1}{2},j,k}}\,\right]\\(\phi_3)_{i,j,k}&=\left[J^{-1}\left(W+a\sqrt{A_6}\right)\right]_{i,j,k+\frac{1}{2}}\left[1+\sqrt{\max\left(\frac{U+a\sqrt{A_1}}{W+a\sqrt{A_6}},\frac{V+a\sqrt{A_4}}{W+a\sqrt{A_6}}\right)_{i,j,k+\frac{1}{2}}}\,\right]\end{aligned}\tag{2.31}$$

and $\mathbf{D}_e^{n,n+1}$ is the explicit fourth order dissipation, given by:

$$\mathbf{D}_e^{n,n+1}=\Delta\tau\,\varepsilon_E\left[\nabla_\xi\phi_1\left(\Delta_\xi\nabla_\xi\Delta_\xi\right)+\phi_2\left(\nabla_\eta\Delta_\eta\right)^2+\nabla_\zeta\phi_3\left(\Delta_\zeta\nabla_\zeta\Delta_\zeta\right)\right]J\mathbf{Q}^n\tag{2.32}$$

where ε_E is the coefficient of explicit numerical dissipation and

$$\phi_2 = \frac{1}{2} J^{-1}\left(V + a\sqrt{A_4}\right)\left[1 + \sqrt{\max\left(\frac{U + a\sqrt{A_1}}{V + a\sqrt{A_4}}, \frac{W + a\sqrt{A_6}}{V + a\sqrt{A_4}}\right)}\right] \tag{2.33}$$

For points adjacent to the computational boundaries, second-order explicit dissipation is used instead of Eq. (2.32).

The above described fourth order dissipation may lead to "wiggles" near shocks. To avoid this problem, a switching function based on the second normalized streamwise derivative of pressure

$$\frac{p_{i+1} - 2p_i + p_{i-1}}{\left|p_{i+1} - 2p_i + p_{i-1}\right|}$$

is used to replace the fourth order dissipation with second order dissipation near shocks[130,131].

2.2.6. Turbulence Model

A slightly modified version of the Baldwin-Lomax (B-L) algebraic turbulence model[132] is used, where the maximum shear stress is used instead of the wall shear stress because in the vicinity of separation points, the shear stress values approach zero at the wall.

In this model, two layers are considered; in the inner layer, μ_T is given by:

$$(\mu_T)_{\text{inner layer}} = \rho \ell_m^2 |\omega| \tag{2.34}$$

where $|\omega|$ is the mean vorticity, given by:

$$|\omega| = \sqrt{\left(\frac{\partial w}{\partial y} - \frac{\partial v}{\partial z}\right)^2 + \left(\frac{\partial u}{\partial z} - \frac{\partial w}{\partial x}\right)^2 + \left(\frac{\partial v}{\partial x} - \frac{\partial u}{\partial y}\right)^2} \tag{2.35}$$

and ℓ_m is the mixing length, given by:

$$\ell_m = \kappa d\left[1 - e^{-d_+/A_+}\right] \tag{2.36}$$

where $\kappa = 0.41$ is the von Kármán constant, d is the distance from the wall, $A_+ = 26.0$ is the van Driest constant, and

$$d_+ = d\frac{\sqrt{\rho\, \tau_{\max}}}{\mu_\infty} \tag{2.37}$$

The modification with respect to the original Balwin-Lomax model is apparent in Eq. (2.37), where $\tau_{\max}$ is used instead of τ_{wall}.

In the outer layer, μ_T is given by:

$$(\mu_T)_{\text{outer layer}} = K_C \rho c_1 F_w F_k \tag{2.38}$$

where $K_C = 0.0168$ is Clauser's constant, $c_1 = 1.6$ is an empirical constant, F_w is given by:

$$F_w = \min\left(d_{\max} F_{\max}, 0.25 \frac{d_{\max} U_{\text{dif}}^2}{F_{\max}} \right) \tag{2.39}$$

where

$$F_{\max} = \max\left(\frac{\ell_m \omega}{\kappa} \right) \tag{2.40}$$

$$U_{\text{dif}} = \max\left(\sqrt{u^2 + v^2 + w^2} \right) - \min\left(\sqrt{u^2 + v^2 + w^2} \right) \tag{2.41}$$

and $d_{\max}$ is the distance from the wall where $F_{\max}$ occurs. Also in Eq. (2.38) F_k is given by:

$$F_k = \frac{1}{1 + 5.5 \left(\frac{0.3d}{d_{\max}} \right)^6} \tag{2.42}$$

The switch between inner and outer zones occurs at the distance d_c, defined as the smallest distance from the wall for which $(\mu_T)_{\text{inner layer}} = (\mu_T)_{\text{outer layer}}$, i.e., the values from Eqs. (2.34) and (2.38) are the same.

2.2.7. Numerical Boundary Conditions

The formulation described above must be complemented by appropriate boundary conditions to be specified along the solid surface, Full-Potential/Navier-

Stokes interface, at the wing root, and far field boundaries located outboard of the wing tip and downstream or outflow boundary beyond the wing trailing edge. The boundary conditions to be applied at the Full-Potential/Navier-Stokes interface are discussed in Chapter IV. The remaining boundary conditions are discussed next.

2.2.7.1. Solid Surface Boundary

The solid surface corresponds to the plane $k=1$. The unknown vector in Eq. (2.29), $\Delta\mathbf{Q}$ includes values from $k=2$ to $k=KMATCH$. At the end of each iteration, the new values of $\mathbf{Q}_{i,j,1}$ are computed as follows: Density and pressure are computed from the assumption that their normal derivative at the solid surface is zero, $\partial p/\partial n=\partial\rho/\partial n=0$. This is approximately satisfied on near-orthogonal grids as:

$$\rho_{i,j,1}=\frac{4\rho_{i,j,2}-\rho_{i,j,3}}{3} \qquad p_{i,j,1}=\frac{4p_{i,j,2}-p_{i,j,3}}{3} \tag{2.43}$$

The velocities at the surface are computed from the no-slip condition, i.e.:

$$u_{i,j,1}=(x_\tau)_{i,j,1} \qquad v_{i,j,1}=(y_\tau)_{i,j,1} \qquad w_{i,j,1}=(z_\tau)_{i,j,1} \tag{2.44}$$

2.2.7.2. Wing Root Boundary

The wing root corresponds to the plane $j=1$. The unknown vector in Eq. (2.29), $\Delta\mathbf{Q}$ includes values from $j=2$ to $j=JMAX-1$. The values of $\mathbf{Q}_{i,1,k}$, i.e., at the root, are not updated; when computing the residual $\mathbf{RHS}^{n,n+1}$ at the $j=2$ cell, the fluxes at $j=1$ are computed with the symmetry condition that the contravariant velocity normal to the boundary vanishes, i.e., $V=0$. The pressure values at $j=1$ are computed using zeroth order extrapolation, so that $p_{i,1,k}=p_{i,2,k}$.

2.2.7.3. Far Field Boundaries

The downstream ($i=1$ and $i=IMAX$) and outboard ($j=JMAX$) boundaries are treated in the same way. The velocity normal to the boundary is computed. Then, the boundary conditions are imposed depending on whether it is an inflow or outflow and whether it is subsonic or supersonic:

- Supersonic outflow: all variables are extrapolated from the interior of the domain;
- Subsonic outflow: the pressure is fixed to be the free-stream value and the other variables are extrapolated;
- Subsonic inflow: the density is extrapolated from the interior of the domain and the other variables are fixed from the free-stream;
- Supersonic inflow: all variables are fixed to be the free-stream values.

CHAPTER III

FULL-POTENTIAL FORMULATION

In the present Chapter, the mathematical formulation of the Full-Potential equation is presented and subsequently the numerical method is described. The Full-Potential solver used in the present work was developed by Sankar et al.[4,5,133].

3.1. Mathematical Formulation

The 3-D unsteady compressible potential flow equation, in a body-fitted coordinate system, may be written in a strong conservation form as:

$$\left(\frac{\rho}{J}\right)_\tau + \left(\frac{\rho U}{J}\right)_\xi + \left(\frac{\rho V}{J}\right)_\eta + \left(\frac{\rho W}{J}\right)_\zeta = 0 \tag{3.1}$$

where ρ is density and U, V and W are the contravariant components of velocity, given by:

$$U = \xi_t + \xi_x u + \xi_y v + \xi_z w$$
$$V = \eta_t + \eta_x u + \eta_y v + \eta_z w \qquad (3.2)$$
$$W = \zeta_t + \zeta_x u + \zeta_y v + \zeta_z w$$

and J is the Jacobian of the transformation between Cartesian and curvilinear coordinates, given by:

$$J = \left[y_\xi \left(x_\zeta z_\eta - x_\eta z_\zeta \right) + y_\eta \left(x_\xi z_\zeta - x_\zeta z_\xi \right) + y_\zeta \left(x_\eta z_\xi - x_\xi z_\eta \right) \right]^{-1} \qquad (3.3)$$

In the present formulation, the full potential is denoted by ϕ and the perturbation potential is denoted by φ, i.e.:

$$u = \phi_x = u_\infty + \varphi_x$$
$$v = \phi_y = v_\infty + \varphi_y \qquad (3.4)$$
$$w = \phi_z = w_\infty + \varphi_z$$

It should be noted that the contravariant components of velocity can be expressed in terms of the derivatives of ϕ by substituting (3.4) into (3.2), which yields:

$$U = \xi_t + A_1 \phi_\xi + A_2 \phi_\eta + A_3 \phi_\zeta$$
$$V = \eta_t + A_2 \phi_\xi + A_4 \phi_\eta + A_5 \phi_\zeta \qquad (3.5)$$
$$W = \zeta_t + A_3 \phi_\xi + A_5 \phi_\eta + A_6 \phi_\zeta$$

where

$$\begin{aligned}
A_1 &= \xi_x^2 + \xi_y^2 + \xi_z^2 \\
A_2 &= \xi_x \eta_x + \xi_y \eta_y + \xi_z \eta_z \\
A_3 &= \xi_x \zeta_x + \xi_y \zeta_y + \xi_z \zeta_z \\
A_4 &= \eta_x^2 + \eta_y^2 + \eta_z^2 \\
A_5 &= \eta_x \zeta_x + \eta_y \zeta_y + \eta_z \zeta_z \\
A_6 &= \zeta_x^2 + \zeta_y^2 + \zeta_z^2
\end{aligned} \tag{3.6}$$

In addition to the differential equation (3.1), an additional relation is needed to express the density in terms of the velocity potential and its derivatives (i.e., the velocity components). This additional relation is the isentropic gas law

$$\frac{\rho}{\rho_\infty} = \left(\frac{a^2}{a_\infty^2} \right)^{\frac{1}{\gamma-1}} \tag{3.7}$$

where a is the speed of sound, given by the energy equation:

$$\frac{a^2}{\gamma-1} + \varphi_t + \frac{u^2+v^2+w^2}{2} = \frac{a_\infty^2}{\gamma-1} + \frac{V_\infty^2}{2} \tag{3.8}$$

Note that the derivative φ_t may be expressed in terms of the derivatives with respect to the transformed variables as:

$$\varphi_t = \varphi_\tau + \varphi_\xi \, \xi_t + \varphi_\eta \, \eta_t + \varphi_\zeta \, \zeta_t \tag{3.9}$$

Using Eqs. (3.7) and (3.8), Eq. (3.1) may be written[4] as a second order hyperbolic partial differential equation for φ:

$$\frac{\rho}{a^2 J}\left[\varphi_{\tau\tau}+U\varphi_{\xi\tau}+V\varphi_{\eta\tau}+W\varphi_{\zeta\tau}\right]=\left(\frac{\rho U}{J}\right)_{\xi}+\left(\frac{\rho V}{J}\right)_{\eta}+\left(\frac{\rho W}{J}\right)_{\zeta}+Q \qquad (3.10)$$

where Q is a source term associated with the rate of grid deformation[133], which vanishes for rigid grids and may be neglected for mildly deformed grids, which is the case considered here.

3.2. Numerical Formulation

In this section the finite-difference numerical formulation of the Full-Potential Equation (3.10) is discussed. The spatial flux-like terms appearing on the right hand side of Eq. (3.10) are discretized using standard central differences, which result in formal second-order accuracy in space. The mixed time-space terms appearing on the left hand side are discretized using two-point upwind differences. The temporal derivatives are discretized using two-point backward differences. These discretizations are described in more detail below. For convenience, the mesh spacing $\Delta\xi$, $\Delta\eta$ and $\Delta\zeta$ are set equal to unity in the computational domain.

3.2.1. Discretization

At a given time level n, the disturbance velocity potential φ and its temporal derivative φ_τ are known, and consequently all velocity components, speed of sound and density are also known. Eq. (3.10) is a partial differential equation for φ with nonlinear coefficients. To circumvent the nonlinearities, the coefficients ρ, a^2, J, U, V and W appearing on the left side, and the density ρ appearing on the right side of equation (3.10) are computed at the time level n. The remaining quantities in (3.10) are kept at the new time level $n+1$. In the process of evaluating the contravariant velocities U, V and W, two-point central differences are used to evaluate the derivatives of φ and the transformation metrics at the grid points and locations mid distance between the grid points.

The temporal derivatives on the left hand side of Eq. (3.10) are discretized using two-point backward finite-difference operators, while the mixed time-space terms appearing on the left hand side are discretized using two-point upwind differences. In this respect, the left hand side of Eq. (3.10) is expressed as follows:

$$\left(\frac{\rho}{a^2J}\right)^n_{i,j,k}\left[\overleftarrow{\delta}_\tau\overleftarrow{\delta}_\tau\varphi+U^n\overleftarrow{\delta}_\xi\overleftarrow{\delta}_\tau\varphi+V^n\overleftarrow{\delta}_\eta\overleftarrow{\delta}_\tau\varphi+W^n\overleftarrow{\delta}_\zeta\overleftarrow{\delta}_\tau\varphi\right]_{i,j,k} \tag{3.11}$$

For example, at a typical grid node (i,j,k), the first term inside the square brackets of Eq. (3.11) is expressed as

$$\overleftarrow{\delta}_\tau\overleftarrow{\delta}_\tau\varphi^{n+1}=\frac{\varphi^{n+1}-2\varphi^n+\varphi^{n-1}}{(\Delta\tau)^2}=\frac{\Delta\varphi^{n+1}-\Delta\varphi^n}{(\Delta\tau)^2} \tag{3.12}$$

In the previous expression, $\Delta\varphi$ represents the change in the solution in two consecutive time steps, i.e., $\Delta\varphi^{n+1}=\varphi^{n+1}-\varphi^n$, and $\Delta\varphi^n=\varphi^n-\varphi^{n-1}$. The mixed space-time derivatives appearing in Eq. (3.11) are discretized using upwind-differencing for the spatial derivative, and two-point backward-differencing for the temporal derivative.

For example, in evaluating the second, third and fourth terms, the following expressions are used:

$$
\begin{aligned}
U\bar{\delta}_{\xi}\bar{\delta}_{\tau}\varphi &\equiv \frac{U+|U|}{2\Delta\tau}\left[\frac{\Delta\varphi^{n+1}_{i,j,k}-\Delta\varphi^{n+1}_{i-1,j,k}}{\Delta\xi}\right]+\frac{U-|U|}{2\Delta\tau}\left[\frac{\Delta\varphi^{n+1}_{i+1,j,k}-\Delta\varphi^{n+1}_{i,j,k}}{\Delta\xi}\right]\\
W\bar{\delta}_{\zeta}\bar{\delta}_{\tau}\varphi &\equiv \frac{W+|W|}{2\Delta\tau}\left[\frac{\Delta\varphi^{n+1}_{i,j,k}-\Delta\varphi^{n+1}_{i,j,k-1}}{\Delta\zeta}\right]+\frac{W-|W|}{2\Delta\tau}\left[\frac{\Delta\varphi^{n+1}_{i,j,k+1}-\Delta\varphi^{n+1}_{i,j,k}}{\Delta\zeta}\right]\\
V\bar{\delta}_{\eta}\bar{\delta}_{\tau}\varphi &\equiv \frac{V+|V|}{2\Delta\tau}\left[\frac{\Delta\varphi^{n+1}_{i,j,k}-\Delta\varphi^{n+1}_{i,j-1,k}}{\Delta\eta}\right]+\frac{V-|V|}{2\Delta\tau}\left[\frac{\Delta\varphi^{n+1}_{i,j+1,k}-\Delta\varphi^{n+1}_{i,j,k}}{\Delta\eta}\right]
\end{aligned}
\tag{3.13}
$$

The flux-like terms appearing on the right hand side of Eq. (3.10) are evaluated using two-point central-difference formulas, i.e.,

$$
\begin{aligned}
\left[\left(\frac{\rho U}{J}\right)_{i,j,k}\right]_{\xi} &= \left(\frac{\rho U}{J}\right)_{i+\frac{1}{2},j,k}-\left(\frac{\rho U}{J}\right)_{i-\frac{1}{2},j,k}+O\left(\Delta\xi^{2}\right)\\
\left[\left(\frac{\rho V}{J}\right)_{i,j,k}\right]_{\eta} &= \left(\frac{\rho V}{J}\right)_{i,j+\frac{1}{2},k}-\left(\frac{\rho V}{J}\right)_{i,j-\frac{1}{2},k}+O\left(\Delta\eta^{2}\right)\\
\left[\left(\frac{\rho W}{J}\right)_{i,j,k}\right]_{\zeta} &= \left(\frac{\rho W}{J}\right)_{i,j,k+\frac{1}{2}}-\left(\frac{\rho W}{J}\right)_{i,j,k-\frac{1}{2}}+O\left(\Delta\zeta^{2}\right)
\end{aligned}
\tag{3.14}
$$

The density ρ in Eq. (3.14) is computed at the time level n, while the contravariant components of velocity are computed using mixed information from time level n and the new time level $n+1$, in order to reduce the number of diagonals in the final matrix of coefficients. Recalling Eq. (3.5), the contravariant components are evaluated as follows:

$$\begin{aligned}
U^{n+1} &= \xi_t + A_1\phi_\xi^{n+1} + A_2\phi_\eta^n + A_3\phi_\zeta^n \\
&= \xi_t + A_1\left(\phi_\xi^n + \Delta\varphi_\xi^{n+1}\right) + A_2\phi_\eta^n + A_3\phi_\zeta^n = U^n + A_1\Delta\varphi_\xi^{n+1} \\
V^{n+1} &= \eta_t + A_2\phi_\xi^n + A_4\phi_\eta^{n+1} + A_5\phi_\zeta^n \\
&= \eta_t + A_2\phi_\xi^n + A_4\left(\phi_\eta^n + \Delta\varphi_\eta^{n+1}\right) + A_5\phi_\zeta^n = V^n + A_4\Delta\varphi_\eta^{n+1} \\
W^{n+1} &= \zeta_t + A_3\phi_\xi^n + A_5\phi_\eta^n + A_6\phi_\zeta^{n+1} \\
&= \zeta_t + A_3\phi_\xi^n + A_5\phi_\eta^n + A_6\left(\phi_\zeta^n + \Delta\varphi_\zeta^{n+1}\right) = W^n + A_6\Delta\varphi_\zeta^{n+1}
\end{aligned} \tag{3.15}$$

3.2.2. Density Biasing

In order to maintain numerical stability in regions of supersonic flow, the numerical formulation must be constructed in such a way that it is consistent with the physical domain of dependence. For that purpose, the artificial compressibility method[134] is used. Here, the density values ρ that appear in $(\rho U/J)$ on the right side of equation (3.10) are biased in the direction of the flow using a procedure suggested by Hafez, Whitlow and Osher[57]. First, a function F is defined as:

$$\begin{aligned}
F &= \rho q \quad \text{if } M > 1 \\
F &= \rho^* q^* \quad \text{if } M \leq 1
\end{aligned} \tag{3.16}$$

where the superscript * refers to sonic conditions.

Then the biased density is defined as:

$$\bar{\rho}_{i+\frac{1}{2},j,k} = \rho_{i+\frac{1}{2},j,k} - \frac{F_{i+\frac{1}{2},j,k} - F_{i-\frac{1}{2},j,k}}{q_{i,j,k}} \tag{3.17}$$

where q is the flow speed and M is the Mach number. It is clear from Eqs. (3.16,17) that the biased density reduces to the local density in subsonic flow regions.

3.2.3. Strongly Implicit Procedure

When the above discretizations are employed, at each grid point a linear equation results for the quantity $\Delta\varphi^{n+1} = \varphi^{n+1} - \varphi^{n}$, namely:

$$\begin{aligned} &a^{n}_{i,j,k}\Delta\varphi^{n+1}_{i,j,k-1} + b^{n}_{i,j,k}\Delta\varphi^{n+1}_{i,j-1,k} + c^{n}_{i,j,k}\Delta\varphi^{n+1}_{i-1,j,k} + d^{n}_{i,j,k}\Delta\varphi^{n+1}_{i,j,k} \\ &+ e^{n}_{i,j,k}\Delta\varphi^{n+1}_{i+1,j,k} + f^{n}_{i,j,k}\Delta\varphi^{n+1}_{i,j+1,k} + g^{n}_{i,j,k}\Delta\varphi^{n+1}_{i,j,k+1} = R^{n}_{i,j,k} \end{aligned} \tag{3.18}$$

where the coefficients $a^{n}_{i,j,k}$, $b^{n}_{i,j,k}$, $c^{n}_{i,j,k}$, $d^{n}_{i,j,k}$, $e^{n}_{i,j,k}$, $f^{n}_{i,j,k}$, $g^{n}_{i,j,k}$ and $R^{n}_{i,j,k}$ are functions of the transformation metrics, the contravariant velocities, the density ρ, the speed of sound a, and the time step $\Delta\tau$. Application of Eq. (3.18) at the grid points result in a sparse pentadiagonal matrix system which may be expressed as:

$$[M]\{\Delta\varphi\}^{n+1} = \{R\}^{n} \tag{3.19}$$

A lower-upper (LU) approximate factorization scheme, originally devised by Stone[135], and applied to transonic flows by Sankar, Malone and Tassa[4], is employed to solve the system of equations (3.19) efficiently. In Stone's strongly implicit procedure (SIP), the matrix $[M]$ is approximately factored as the product of two sparse lower

([L]) and upper ([U]) matrices each having four diagonals. Eq. (3.19) can thus be expressed as:

$$[L][U]\{\Delta\varphi\}^{n+1} = \{R\}^n \tag{3.20}$$

where the elements of matrices $[L]$ and $[U]$ are recursively related to the coefficients of the matrix $[M]$[4,133]. The solution to Eq. (3.20) is then obtained using a two-step procedure where we first solve for a temporary solution vector $\{\Delta\varphi^*\}$, i.e.:

$$[L]\{\Delta\varphi^*\} = \{R\}^n \tag{3.21}$$

and next solve for $\{\Delta\varphi\}^{n+1}$:

$$[U]\{\Delta\varphi\}^{n+1} = \{\Delta\varphi^*\} \tag{3.22}$$

It should be noted that the above approximate factorization procedure is applicable to both quasi-steady as well as unsteady flow field solutions. In the former case, the temporal derivatives of the potential function are set equal to zero and the SIP can be regarded as an iterative relaxation procedure. In the latter case, the SIP is regarded as a one-step non-iterative time-accurate marching procedure.

3.2.4. Numerical Boundary Conditions

The formulation described above must be complemented by appropriate boundary conditions to be specified along the Full-Potential/Navier-Stokes interface, at the wing root, and far field boundaries located outboard of the wing tip, outer boundary, downstream or outflow boundary beyond the wing trailing edge. The boundary conditions to be applied at the Full-Potential/Navier-Stokes interface are discussed in Chapter IV. The wing root and far field boundary conditions are discussed next.

3.2.4.1. Wing Root Boundary

The governing equations (3.10) are applied on the $j = 2$ cell as at other interior points. The computational plane $j = 1$ corresponds to the wing root. At this plane of symmetry the contravariant component of velocity V should be zero. As an approximation, this condition is enforced at $j = 2$. Using the expression for V in Eq. (3.5), and the condition $V = 0$, the derivative ϕ_η may be obtained as

$$\phi_\eta = -\frac{\eta_t + A_2\phi_\xi + A_5\phi_\zeta}{A_4} \tag{3.23}$$

After ϕ_η is found, the derivative of the perturbation velocity potential, φ_η is easily computed and the perturbation velocity potential at $j = 1$ is computed from

$$\varphi_{i,1,k} = \varphi_{i,3,k} - 2(\Delta\eta)\left[\varphi_\eta\right]_{i,2,k} \tag{3.24}$$

3.2.4.2. Far Field Boundary

Since the flow is considered to be uniform at a large distance from the wing, the disturbance velocity potential function φ is usually set to zero on all far field boundaries. This condition also implies that the flow velocities in the planes containing these boundaries assume free stream values.

In practice, the computational domain is bounded and the assumption of zero disturbance potential at distances not very far from solid surfaces causes the acoustic waves that carry the perturbation information to be reflected at the outer computational boundary. These reflected waves contaminate the solution and delay convergence[136].

In order to minimize this adverse effect, the far-field boundary conditions derived by Shankar et al.[52] are used at the outer boundary. In this approach, the Riemann invariant R that corresponds to positive characteristics with respect to the inward normal to the boundary is specified. The Riemann invariant may be expressed as:

$$R = -\frac{W}{\sqrt{A_6}} + \frac{2}{\gamma - 1} a \tag{3.25}$$

The actual implementation of this approximate non-reflecting boundary condition is carried out as follows: Let R_∞ be the Riemann invariant corresponding to the undisturbed flow field, i.e.:

$$R_\infty = -\frac{W_\infty}{\sqrt{A_6}} + \frac{2}{\gamma - 1} a_\infty \tag{3.26}$$

The internal solution in the computational domain at a given time level n gives a Riemann invariant $R^n_{i,j,KMAX-1}$ at the point $(i,j,KMAX-1)$. Variations in the values of φ and its derivatives will introduce a variation $\hat{\delta}R$ with respect to $R^n_{i,j,KMAX-1}$. The objective here is to set the values of the perturbation potential φ at the outer boundary so that at each time step the variation that corresponds to these new values of φ is equal to the difference between R_∞ and $R^n_{i,j,KMAX-1}$, i.e.:

$$\hat{\delta}R_{i,j,KMAX-1} = R_\infty - R^n_{i,j,KMAX-1} \tag{3.27}$$

so that the Riemann invariant in the computational domain approaches the far field value. By employing a variational calculation on the expressions of W, Eq. (3.5), and a, Eq. (3.8), and neglecting variations in the tangential derivatives of the potential, $\hat{\delta}\varphi_\xi$ and $\hat{\delta}\varphi_\eta$, the following expression may be obtained for $\hat{\delta}R$:

$$\hat{\delta}R = -\sqrt{A_6}\,\hat{\delta}\varphi_\zeta - \frac{1}{a}\left(W_\infty\hat{\delta}\varphi_\zeta + \hat{\delta}\varphi_t\right) \tag{3.28}$$

The following difference approximations are used:

$$\begin{aligned} \left(\hat{\delta}\varphi_\zeta\right)_{i,j,KMAX} &\approx \Delta\varphi^{n+1}_{i,j,KMAX} - \Delta\varphi^{n+1}_{i,j,KMAX-1} \\ \left(\hat{\delta}\varphi_t\right)_{i,j,KMAX} &\approx \frac{\Delta\varphi^{n+1}_{i,j,KMAX} - \Delta\varphi^{n}_{i,j,KMAX}}{\Delta\tau} \end{aligned} \tag{3.29}$$

It should be noted that the change in notation in Eq. (3.29) from $\hat{\delta}\varphi$ to $\Delta\varphi$ implicitly assumes that the variations in the derivatives are due to the changes in φ as the solution marches in time, since $\Delta\varphi^{n+1} = \varphi^{n+1} - \varphi^{n}$. By applying Eqs. (3.28) and (3.29) in Eq. (3.27), the following expression may be obtained for $\Delta\varphi^{n+1}_{i,j,KMAX}$:

$$\Delta\varphi^{n+1}_{i,j,KMAX} = \frac{1}{1+\Delta\tau\left(W_{\infty}+a\sqrt{A_6}\right)}\left[\Delta\varphi^{n}_{i,j,KMAX} + \Delta\tau\left(W_{\infty}+a\sqrt{A_6}\right) - a\Delta\tau\left(R_{\infty} - R^{n}_{i,j,KMAX-1}\right)\right] \tag{3.30}$$

Eq. (3.30) is used at each time step to update the values of φ at the outer boundary. Similar approaches may be used for the downstream ($i = 1$, $i = IMAX$) and outboard ($j = JMAX$) boundaries. However, in the present work the application of the above described boundary conditions only on the $k = KMAX$ boundary was sufficient to give good convergence characteristics.

CHAPTER IV

NAVIER-STOKES/FULL POTENTIAL COUPLING

4.1. Partitioning of Computational Domain

A typical partitioning of the domain into an inner zone and an outer zone is illustrated in Fig. 4.1. The plane $k = KMATCH$ corresponds to the interface between the inner zone and the outer zone. The Navier-Stokes solver is applied at all planes up to $k = KMATCH$. The FPE solver is applied between the planes $k = KMATCH$ and the outer boundary k-plane. Therefore, the two zones actually overlap, which allows specification of boundary conditions at the interface without extrapolation.

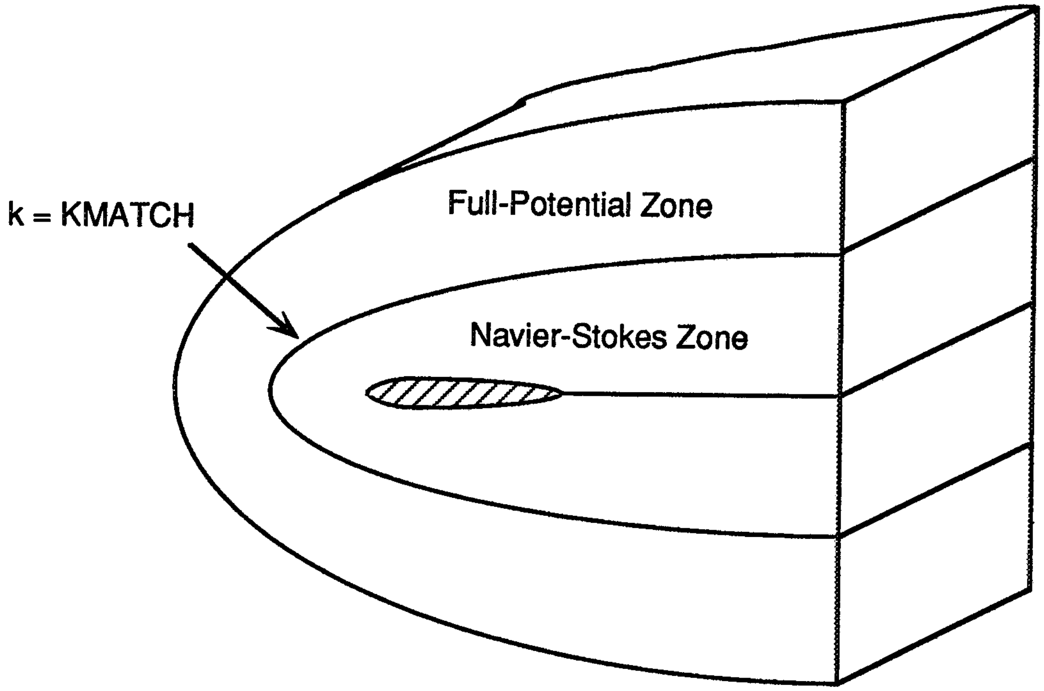

Fig. 4.1: Partitioning of Computational Domain into Inner and Outer Zones.

4.2. Original Viscous-Inviscid Interface Boundary Conditions

In this section, the interface boundary conditions used in the original hybrid scheme[1] are described. The Navier-Stokes solver is applied up to the location $k = KMATCH$. This solver requires the flow properties (density, velocity, pressure) at the plane $KMATCH+1$. These values are obtained through the numerical differentiation of the velocity potential, and the application of the isentropic energy equation:

$$
\begin{aligned}
u &= \phi_\xi \xi_x + \phi_\eta \eta_x + \phi_\zeta \zeta_x \\
v &= \phi_\xi \xi_y + \phi_\eta \eta_y + \phi_\zeta \zeta_y \\
w &= \phi_\xi \xi_z + \phi_\eta \eta_z + \phi_\zeta \zeta_z
\end{aligned}
\tag{4.1}
$$

$$
\frac{T}{T_\infty} = \left(\frac{\rho}{\rho_\infty} \right)^{\gamma - 1}
\tag{4.2}
$$

The full potential solver is applied down to and including the plane $k = KMATCH$. This solver requires the velocity potential at the plane $k = KMATCH - 1$. These values are obtained by matching the normal component of velocity v_n at the plane $k = KMATCH$ from the potential flow and the viscous flow. In terms of the perturbation potential, this is equivalent to matching φ_ζ at $k = KMATCH$ and using the difference formula:

$$
\left(\varphi_\zeta \right)_{i,j,KMATCH} \approx \frac{\varphi_{i,j,KMATCH+1} - \varphi_{i,j,KMATCH-1}}{2}
\tag{4.3}
$$

In order to obtain φ_ζ from the Navier-Stokes solution, the expressions for the contravariant component of velocity W in terms of the primitive variables and perturbation potential are used:

$$
W = \zeta_t + \zeta_x u + \zeta_y v + \zeta_z w
\tag{4.4}
$$

$$
W = \zeta_t + \zeta_x u_\infty + \zeta_y v_\infty + \zeta_z w_\infty + A_3 \varphi_\xi + A_5 \varphi_\eta + A_6 \varphi_\zeta
\tag{4.5}
$$

Eq. (4.4) is used to evaluate W in terms of the primitive variables, obtained from the Navier-Stokes solution at $k = KMATCH$. Using the value of W from Eq. (4.4) and φ_ξ and φ_η from the numerical differentiation of the perturbation potential φ at the previous time level 'n', φ_ζ is obtained from Eq. (4.5) and finally used in Eq. (4.3) to obtain φ at $k = KMATCH - 1$.

4.3. Improved Viscous-Inviscid Interface Boundary Conditions

Previous applications of the hybrid NS/FPE solver to an iced wing configuration[137] with the above interface boundary conditions showed an oscillatory behavior in convergence histories that indicated false reflections from the Navier-Stokes/Full-Potential interface when the boundary conditions where implemented as above. Similar numerical phenomena were observed in the past with respect to far-field boundary conditions: Acoustic waves traveled from the solid surface to the outer boundary and were reflected back to contaminate the solution and delay convergence[136]. The spurious waves responsible for the oscillatory convergence behavior need to be eliminated. In unsteady flows this is even more important since these spurious waves will compromise the time accuracy of the solution.

In the past several years, research has been underway[52,60,61,138–150] to develop and apply non-reflecting far field boundary conditions, which accelerate convergence to steady-state and in some cases improve time accuracy. These boundary conditions would not be directly applicable to the viscous/inviscid interface discussed here because perturbations in one zone must be transmitted to the other zone, as illustrated in Fig. 4.2. The disturbances in the inner region should contribute to the outgoing waves only, while the disturbances in the outer region should contribute to the ingoing waves only, so that there is no reflection at the interface.

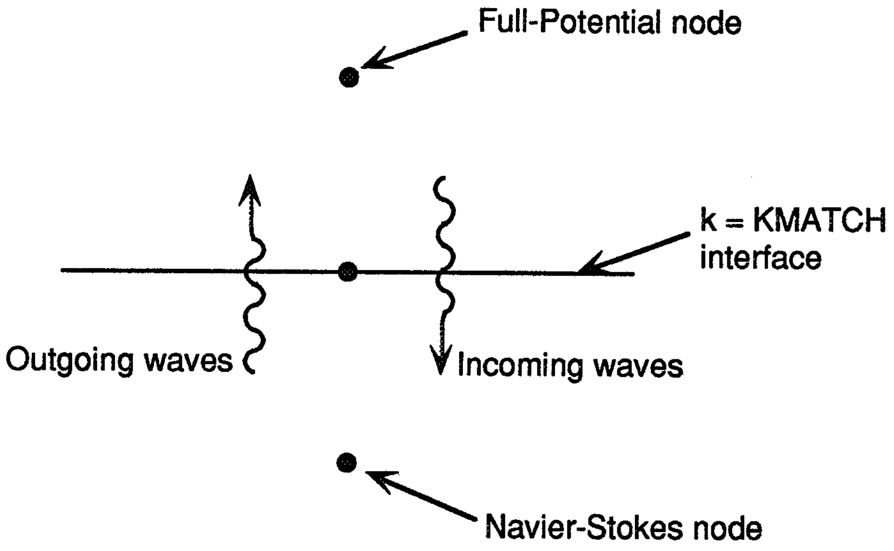
Full-Potential node
k = KMATCH interface
Outgoing waves
Incoming waves
Navier-Stokes node

Fig. 4.2: Waves Contributing to Fluxes at $k = KMATCH$ Interface.

4.3.1. Interface Boundary Conditions for the Navier-Stokes Solver

Following a development analogous to Giles' derivation of approximate non-reflecting boundary conditions[148], a set of characteristics normal to a ζ=constant surface was obtained as follows: First, the vector form of the 3-D Euler equations based on an arbitrary curvilinear coordinate system can be written as:

$$\mathbf{Q}_\tau + \mathbf{E}_\xi + \mathbf{F}_\eta + \mathbf{G}_\zeta = 0 \tag{4.6}$$

where **Q** is the vector of unknown flow properties; **E**, **F**, **G** are the inviscid flux vectors. These vectors are given in Eq. (2.3) and are repeated here for convenience:

$$\mathbf{Q}=\frac{1}{J}\begin{Bmatrix}\rho\\ \rho u\\ \rho v\\ \rho w\\ e\end{Bmatrix} \quad ; \quad \mathbf{E}=\frac{1}{J}\begin{Bmatrix}\rho U\\ \rho uU+\xi_x p\\ \rho vU+\xi_y p\\ \rho wU+\xi_z p\\ (e+p)U-\xi_t p\end{Bmatrix} \quad ;$$

$$\mathbf{F}=\frac{1}{J}\begin{Bmatrix}\rho V\\ \rho uV+\eta_x p\\ \rho vV+\eta_y p\\ \rho wV+\eta_z p\\ (e+p)V-\eta_t p\end{Bmatrix} \quad ; \quad \mathbf{G}=\frac{1}{J}\begin{Bmatrix}\rho W\\ \rho uW+\zeta_x p\\ \rho vW+\zeta_y p\\ \rho wW+\zeta_z p\\ (e+p)W-\zeta_t p\end{Bmatrix} \tag{4.7}$$

Next, small perturbations on the primitive variables are considered. Let the vector of perturbations on the primitive variables be denoted by $\delta\mathbf{q}$, where:

$$\delta\mathbf{q}=\left[\delta\rho \quad \delta u \quad \delta v \quad \delta w \quad \delta p\right]^T \tag{4.8}$$

Then the small perturbation form of the Euler equations (4.6) is given by:

$$\delta\mathbf{q}_\tau+\tilde{\mathbf{A}}\,\delta\mathbf{q}_\xi+\tilde{\mathbf{B}}\,\delta\mathbf{q}_\eta+\tilde{\mathbf{C}}\,\delta\mathbf{q}_\zeta=0 \tag{4.9}$$

where $\tilde{\mathbf{A}}$, $\tilde{\mathbf{B}}$, and $\tilde{\mathbf{C}}$ are Jacobian matrices for the small perturbations. Here, the purpose is to construct a set of characteristics normal to a ζ=constant surface, therefore tangential variations are neglected, and consequently Eq. (4.9) is reduced to:

$$\delta\mathbf{q}_\tau + \tilde{\mathbf{C}}\,\delta\mathbf{q}_\zeta = 0 \tag{4.10}$$

where

$$\tilde{\mathbf{C}} = \begin{bmatrix} W & \rho\zeta_x & \rho\zeta_y & \rho\zeta_z & 0 \\ 0 & W & 0 & 0 & \dfrac{\zeta_x}{\rho} \\ 0 & 0 & W & 0 & \dfrac{\zeta_y}{\rho} \\ 0 & 0 & 0 & W & \dfrac{\zeta_z}{\rho} \\ 0 & \gamma p\zeta_x & \gamma p\zeta_y & \gamma p\zeta_z & W \end{bmatrix} \tag{4.11}$$

The matrix $\tilde{\mathbf{C}}$ has five eigenvalues: $\lambda_1 = \lambda_2 = \lambda_3 = W$, $\lambda_4 = W - a\sqrt{A_6}$, and $\lambda_5 = W + a\sqrt{A_6}$, where A_6 is given in Eq. (3.6). The five characteristics corresponding to the hyperbolic system (4.10) are constructed by applying the similarity transformation:

$$\tilde{\mathbf{C}} = \tilde{\mathbf{T}}_\zeta \Lambda_\zeta \tilde{\mathbf{T}}_\zeta^{-1} \tag{4.12}$$

Applying (4.12) to (4.10) and left-multiplying the result with $\tilde{\mathbf{T}}_\zeta^{-1}$ the characteristic equations are obtained:

$$\mathbf{c}_\tau + \Lambda_\zeta \mathbf{c}_\zeta = 0 \tag{4.13}$$

where $\mathbf{c} = \tilde{\mathbf{T}}_\zeta^{-1}\delta\mathbf{q}$, i.e.:

$$\begin{Bmatrix} c_1 \\ c_2 \\ c_3 \\ c_4 \\ c_5 \end{Bmatrix} = \begin{bmatrix} 0 & -\frac{\zeta_x\zeta_z}{A_6} & -\frac{\zeta_y\zeta_z}{A_6} & \frac{\zeta_x^2+\zeta_y^2}{A_6} & 0 \\ 0 & -\frac{\zeta_x\zeta_y}{A_6} & \frac{\zeta_x^2+\zeta_z^2}{A_6} & -\frac{\zeta_y\zeta_z}{A_6} & 0 \\ 1 & 0 & 0 & 0 & -\frac{1}{a^2} \\ 0 & -\frac{\rho a\zeta_x}{2\sqrt{A_6}} & -\frac{\rho a\zeta_y}{2\sqrt{A_6}} & -\frac{\rho a\zeta_z}{2\sqrt{A_6}} & \frac{1}{2} \\ 0 & \frac{\rho a\zeta_x}{2\sqrt{A_6}} & \frac{\rho a\zeta_y}{2\sqrt{A_6}} & \frac{\rho a\zeta_z}{2\sqrt{A_6}} & \frac{1}{2} \end{bmatrix} \begin{Bmatrix} \delta\rho \\ \delta u \\ \delta v \\ \delta w \\ \delta p \end{Bmatrix} \tag{4.14}$$

The integration of Eq. (4.13) to obtain the characteristics c_1 to c_5 is performed according to the signs of the corresponding eigenvalues, for example if $\lambda_4 > 0$ then c_4 is computed using information from the inner zone, otherwise it is computed using information from the outer zone. This corresponds to the eigenvalue splitting $\Lambda_\zeta = \Lambda_\zeta^+ + \Lambda_\zeta^-$ and corresponding characteristic splitting $\mathbf{c} = \mathbf{c}^+ + \mathbf{c}^-$. Then Eq. (4.13) becomes:

$$\mathbf{c}_\tau^+ + \Lambda_\zeta^+ \mathbf{c}_\zeta^+ = 0 \tag{4.15a}$$

$$\mathbf{c}_\tau^- + \Lambda_\zeta^- \mathbf{c}_\zeta^- = 0 \tag{4.15b}$$

The integration of Eq. (4.15a) is discussed next. For convenience, one scalar equation is treated. Let c_k^+ denote the characteristic at the k plane being calculated (the subscripts i, j are dropped to shorten the notation). The discretization of the scalar form of Eq. (4.15a) is made as:

$$\frac{(c_k^+)^{\text{new}} - (c_k^+)^{\text{old}}}{\Delta\tau} + \lambda^+ \frac{(c_k^+)^{\text{new}} - (c_{k-1}^+)^{\text{NS}}}{\Delta\zeta} = 0 \tag{4.16}$$

where $(c_{k-1}^+)^{\text{NS}}$ is the characteristic given by the Navier-Stokes solver at the $k-1$ plane. Considering that the linearization (4.9) is performed about the previous time step, then $(c_k^+)^{\text{old}} = 0$ and Eq. (4.16) can be solved for $(c_k^+)^{\text{new}}$ as:

$$(c_k^+)^{\text{new}} = \frac{\lambda^+ \Delta\tau}{\lambda^+ \Delta\tau + 1} (c_{k-1}^+)^{\text{NS}} \tag{4.17}$$

The integration of Eq. (4.15b) is performed in an analogous fashion. The discretization of the scalar form of Eq. (4.15b) is made as:

$$\frac{(c_k^-)^{\text{new}} - (c_k^-)^{\text{old}}}{\Delta\tau} + \lambda^- \frac{(c_{k+1}^-)^{\text{FP}} - (c_k^-)^{\text{new}}}{\Delta\zeta} = 0 \tag{4.18}$$

where $(c_{k+1}^-)^{\text{FP}}$ is the characteristic given by the Full-Potential solver at the $k+1$ plane. Again, considering $(c_k^-)^{\text{old}} = 0$, Eq. (4.18) can be solved for $(c_k^-)^{\text{new}}$ as:

$$(c_k^-)^{\text{new}} = \frac{\lambda^- \Delta\tau}{\lambda^- \Delta\tau - 1} (c_{k+1}^-)^{\text{FP}} \tag{4.19}$$

For steady flows, it has been found that slightly higher convergence rates may be obtained by taking the limit as $\Delta\tau \to \infty$ in Eqs. (4.17) and (4.19), i.e.:

$$\left(c_k^+\right)^{\text{new}} = \left(c_{k-1}^+\right)^{\text{NS}} \tag{4.20a}$$

$$\left(c_k^-\right)^{\text{new}} = \left(c_{k+1}^-\right)^{\text{FP}} \tag{4.20b}$$

For unsteady flows, numerical experimentation has shown that using the unsteady form, Eqs. (4.17) and (4.19), does not yield better correlations between the computed and experimental results. Therefore, the steady form, Eqs. (4.20), was used also for unsteady flow cases. Further studies are needed to clarify whether the explicit time integration of Eqs. (4.15) is consistent with the implicit Navier-Stokes and Full-Potential solvers used in the present work.

With the resulting values of c_1 to c_5, the changes in flow properties at the interface are computed using the inverse of Eq. (4.14):

$$\begin{Bmatrix} \delta\rho \\ \delta u \\ \delta v \\ \delta w \\ \delta p \end{Bmatrix} = \begin{bmatrix} 0 & 0 & 1 & \dfrac{1}{a^2} & \dfrac{1}{a^2} \\ -\dfrac{\zeta_z}{\zeta_x} & -\dfrac{\zeta_y}{\zeta_x} & 0 & -\dfrac{\zeta_x}{\rho a\sqrt{A_6}} & \dfrac{\zeta_x}{\rho a\sqrt{A_6}} \\ 0 & 1 & 0 & -\dfrac{\zeta_y}{\rho a\sqrt{A_6}} & \dfrac{\zeta_y}{\rho a\sqrt{A_6}} \\ 1 & 0 & 0 & -\dfrac{\zeta_z}{\rho a\sqrt{A_6}} & \dfrac{\zeta_z}{\rho a\sqrt{A_6}} \\ 0 & 0 & 0 & 1 & 1 \end{bmatrix} \begin{Bmatrix} c_1 \\ c_2 \\ c_3 \\ c_4 \\ c_5 \end{Bmatrix} \tag{4.21}$$

4.3.2. Interface Boundary Conditions for the Full-Potential Solver

From the last two equations in Eq. (4.14):

$$\begin{aligned} c_4 &= -\frac{\rho a}{2\sqrt{A_6}}\left(\zeta_x \delta u + \zeta_y \delta v + \zeta_z \delta w\right) + \frac{1}{2}\delta p = -\frac{\rho a}{2\sqrt{A_6}}\delta W + \frac{1}{2}\delta p \\ c_5 &= \frac{\rho a}{2\sqrt{A_6}}\left(\zeta_x \delta u + \zeta_y \delta v + \zeta_z \delta w\right) + \frac{1}{2}\delta p = \frac{\rho a}{2\sqrt{A_6}}\delta W + \frac{1}{2}\delta p \end{aligned} \tag{4.22}$$

Using

$$p = \frac{1}{\gamma}\left(a^2\right)^{\frac{\gamma}{\gamma-1}} \Rightarrow \delta p = \frac{2\rho a}{\gamma-1}\delta a \tag{4.23}$$

yields:

$$\begin{aligned} c_4 &= -\frac{\rho a}{2\sqrt{A_6}}\delta W + \frac{\rho a}{\gamma-1}\delta a \\ c_5 &= \frac{\rho a}{2\sqrt{A_6}}\delta W + \frac{\rho a}{\gamma-1}\delta a \end{aligned} \tag{4.24}$$

By multiplying Eq. (4.24) by $2/\rho a$ the Riemann invariants are recovered, i.e., the characteristic invariants may be expressed as:

$$\begin{aligned} R_1 &= -\frac{\delta W}{\sqrt{A_6}} + \frac{2}{\gamma-1}\delta a \\ R_2 &= \frac{\delta W}{\sqrt{A_6}} + \frac{2}{\gamma-1}\delta a \end{aligned} \tag{4.25}$$

The first characteristic corresponds to the eigenvalue $\lambda_4 = W - a\sqrt{A_6}$, and the second to $\lambda_5 = W + a\sqrt{A_6}$. The Riemann invariants are computed according to the signs of the corresponding eigenvalues, for example if $\lambda_4 > 0$ then R_1 is computed using information from the inner zone, otherwise it is computed using information from the outer zone. With the resulting values of R_1 and R_2, the changes in flow properties at the interface are computed using the inverse of Eq. (4.25).

As shown in Chapter V, the above procedure has been successful in suppressing the oscillatory behavior observed in the computations with the original boundary conditions. Although the procedure is strictly valid only for steady flows, it was used also for unsteady flows with results similar to those obtained by full Navier-Stokes computations, as discussed in Chapter V.

CHAPTER V

RESULTS AND DISCUSSION

In the present Chapter, applications of the hybrid Navier-Stokes/Full-Potential Method are discussed. First, the application of the method to a rectangular wing in steady flow is presented. Next, the application to an F-5 wing in steady and unsteady flow for both subsonic and transonic flow is presented. The method was also applied to a rectangular wing with a simulated glaze ice accretion in subsonic flow, and the corresponding results are presented in Appendix A for completeness.

5.1. Rectangular Wing Study

5.1.1. Configuration

The hybrid Navier-Stokes/Full-Potential Method has been applied to a rectangular wing of aspect ratio 2.5. The airfoil section was NACA 0012. This configuration has been experimentally studied by Bragg et al.[151–153] as part of their iced wing studies. The surface pressures were measured at five spanwise stations: 17%, 34%, 50%, 66% and 85% of the wing semi-span. The wind tunnel had a 0.85m by 1.22m rectangular cross section. The model semi-span was 0.95m.

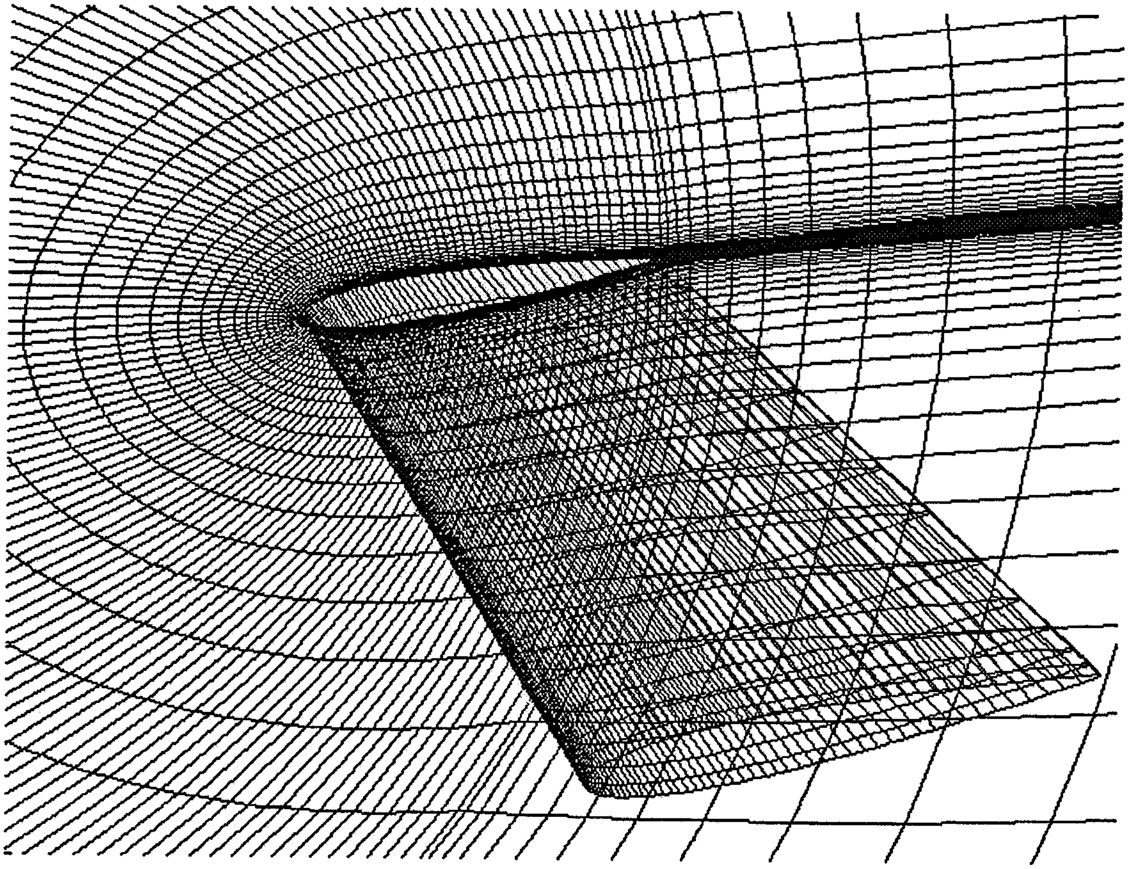

Fig. 5.1: Computational Grid for the Rectangular NACA 0012 Wing.

The computational grid used in the present study, illustrated in Fig. 5.1, was an algebraic C-grid with 141 × 19 × 41 grid points, with 121 points over the airfoil surface at each spanwise station. 14 spanwise stations were used along the wing, with 5 stations extending beyond the tip. The Navier-Stokes and Full-Potential solvers were interfaced at KMATCH=20, so that about half of the number of points are located in each zone. The Mach number was 0.12, the Reynolds number 1.5 million, and the angles of attack were 4° and 8°. The CPU time for this configuration was about 13.6 sec. per iteration on a Hewlett-Packard Apollo 700 workstation. This time was about 60% of the time required for a full Navier-Stokes analysis. The CPU time for the same configuration on Georgia Tech's Cray Y-MP/E was about 4.5 sec. per iteration. This time was about 68% of the time required for a full Navier-Stokes analysis. It was observed that the Navier-Stokes module vectorized better than the Full-Potential module, therefore the computational savings on a vector processor were lower.

5.1.2. Surface Pressure Distributions

The pressure coefficient distributions for angles of attack of 4° and 8° are shown in Figs. 5.2 and 5.3, respectively. The small spurious peaks near the trailing edge at all the spanwise stations are due to inadequate grid resolution in that region, where the chordwise spacing was about 4%, and may be improved with a clustered grid. Outside the trailing edge region, a very good agreement may be observed for the case α=4°, with the possible exception of station 85%. The discrepancies at that station may be due to the tapering of the grid outboard of the wing tip, and better results could be obtained with a finer grid near the tip. In Fig. 5.3, corresponding to the case α=8°, the results obtained from full Navier-Stokes computations are shown for comparison. For this case, an underprediction of the suction peak is noticeable. It can be observed that the underprediction of the suction peak for the case α=8° also occurs for the full Navier-Stokes computations. It should be noted that the experimental results used here were obtained with a small clearance between the upper and lower wind-tunnel walls and the wing surface. Consequently, wind-tunnel wall interference may partially account for the underprediction of the suction peaks.

Further insight can be obtained by analyzing the lift coefficient distribution along the span, shown in Fig. 5.4. The underprediction of lift can be clearly noticed in this figure. Overall, it is observed that our current results correlate well with experiments and are consistent with those obtained by a full Navier-Stokes code[8–10], while consuming only about 60% of the CPU time.

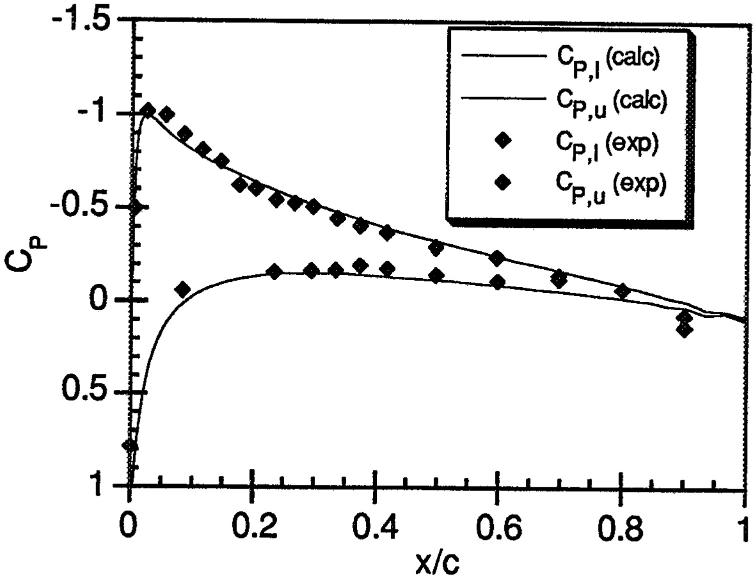

(a) 17% Span

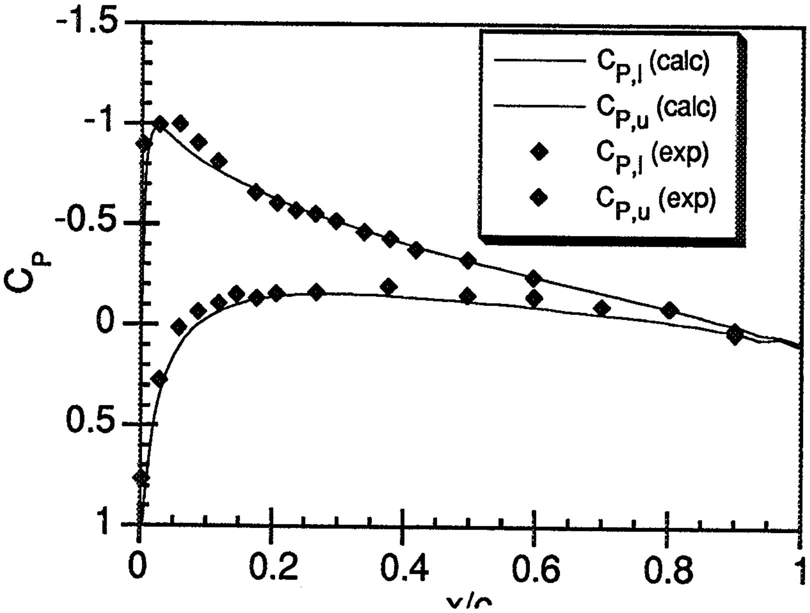

(b) 34% Span

Fig. 5.2: Surface Pressure Distributions for the Rectangular Wing at α=4°

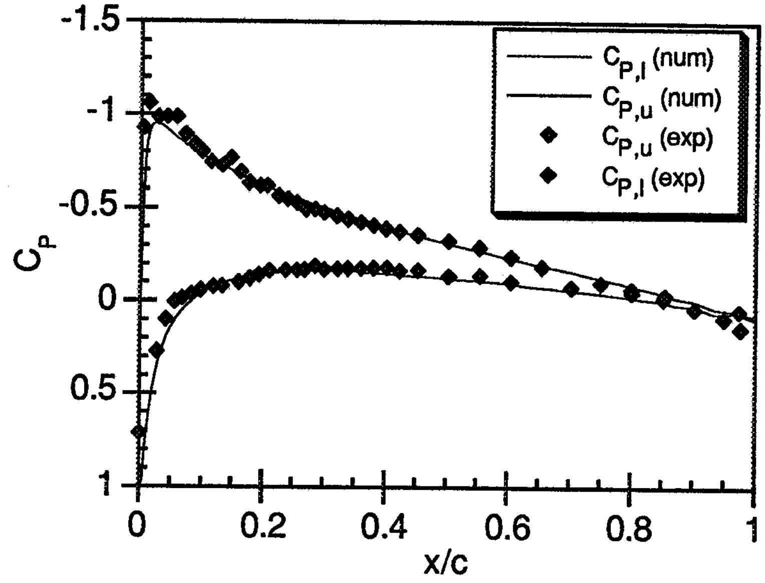

(c) 50% Span

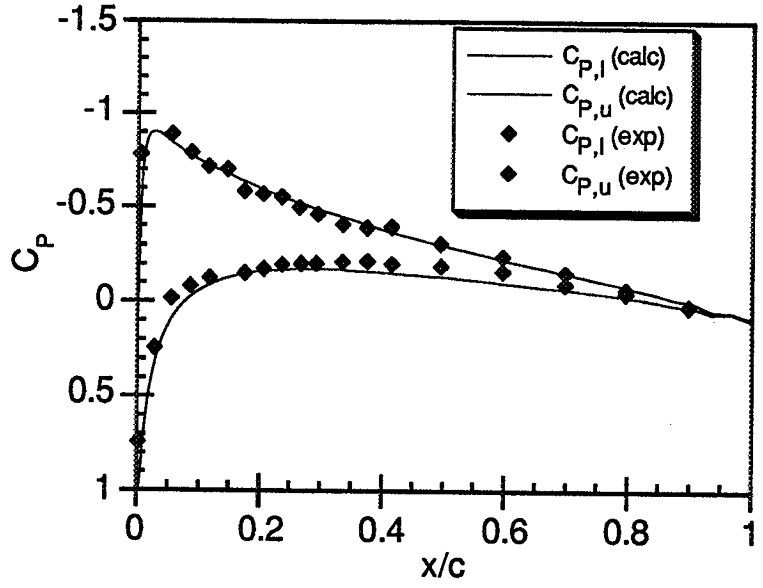

(d) 66% Span

Fig. 5.2: Surface Pressure Distributions for the Rectangular Wing at α=4° (continued)

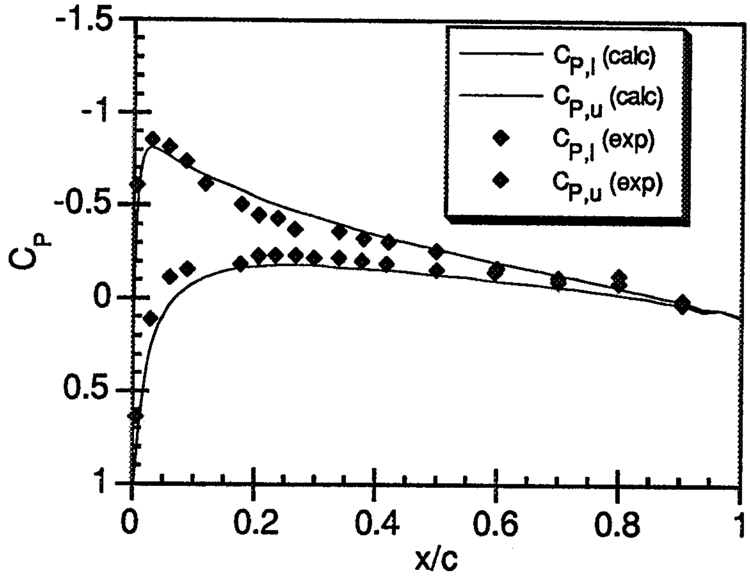

(e) 85% Span

Fig. 5.2: Surface Pressure Distributions for the Rectangular Wing at α=4° (concluded)

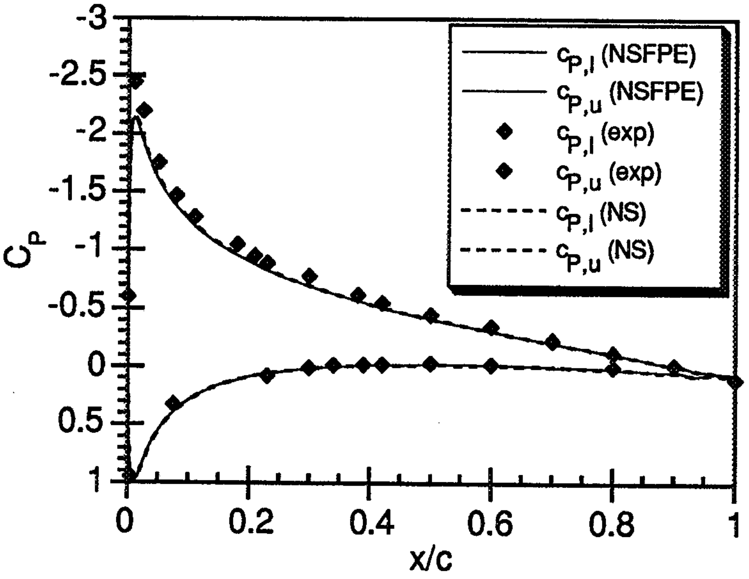

(a) 17% Span

Fig. 5.3: Surface Pressure Distributions for the Rectangular Wing at α=8°

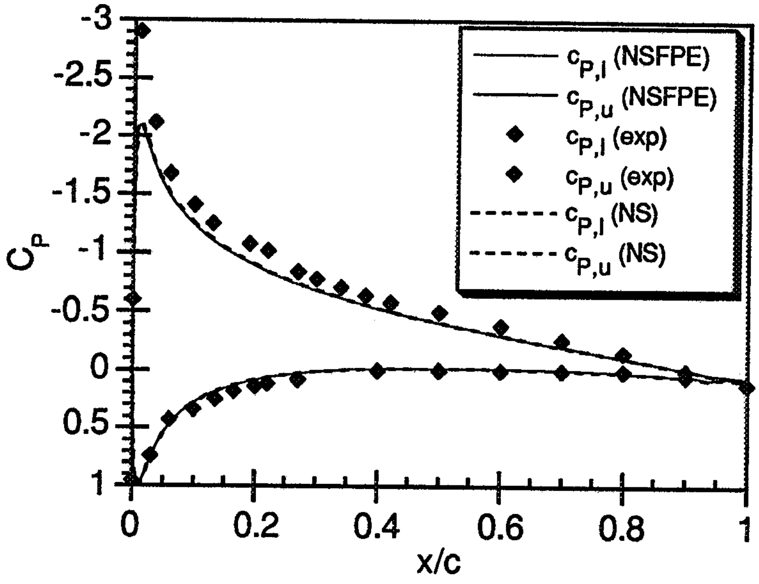

(b) 34% Span

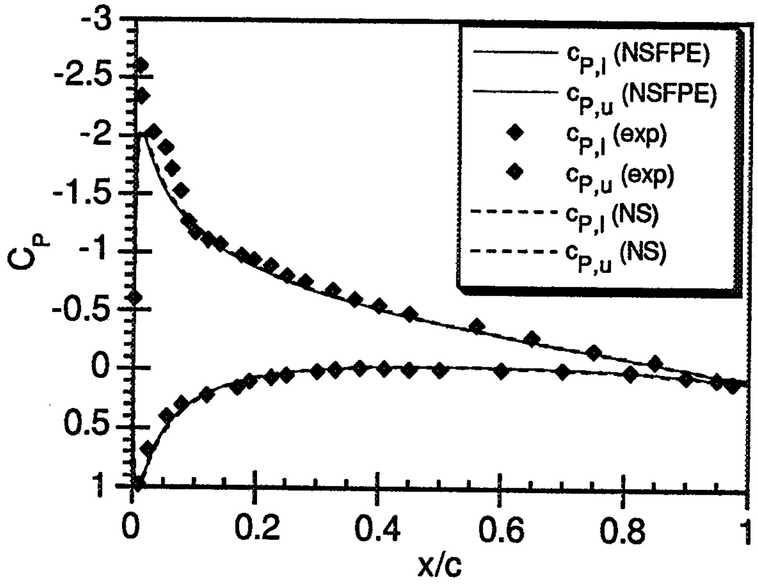

(c) 50% Span

Fig. 5.3: Surface Pressure Distributions for the Rectangular Wing at $\alpha=8°$ (continued)

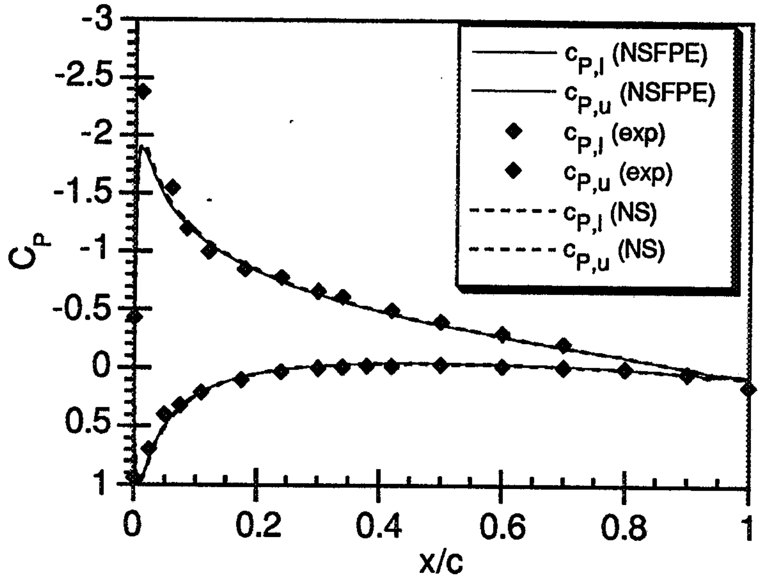

(d) 66% Span

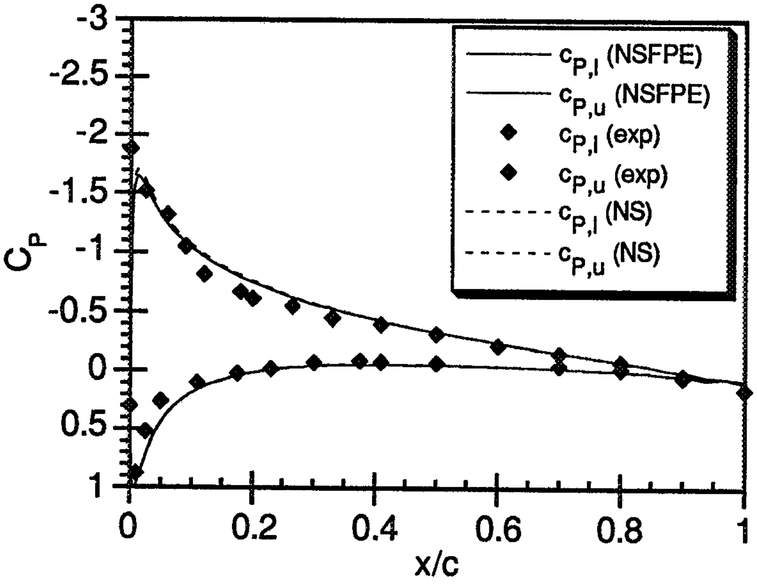

(e) 85% Span

Fig. 5.3: Surface Pressure Distributions for the Rectangular Wing at α=8° (concluded)

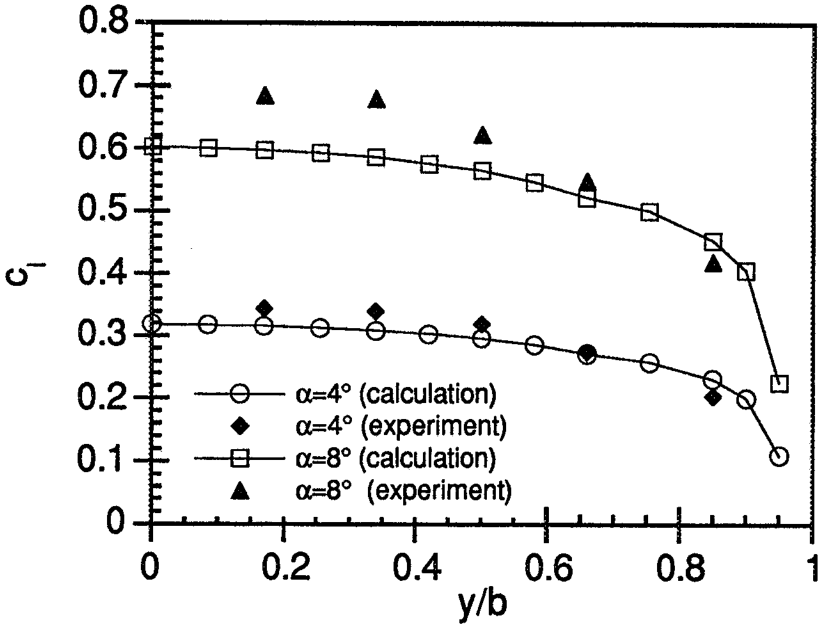

Fig. 5.4: Lift Distribution for the Rectangular Wing at α=4 and 8°

5.1.3. Convergence Histories

The convergence histories for the original hybrid scheme showed a highly oscillatory behavior, as shown in Fig. 5.5 for the rectangular wing at α=8°. These oscillations indicated false reflections from the Navier-Stokes/Full-Potential interface, which affected the solution at early time levels, and required a large number of iterations, about 4000 to 6000, while the Navier-Stokes code was able to achieve satisfactory convergence in about 2000 iterations.

A significant improvement was obtained by using the characteristic-based interface boundary conditions described in Chapter IV. The convergence history of the maximum residual in the Navier-Stokes zone for the rectangular wing at α=4° is shown in Fig. 5.6. The convergence history of the full Navier-Stokes computation is also shown for comparison. It can be observed that the hybrid method attains convergence characteristics similar to the full Navier-Stokes method when proper interface boundary conditions are used. Consequently the hybrid method was able to fully realize the computational savings of about 40% when the improved boundary conditions were used.

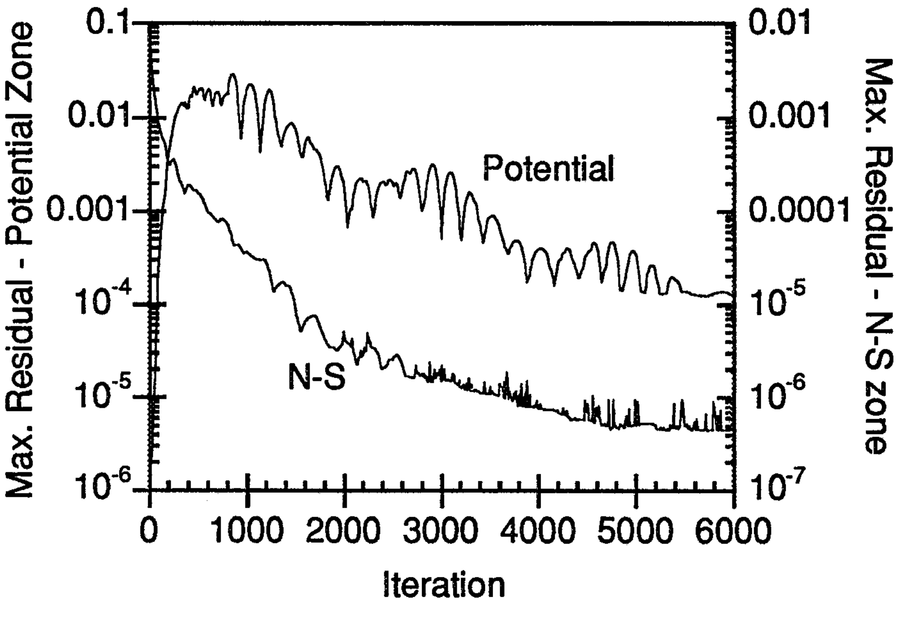

Fig. 5.5: Residual Histories in Potential and Navier-Stokes Zones (Rectangular Wing at α=8°).

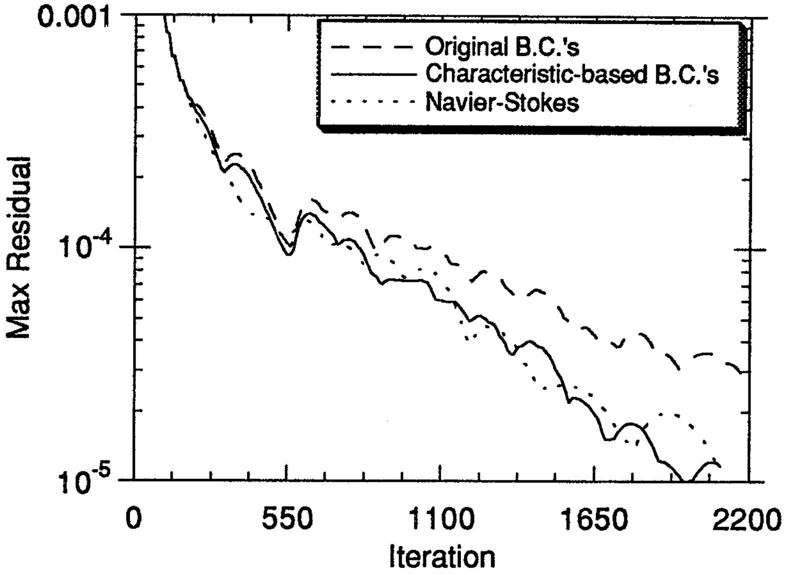

Fig. 5.6: Residual History in Navier-Stokes Zone with Original and Improved Interface Boundary Conditions (Rectangular Wing at α=4°).

5.2. F-5 Wing Studies

In order to investigate the applicability of the hybrid Navier-Stokes/Full-Potential method to unsteady compressible viscous flows, an unsteady problem involving the F-5 wing in pitch oscillations was studied, so that the effect of the interface boundary conditions on the accuracy of the time-dependent results could be verified. The investigation presented here is aimed at the transonic range, which is a very rigorous test for the present method, due to the development of shock waves which cross the Navier-Stokes/Full-Potential interface. The interface boundary conditions are therefore required to propagate significant disturbances. In the unsteady flow simulations, these disturbances have to be propagated in a time-accurate fashion, which presents an even more rigorous test. However, unsteady transonic flow simulations present also a potential for significant computational savings by using the present method, because of the numerous computations that are needed in a typical parametric investigation.

5.1.1. Configuration

The F-5 wing is chosen because a wealth of steady and unsteady data, as well as detailed geometric description, are readily available. It also represents a challenging configuration, since features such as taper and a thin, drooped leading edge are present. The experimental lay-out used by Tijdeman et al.[43,44] is illustrated in Fig. 5.7. The investigators measured steady and time-dependent pressures at eight spanwise stations indicated in Fig. 5.7 and listed in Table 5.1. Note that, for all cases presented here, no experimental data are used for the first point in the upper surface of the wing at spanwise stations 3 and 5, because the measuring probes at these points were defective.

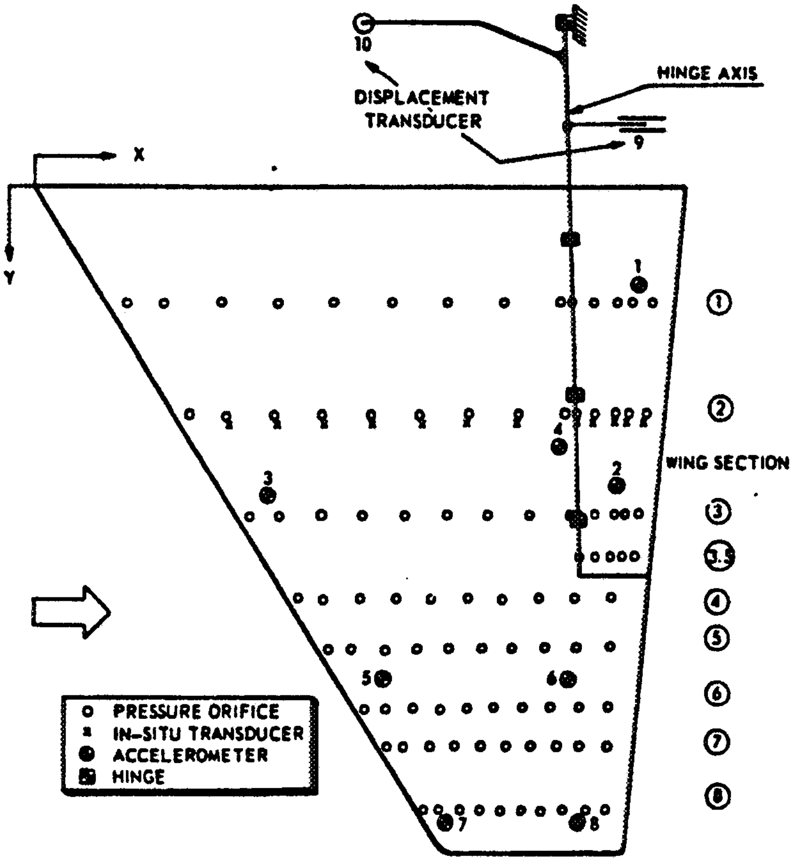
10
DISPLACEMENT TRANSDUCER
HINGE AXIS
9
X
Y
1
①
②
4
2
WING SECTION
3
③
③.⑤
④
⑤
5
6
⑥
⑦
⑧
7
8
o PRESSURE ORIFICE
▪ IN-SITU TRANSDUCER
● ACCELEROMETER
▨ HINGE

Fig. 5.7: F-5 Wing Experimental Lay-Out

Table 5.1: Spanwise Stations Where Experimental Data is Available for the F-5 Wing

Station No.	y/b (%)
1	18.1
2	35.2
3	51.2
4	64.1
5	72.1
6	81.7
7	87.5
8	97.7

The computational grid used in the present study, illustrated in Fig. 5.8, was an algebraic C-grid with 141 × 19 × 41 grid points, with 121 points over the wing surface at each spanwise station. 14 spanwise stations were used along the wing, with 5 stations extending beyond the tip. The Navier-Stokes and Full-Potential solvers were interfaced at KMATCH=20, so that about half of the number of points are located in each zone. The computations presented here were performed in NASA Lewis Research Center Cray-Y/MP. The CPU time for this configuration was about 0.95 sec per time step, about 73% of the CPU time needed for a full Navier-Stokes computation.

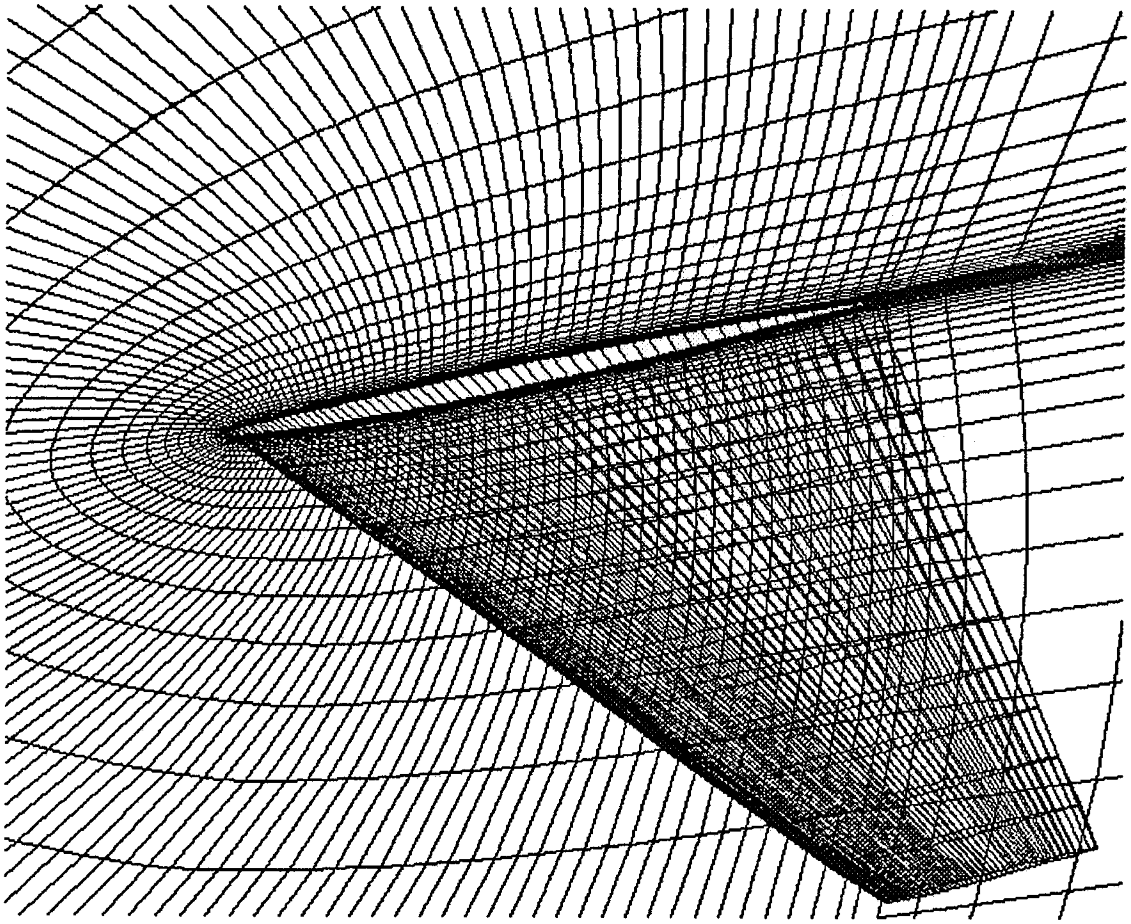

Fig. 5.8: Computational Grid for the F-5 Wing

5.2.2. Steady Flow Simulations

For steady flow simulations, the Mach numbers used in the present study were 0.6, 0.8, 0.9 and 0.95. The Reynolds number based on the root chord and free-stream speed $Re_1 = \rho_\infty U_\infty c_r/\mu_\infty$ was 11 million for M_∞=0.8. The angle of attack for all computations presented here was 0°.

The initial test case was M_∞=0.6. The steady pressure coefficient distributions at spanwise stations 35.2%, 72.1% and 97.7% are shown in Figs. 5.9(a), (b), and (c), respectively. The numerical results are in very good agreement with the experimental data. In particular the leading edge suction peaks seem well predicted, although insufficient experimental data are available in that region. Also the precise location where the lower and upper surface pressure coefficients match seems well predicted.

The next test case was M_∞=0.8. The steady pressure coefficient distributions at spanwise stations 35.2%, 72.1% and 97.7% are shown in Figs. 5.10(a), (b), and (c), respectively. Again the main features of the pressure distributions are well predicted.

A more demanding test case was M_∞=0.9, for which the steady pressure coefficient distributions at spanwise stations 35.2%, 51.2%, 64.1%, 72.1%, 87.5% and 97.7% are shown in Figs. 5.11(a) through (f), respectively. Again the suction peaks and the location where upper and lower surface pressure coefficient match seem well predicted. A slight underprediction of the suction values between 10% and 50% of the chord on the upper surface at the inboard stations is apparent. But the main feature of this configuration is the onset of a weak shock on the upper surface, near the tip. This shock may be observed in the experimental data in Fig. 5.11(f), but it appears that the weak shock was smeared in the numerical solution and cannot be clearly identified. By checking for supersonic points in the full-potential region, it was observed that the sonic line did cross the Navier-Stokes/Full-Potential interface for this configuration.

The last steady test case was M_∞=0.95, for which the steady pressure coefficient distributions at spanwise stations 35.2%, 51.2%, 64.1%, 72.1%, 87.5% and 97.7% are shown in Figs. 5.12(a) through (f), respectively. Here the dominating feature is the shock that forms over most of the wing, on both upper and lower surfaces. The upper surface shock is stronger and aft of the lower surface shock. These features were well predicted by the current method, although some slight underprediction of the mid-chord upper surface suction values is noticed. The suction peaks and location of matching upper and lower surface pressures are again well predicted, except at the station 97.7%, where the experimental data indicate a lower suction peak. This test case was demanding in the sense that the shock crosses the Navier-Stokes/Full-Potential interface, and the results presented here indicate that the hybrid method is able to predict adequately both shock location and strength even when the discontinuities due to the shock are propagated through the Navier/Stokes/Full-Potential interface. Further evidence to support this conclusion is presented in Fig. 5.13, where the density contours at station 81.7% of span, M_∞ = 0.95, are shown. In this figure, the Navier-Stokes/Full-Potential interface is drawn to facilitate the analysis. It can be seen that the contours smoothly cross the interface, and in particular the shock is well captured across the interface.

Overall the results presented here show that the hybrid method can be successfully applied to steady transonic flows, even when the shock crosses the Navier-Stokes/Full-Potential interface. The discrepancies observed near the tip seem to be due to inherent inaccuracies associated with the tapering of the computational grid outside the tip, and are present also in full Navier-Stokes computations, and consequently not associated with deficiencies in the hybrid method. Furthermore, the differences between the computed and measured data are of the same order of, or lower than, the more costly Navier-Stokes solutions presented by other researchers[30,88,154]. Numerical experimentation also indicated that for the transonic cases presented here, the current hybrid code with characteristic-based interface boundary conditions achieved higher convergence rates than the original hybrid code and even the full Navier-Stokes computations, probably due to the use of a higher time step in the FPE solver.Thus, it may be concluded that the present hybrid method gives results that are comparable to the more exact approaches, at less than 60% of the cost of Navier-Stokes simulations.

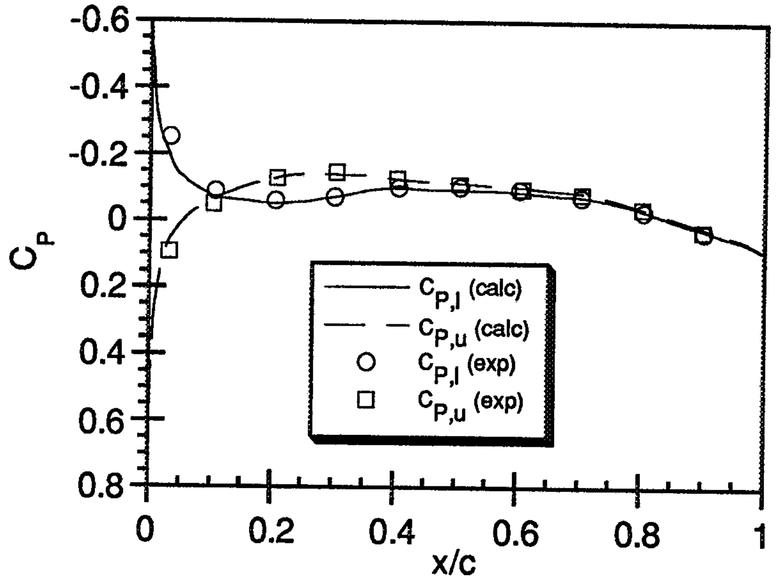

(a) 35.2% Span

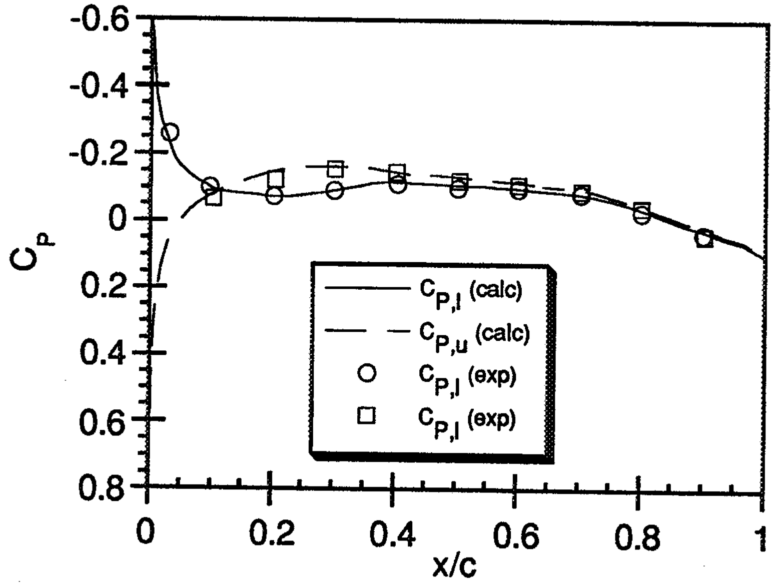

(b) 72.1% Span

Fig. 5.9: Steady Surface Pressure Distributions, $M_\infty = 0.6$

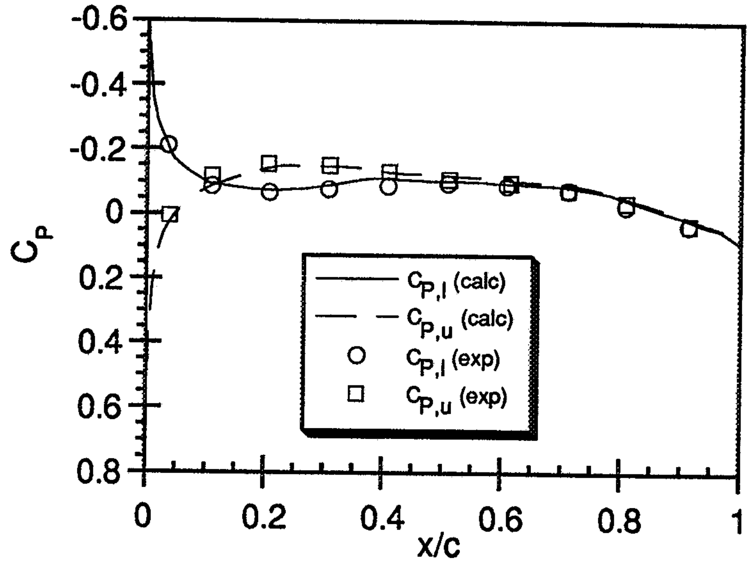

(c) 97.7% Span

Fig. 5.9: Steady Surface Pressure Distributions, $M_\infty = 0.6$ (concluded)

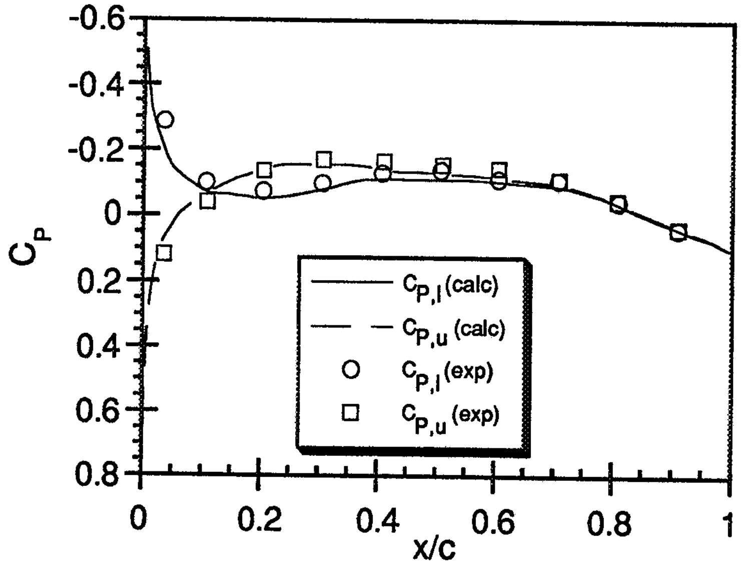

(a) 35.2% Span

Fig. 5.10: Steady Surface Pressure Distributions, $M_\infty = 0.8$

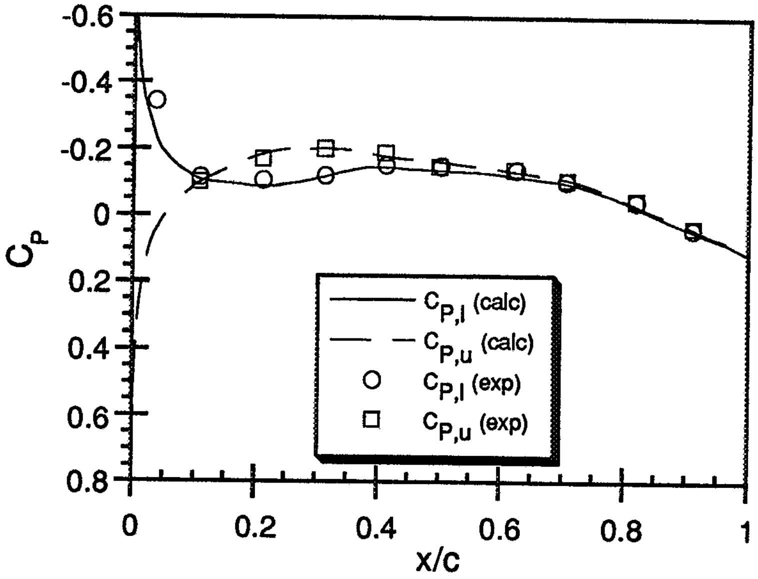

(b) 72.1% Span

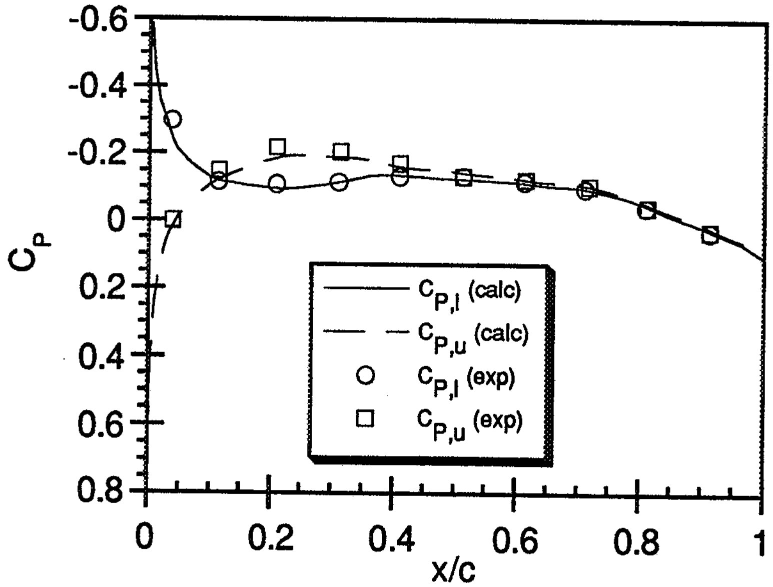

(c) 97.7% Span

Fig. 5.10: Steady Surface Pressure Distributions, $M_\infty = 0.8$ (concluded)

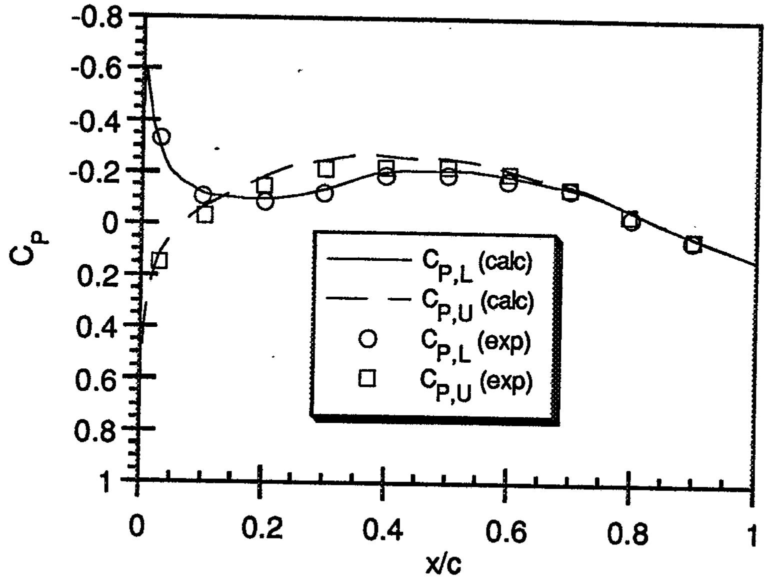

(a) 35.2% Span

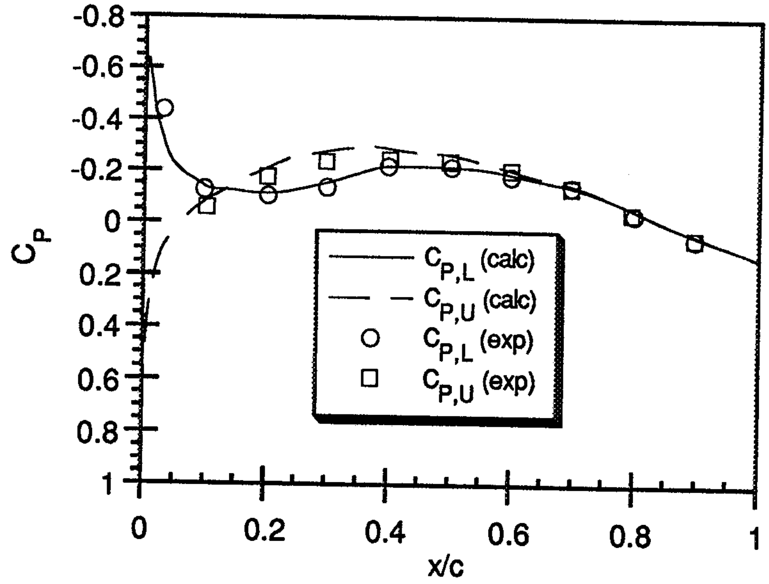

(b) 51.2% Span

Fig. 5.11: Steady Surface Pressure Distributions, $M_\infty = 0.9$

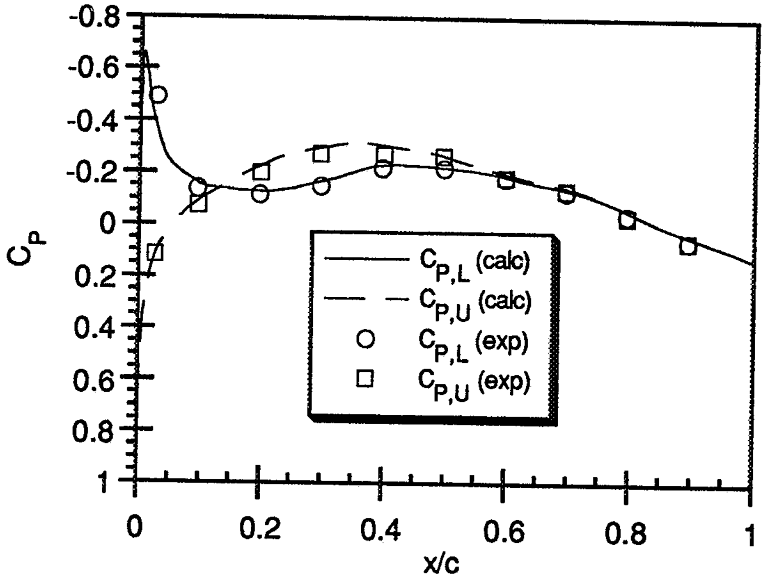

(c) 64.1% Span

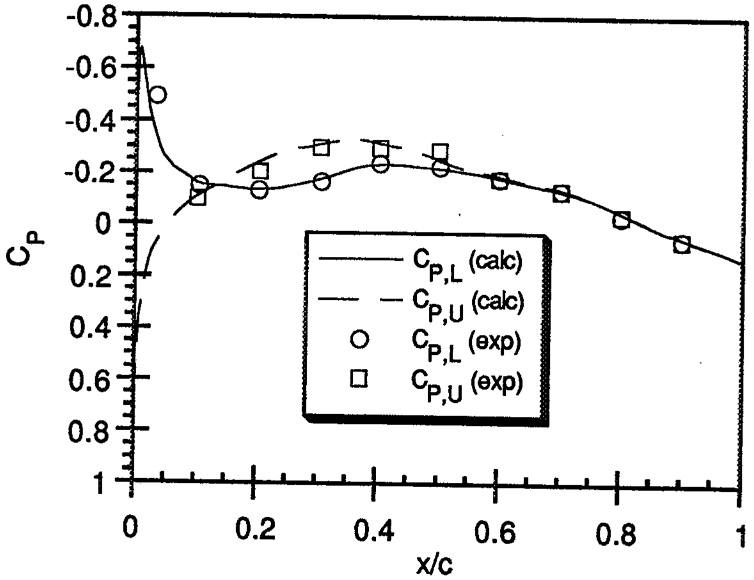

(d) 72.1% Span

Fig. 5.11: Steady Surface Pressure Distributions, $M_\infty = 0.9$ (continued)

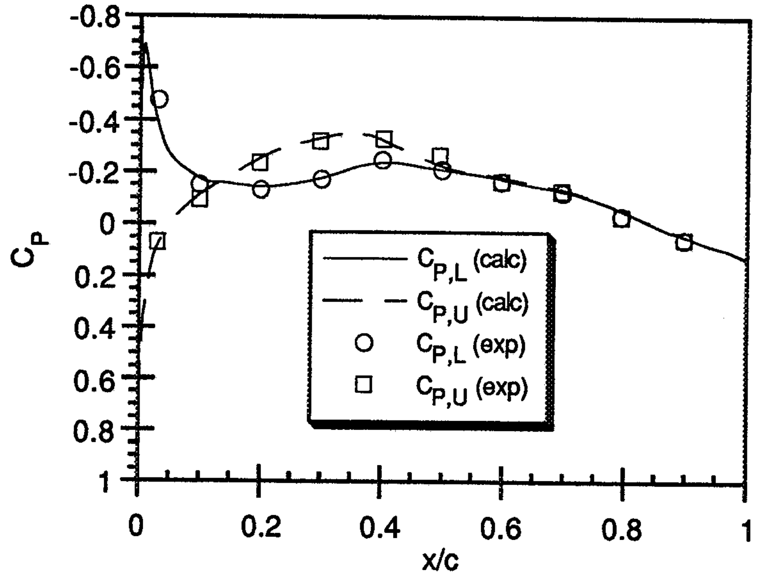

(e) 87.5% Span

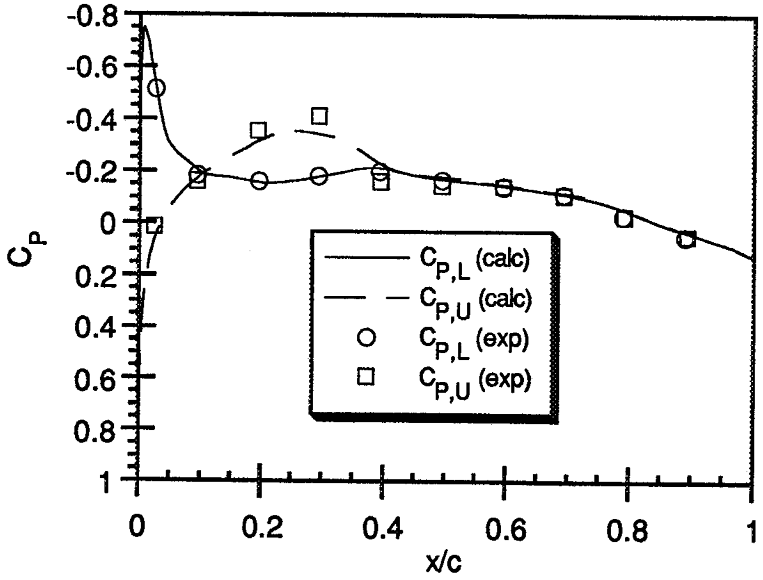

(f) 97.7% Span

Fig. 5.11: Steady Surface Pressure Distributions, $M_\infty = 0.9$ (concluded)

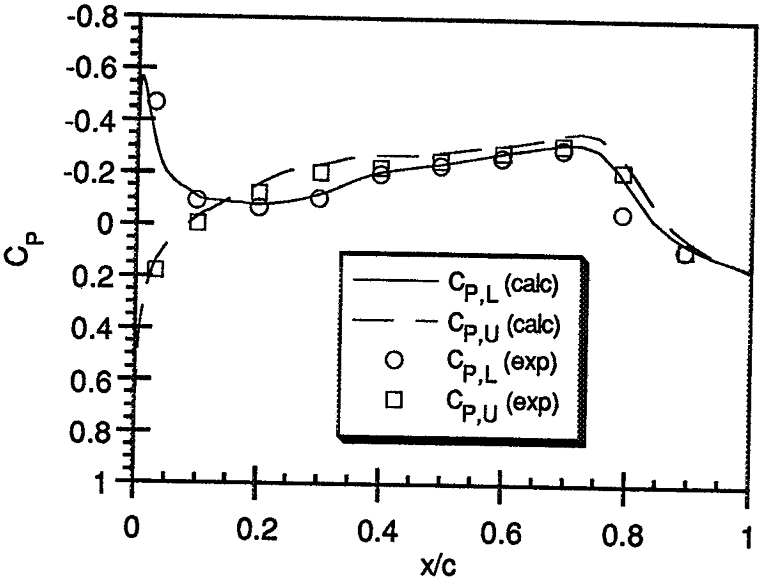

(a) 35.2% Span

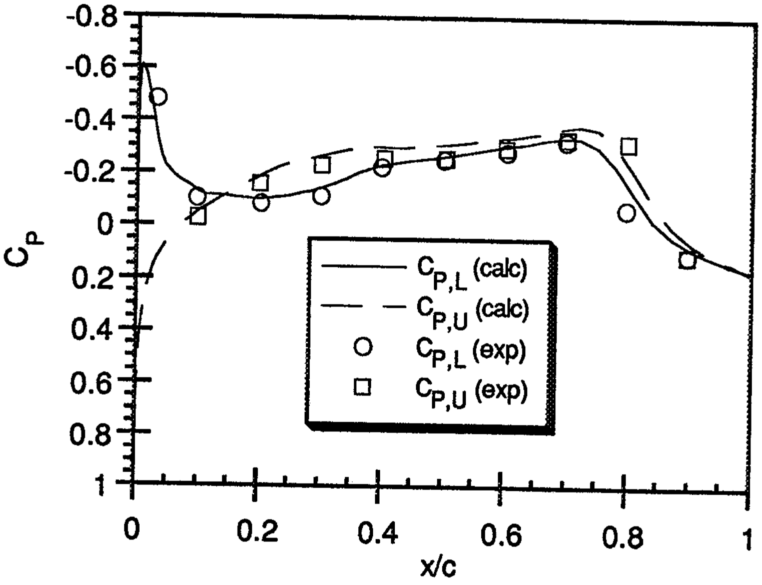

(b) 51.2% Span

Fig. 5.12: Steady Surface Pressure Distributions, $M_\infty = 0.95$

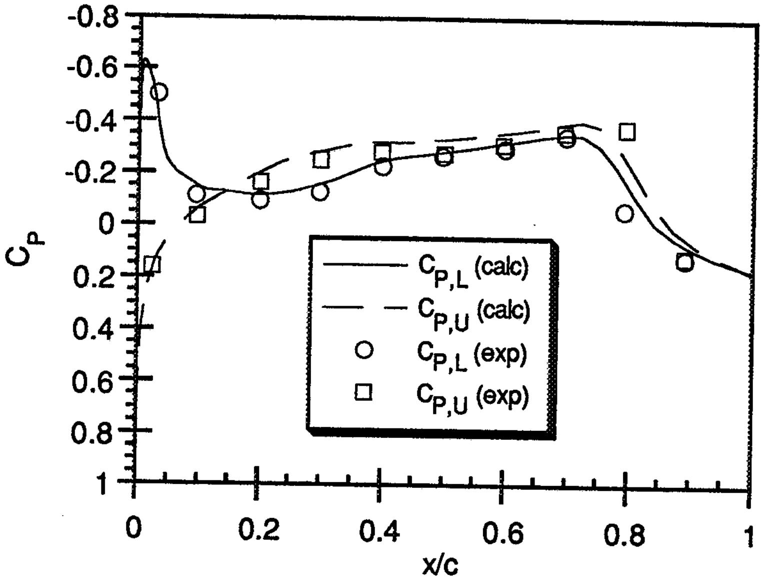

(c) 64.1% Span

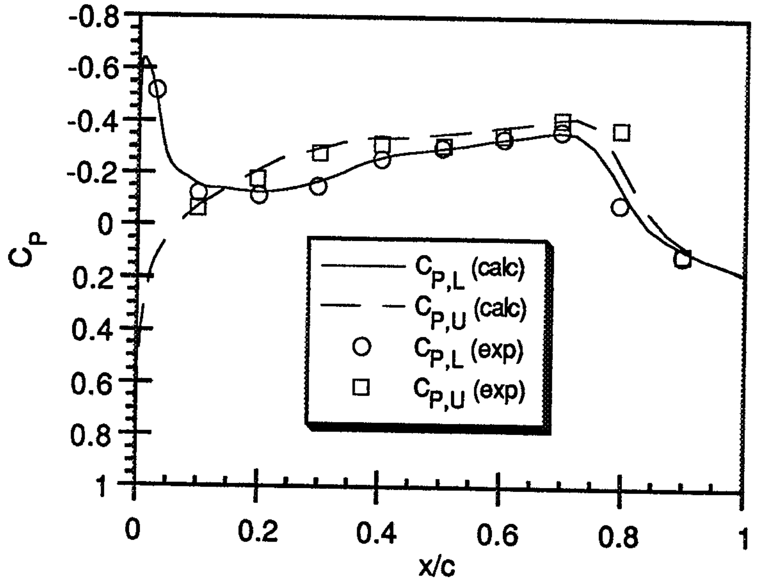

(d) 72.1% Span

Fig. 5.12: Steady Surface Pressure Distributions, $M_\infty = 0.95$ (continued)

C-2

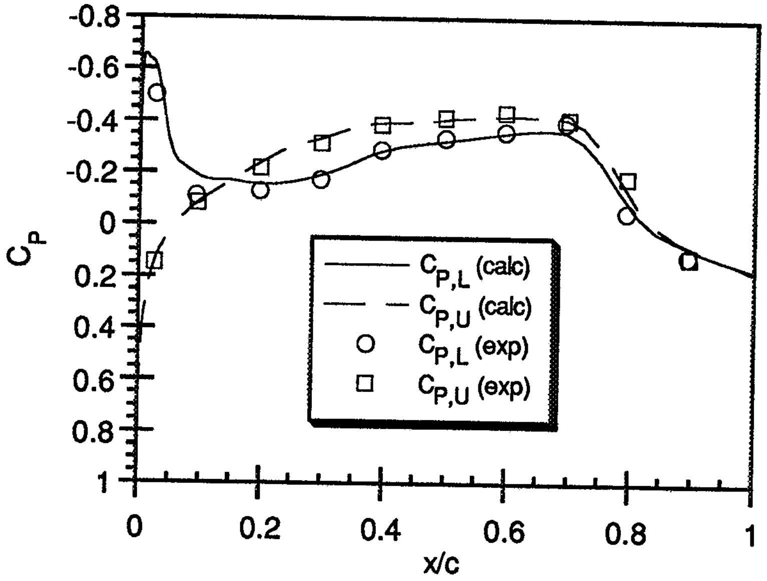

(e) 87.5% Span

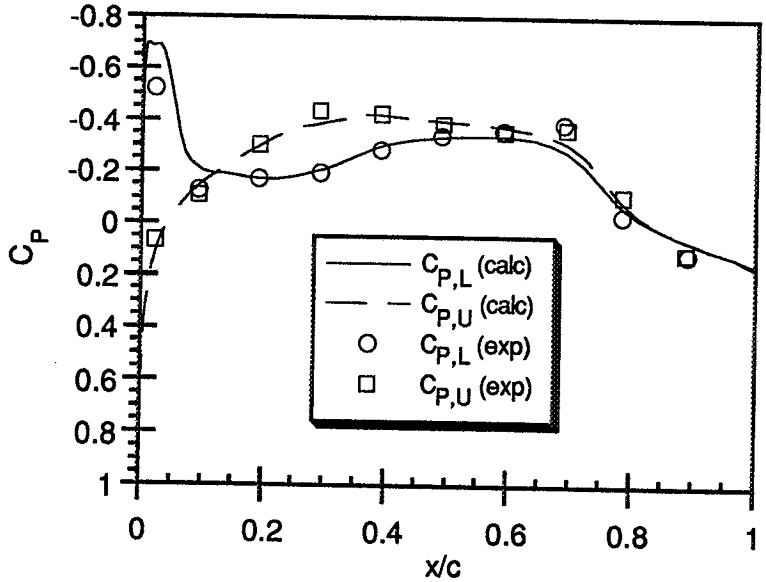

(f) 97.7% Span

Fig. 5.12: Steady Surface Pressure Distributions, $M_\infty = 0.95$ (concluded)

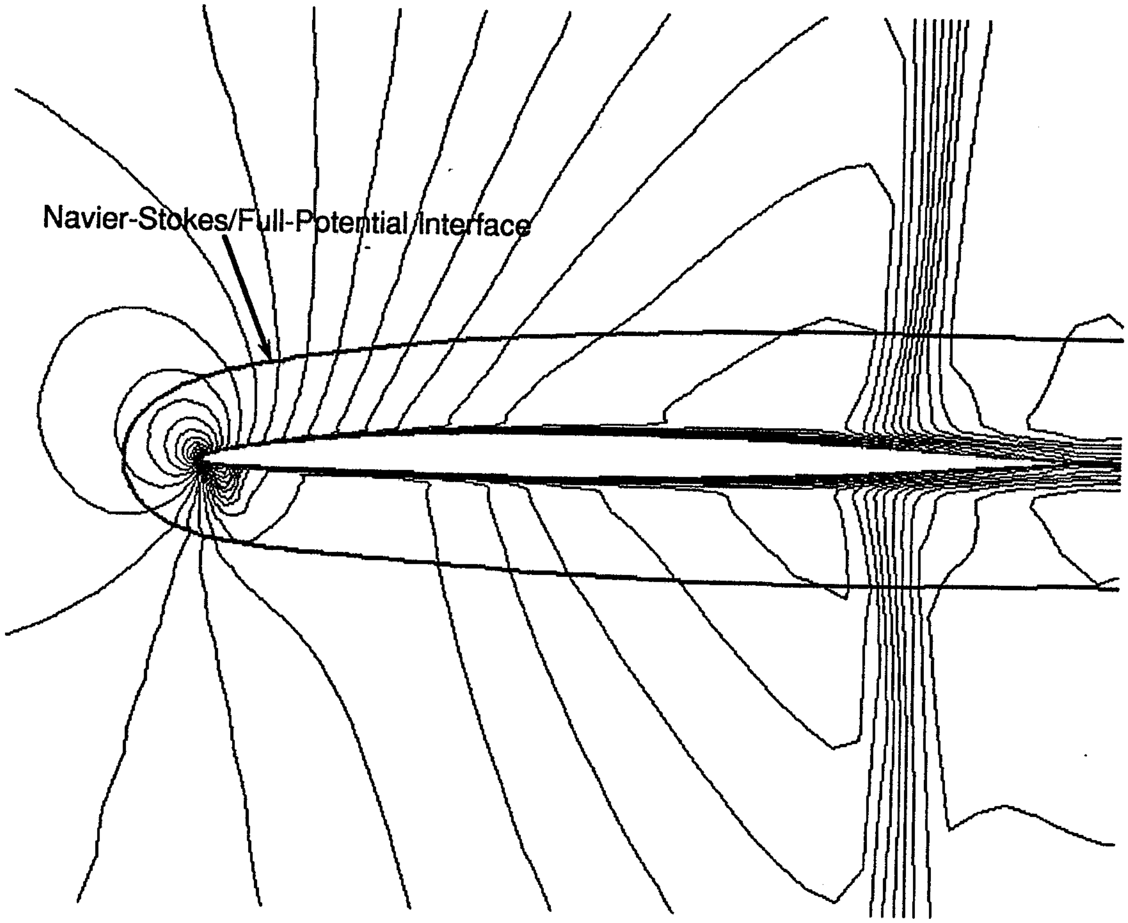

Fig. 5.13: Density Contours at 81.7% Span, $M_\infty = 0.95$

5.2.3. Unsteady Flow Simulations

Numerous unsteady flow simulations are typically needed to predict aeroelastic characteristics. These predictions are especially important in transonic flow, where aeroelastic instabilities are more likely to occur. In the transonic regime, the flow is inherently nonlinear, which has prevented the use of simpler methods, such as panel methods and vortex lattice methods. In particular, the presence of a supersonic region embedded in a subsonic region causes downstream disturbances to be propagated upstream with a considerable time lag, which results in significant out-of-phase forces. Full-potential and Euler methods have been applied to such flows with some success, but viscous effects can alter the location and strength of shocks. In an unsteady flow situation, both the location and strength of the shocks can change rapidly and generate significant unsteady forces, which have to be known for aeroelastic analysis. Navier-Stokes analyses are therefore a natural choice, but require drastically high computational resources. The present hybrid Navier-Stokes/Full-Potential method presents the advantage of fully capturing the viscous and nonlinear effects, while incurring a significantly lower computational cost. However, unsteady transonic flows are also very challenging to the present method, due to the presence of strong disturbances generated by unsteady shock motion, which need to be propagated through the Navier-Stokes/Full-Potential interface in a time-accurate fashion. The purpose of the investigation presented in this Section is to validate the present method for these flow conditions.

For the unsteady flow simulations presented here, the Mach numbers were 0.6, 0.9 and 0.95. The wing was in pitching oscillations about half-chord, and around $\alpha_0=0°$, i.e.:

$$\alpha(\tau)=\alpha_0+\Delta\alpha\ \sin(\kappa\tau) \tag{5.1}$$

where $\Delta\alpha$ is the amplitude of oscillation, given in Table 5.2 for the various test cases. Also, $\tau=a_\infty t/c$ is the nondimensional time, and $\kappa=\omega c/a_\infty$ is the reduced frequency, with c the reference length. Note that $\omega=2\pi F$, where F is expressed in Hertz. Note also that the definition of reduced frequency here differs from that of Tijdeman et al.[43], for consistency with the nondimensionalization used in the present work. The definition of reduced frequency here may be related to the definition in the cited reference as:

$$\kappa=\frac{\omega c}{a_\infty}=\frac{2\pi Fc}{a_\infty}=\underbrace{\frac{\pi F c_r}{U_\infty}}_{K_1}\underbrace{\frac{U_\infty}{a_\infty}}_{M_\infty}\frac{2c}{c_r}=K_1 M_\infty\frac{2c}{c_r} \tag{5.2}$$

where K_1 is the reduced frequency as defined by Tijdeman et al. and c_r is the root chord, equal to 0.6396 meters. The reference length used in the present study was 1 meter. The reduced frequencies corresponding to the test cases used here are listed in Table 5.2.

Table 5.2: Test Cases for Unsteady Flow

Test Case	M_∞	F (Hz)	$\Delta\alpha$ (deg)	K_1	κ
1	0.6	20	0.106	0.199	0.373
2	0.6	40	0.115	0.399	0.749
3	0.9	40	0.111	0.275	0.774
4	0.95	40	0.222	0.264	0.785

Under these pitching oscillations, the F-5 wing deforms aeroelastically. During the investigation reported by Tijdeman et al.[43,44], the wing vibration mode was measured for the various test runs using eight accelerometers. These measurements were used to obtain an approximate analytical expression for the vertical wing displacement at various points, assuming no chordwise deformation (rigid rotation) and parabolic spanwise deformation:

$$w(x,y) = a_{00} + a_{01}x + a_{10}y + a_{11}xy + a_{20}y^2 + + a_{21}xy^2 \tag{5.3}$$

where the coefficients a_{ij} are tabulated in Ref. 44. This approximation to the elastic deformation allows a consistent representation by a rigid rotation about the node corresponding to each spanwise station. The nodal lines corresponding to the cases presented here are illustrated in Fig. 5.14, from Ref. 44.

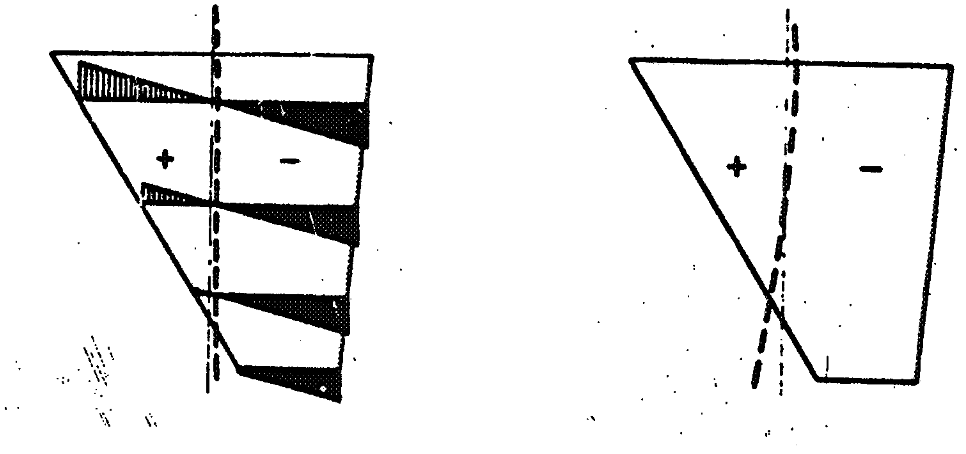

(a) M_∞=0.6, F=20Hz

(b) M_∞=0.6, F=40Hz

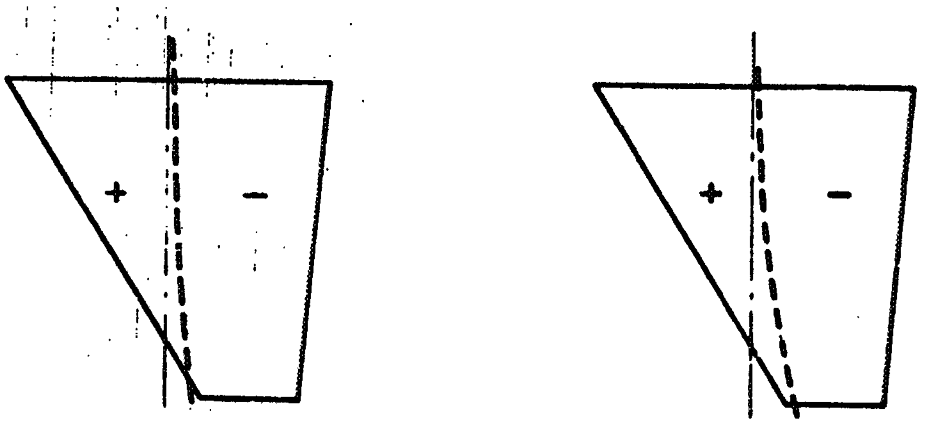

(c) M_∞=0.9, F=40Hz

(d) M_∞=0.95, F=40Hz

Fig. 5.14: Nodal Lines for F-5 Pitching Oscillations

For a given spanwise station y_j, the node is located at x_{N_j} and the motion at that spanwise station is represented by a local rigid pitching rotation about this node, given by:

$$\alpha_j(\tau) = \theta_j \alpha(\tau) \tag{5.4}$$

where $\alpha(\tau)$ is given by (5.1) and θ_j represents the mode shape, obtained from (5.3).

For each unsteady flow simulation presented here, the job is restarted from a previously converged steady flow solution at the specified Mach number and average angle of attack, $\alpha_0=0°$ in all cases considered here. It should be noted that the response of the flow field to the oscillatory motion will involve a transient and a steady-state response. This is illustrated in Fig. 5.15, where the time history of the lift coefficient at the spanwise station 64.1% for the case $M_\infty=0.95$, F=40 Hz, is shown. The results that will be presented subsequently involve only the steady-state response. For that purpose, enough iterations — typically about one cycle — were ran before the computation of the unsteady pressure coefficients was started. For the case $M_\infty=0.9$, F=40 Hz, an additional cycle was ran and the unsteady pressure coefficients were recomputed, yielding almost the same results with no perceptible differences from the previous cycle. This indicated that one cycle was indeed enough to eliminate the transient. Another concern was to verify that the response was dominated by the first harmonic. For that purpose, the second harmonic was also computed and it was observed that its values were negligible, except at locations where the first harmonics presented peaks, but at these locations the second harmonics were still much smaller than the first harmonics.

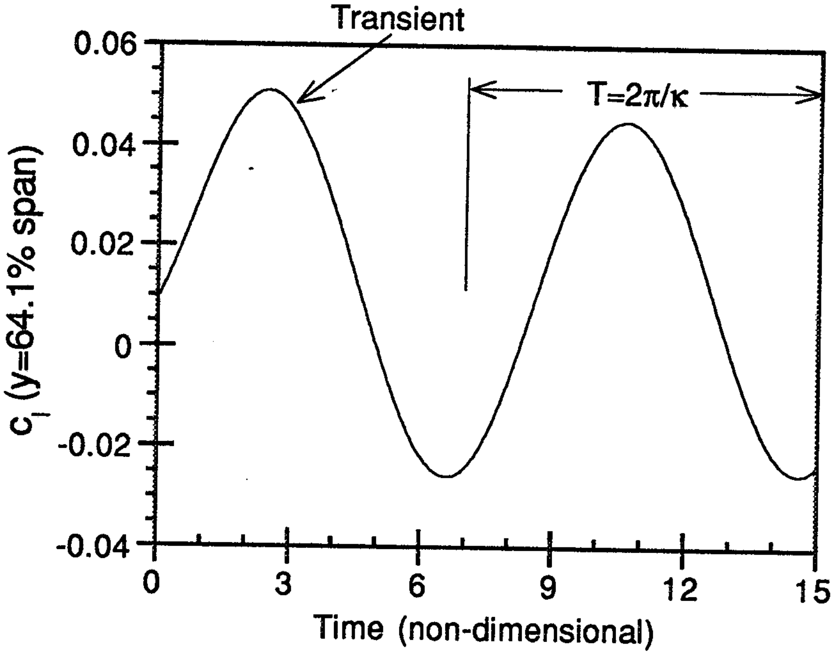

Fig. 5.15: Time History of the Lift Coefficient at 64.1% Span, M_∞=0.95, F=40 Hz.

The unsteady pressure coefficients were computed as follows: The actual oscillations of the wing are given by (5.2) with α_0=0°. Let the complex representation of the motion be:

$$\alpha^c(\tau) = \Delta\alpha \; e^{i\kappa\tau} \tag{5.5}$$

Now let the complex representation of the steady-state response be:

$$C_P^c(\tau) = \left[\mathrm{Re}(C_{P_i}) + i\,\mathrm{Im}(C_{P_i})\right] \; e^{i\kappa\tau} \tag{5.6}$$

Since the actual motion is given by the imaginary part of (5.5), the actual response is given by the imaginary part of (5.6) and can be related to the complex representation by:

$$\begin{aligned} C_P^c(\tau) &= \left[\mathrm{Re}(C_{P_i}) + i\,\mathrm{Im}(C_{P_i})\right]\, e^{i\kappa\tau} \\ &= \left[\mathrm{Re}(C_{P_i})\cos(\kappa\tau) - \mathrm{Im}(C_{P_i})\sin(\kappa\tau)\right] + i\underbrace{\left[\mathrm{Re}(C_{P_i})\sin(\kappa\tau) + \mathrm{Im}(C_{P_i})\cos(\kappa\tau)\right]}_{C_P(\tau)} \end{aligned} \tag{5.7}$$

Then $\mathrm{Re}(C_{P_i})$ and $\mathrm{Im}(C_{P_i})$ can be obtained in terms of the actual pressure coefficient response by:

$$\begin{aligned} \mathrm{Re}(C_{P_i}) &= \frac{\kappa}{\pi}\int_{\tau_1}^{\tau_1+2\pi/\kappa} C_P(\tau)\sin(\kappa\tau)d\tau \\ \mathrm{Im}(C_{P_i}) &= \frac{\kappa}{\pi}\int_{\tau_1}^{\tau_1+2\pi/\kappa} C_P(\tau)\cos(\kappa\tau)d\tau \end{aligned} \tag{5.8}$$

where τ_1 is chosen so that the transient is not included in the computations. It should be noted that the experimental unsteady pressure coefficients[43,44] were normalized with respect to the amplitude of oscillations, $2\Delta\alpha$. The actual computation of $\mathrm{Re}(C_{P_i})$ and $\mathrm{Im}(C_{P_i})$ is finally performed by the discretization of Eq. (5.8):

$$\begin{aligned} \mathrm{Re}(C_{P_i}) &= \frac{\kappa\Delta\tau}{2\pi\Delta\alpha}\sum_{m=m_1}^{m_1+m_T} C_{P_m}\sin(\kappa m\Delta\tau) \\ \mathrm{Im}(C_{P_i}) &= \frac{\kappa\Delta\tau}{2\pi\Delta\alpha}\sum_{m=m_1}^{m_1+m_T} C_{P_m}\cos(\kappa m\Delta\tau) \end{aligned} \tag{5.9}$$

where m denotes the time step number, $m_1 = \tau_1/\Delta\tau$, and $m_T = 2\pi/\kappa\Delta\tau$. Note that the normalization with respect to the amplitude of oscillations has been included in Eq. (5.9).

Using the above described procedure, the unsteady pressure coefficients were computed for the configurations listed in Table 5.2. The first test case corresponds to Mach number 0.6, frequency of 20 Hz and amplitude of oscillation 0.106 degrees. The nondimensional time step $\Delta\tau = a_\infty \Delta t/c$ was 0.005, so that 3369 time steps per cycle were needed. The unsteady pressure coefficient distributions at spanwise stations 35.2% and 72.1% are shown in Fig. 5.16. The in-phase (real) component is in good agreement with the experiment, although few test data are available near the leading edge to confirm the level of unsteady pressure peaks. In particular, at 72.1% span the first experimental point in the upper surface is missing and the first experimental point in the lower surface seems faulty, as a peak is expected near the leading edge. The out-of-phase (imaginary) component leading edge peaks appear well predicted, and so are the distributions from about 40% chord towards the trailing edge, although the location where the lower and upper surface imaginary components match is predicted aft of the experimental location.

The next test case corresponds to Mach number 0.6, frequency of 40 Hz and amplitude of oscillation 0.115 degrees. The nondimensional time step was 0.005, so that 1678 time steps per cycle were needed. The unsteady pressure coefficient distributions at spanwise stations 35.2% and 72.1% are shown in Fig. 5.17. Again the in-phase (real) component appears to be in good agreement with the experiment, showing little change with respect to the previous test case (F=20Hz). At this higher frequency, the out-of-phase (imaginary) component is overall higher than for the lower frequency, in both the experimental and computed results. This imaginary component appears well predicted for the locations aft of 30% chord, but the location where the lower and upper surface imaginary components cross is predicted aft of the experimental location. The leading edge peaks also seem overpredicted, although very few experimental points are available there.

The next test case was M_∞=0.9, frequency 40 Hz and amplitude of oscillation 0.111 degrees. The nondimensional time step was 0.005, so that 1624 time steps per cycle were needed. The real and imaginary parts of the unsteady pressure coefficient distributions at spanwise stations 35.2%, 51.2%, 64.1%, 72.1%, 87.5% and 97.7% are shown in Figs. 5.18(a) through (l). At all spanwise stations strong leading edge peaks are present in the lower surface both in the in-phase and out-of phase component and they seem to be well predicted by the present method. It may be recalled that in the steady case, discussed in Section 5.2.2 above, the main feature of this configuration was the onset of a weak shock on the upper surface, near the tip, which could be observed in the experimental data in Fig. 5.11(f). In the unsteady case, strong variations in the pressure coefficients are noticed about 50% of the chord at all spanwise stations. These indicate that the oscillatory motion causes a shock wave to form over most of the wing and move back and forth, generating the strong variations observed here.

On the lower surface, the real part of the unsteady pressure coefficient shows relatively small variations, as seen in Figs. 5.18(a), (c), (e), (g), (i) and (k), while the imaginary part shows stronger variations. This indicates that the shock wave on the lower surface is predominantly out of phase with respect to the motion. The present method predicts this phenomenon for inboard stations, up to about half span, as seen in Figs. 5.18(b) and (d), although about 15% of the chord aft of the experimental data and somewhat smeared. At outer stations, the unsteady shock on the lower surface appears to smeared and even disappears in the computed results.

On the upper surface, both the real and imaginary components show significant variations indicating a stronger shock moving, with a significant in-phase, but higher out-of-phase component. This phenomenon is better predicted in all spanwise stations, especially the chordwise location, around mid-chord. The imaginary part in Figs. 5.18(b), (d), (f) and (h) seems to indicate some underprediction of strength of the out-of-phase component of the shock, which may be due to smearing.

The results discussed above for the case $M_\infty=0.9$, F=40 Hz are quite similar to full Navier-Stokes computations performed with a different version of the Navier-Stokes module used here[30]. The same test case was also investigated by Obayashi et al.[154], who used a streamwise upwind algorithm. In that paper, only the upper surface results were presented and a comparison was made between the streamwise upwind algorithm and a central-difference algorithm, with a more favorable correlation for the former. Since the present method is modular, an upwind Navier-Stokes module could potentially improve the unsteady shock prediction while maintaining the computational savings obtained by the hybrid Navier-Stokes/Full-Potential method. It should be noted that this case was a rigorous test for the hybrid method, since the unsteady shock is moving back and forth and crossing the Navier-Stokes/Full-Potential interface. As the shock is not completely aligned with the grid, strong oblique disturbances are propagated through the interface. The results presented here show that the interface boundary conditions are adequate to transmit these disturbances in a time-accurate fashion.

The last test case was M_∞=0.95, frequency 40 Hz and amplitude of oscillation 0.222 degrees. The nondimensional time step was 0.005, so that 1601 time steps per cycle were needed. An additional computation to assess the effect of the time step was made with a nondimensional time step of 0.002, for which 4003 time steps per cycle were needed. The real and imaginary parts of the unsteady pressure coefficient distributions at spanwise stations 35.2%, 51.2%, 64.1%, 72.1%, 87.5% and 97.7% are shown in Figs. 5.19(a) through (l). As occurred in the previous test case, at all spanwise stations strong leading edge peaks are present in the lower surface both in the in-phase and out-of phase component and they seem to be well predicted by the present method. The steady flow results for M_∞=0.95, shown in Fig. 5.12, indicate a strong shock on both upper and lower surfaces around 80% of the chord. The experimental data for the unsteady case, seen in Fig. 5.19, show significant peaks around this chordwise location, mostly in the real (in-phase) component, but also in the imaginary (out-of-phase) component. These peaks are very localized, which indicates that they result more from shock strength variations than shock movement. The numerical results presented in Fig. 5.19 show that the present method was unable to correctly predict the peak in the real part, but predicted the peak in the imaginary part. The computations with a smaller time step show some improvement in the real part, which indicate that the time step might have to be further reduced to yield a better correlation. Further reductions in time step were not attempted because of the large CPU resources that would be needed. This improvement with time step also indicates that the deficiency is not due to the hybrid method. It should also be noted that the current coarse grid presents some smearing in the shock, therefore small changes in the shock strength are not likely to be well captured, even with a smaller time step.

Except for the above discussed discrepancy, the unsteady pressure coefficient distribution is well predicted. It should be noted that this is a very rigorous test for the present method, due to the strong shock crossing the Navier-Stokes interface, as seen in Fig. 5.13. The results presented here indicate that the discrepancies observed in this test case are inherent to the Navier-Stokes module, and can probably be overcome by using an upwind Navier-Stokes module capable of capturing sharper shocks.

Overall the unsteady pressure coefficient distributions correlate well with experimental data and are similar to those obtained with equivalent full Navier-Stokes computations, with a fraction of the computational cost. The savings in CPU time were found to depend on the vector capability of the CPU, ranging from 27% on the Cray Y/MP-L up to 40% on a HP Apollo 700 workstation. It is believed that effective clock times could be reduced even more with respect to full Navier-Stokes computations on distributed processing machines, since the entire Full-Potential module could be solved in parallel without data exchange with the Navier-Stokes solver, for a given iteration. This possibility, however, is yet to be investigated.

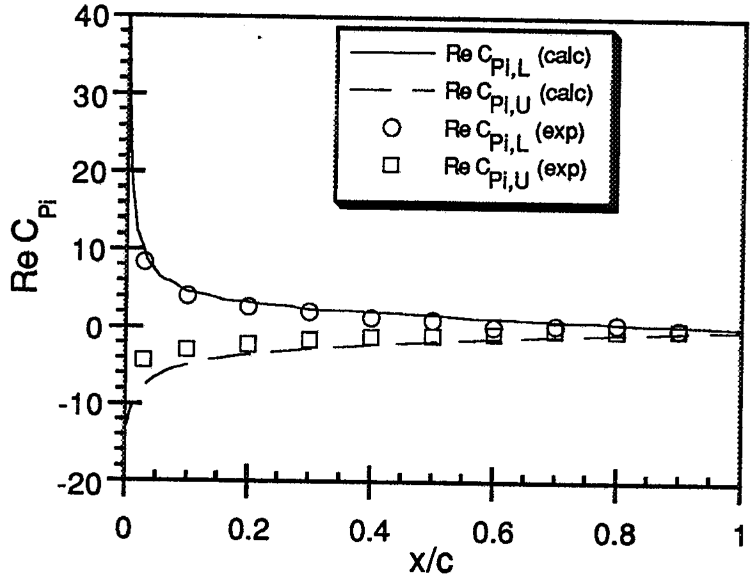

(a) Real Part, 35.2% Span

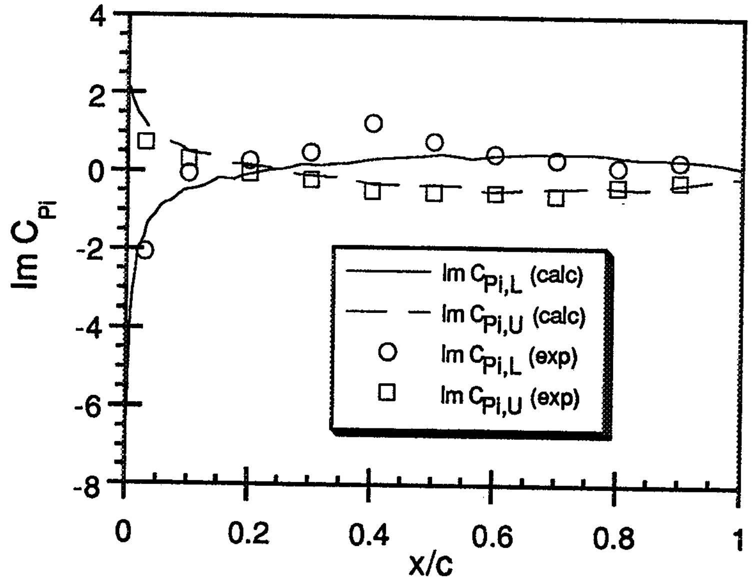

(b) Imaginary Part, 35.2% Span

Fig. 5.16: Unsteady Surface Pressure Distributions, $M_\infty = 0.6$, f=20 Hz

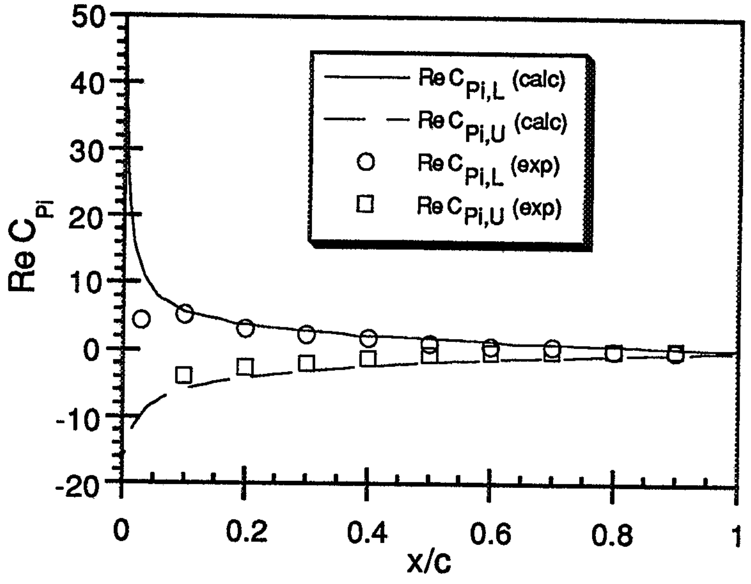

(c) Real Part, 72.1% Span

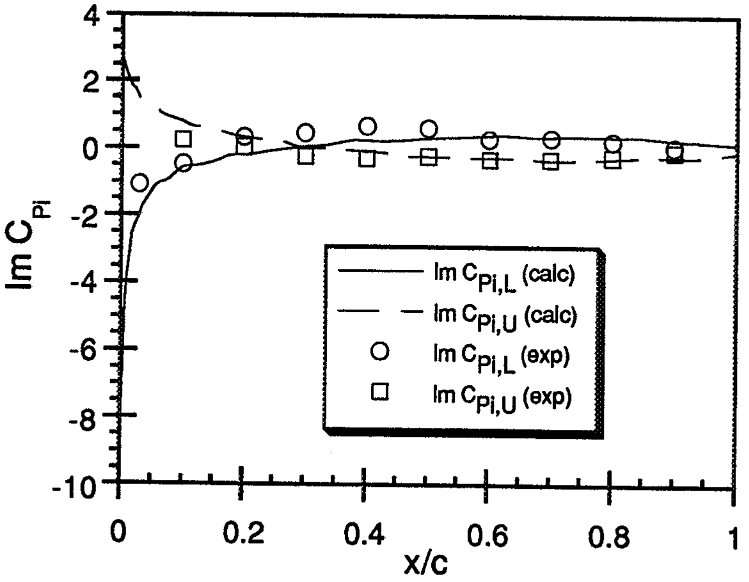

(d) Imaginary Part, 72.1% Span

Fig. 5.16: Unsteady Surface Pressure Distributions, $M_\infty = 0.6$, f=20 Hz (concluded)

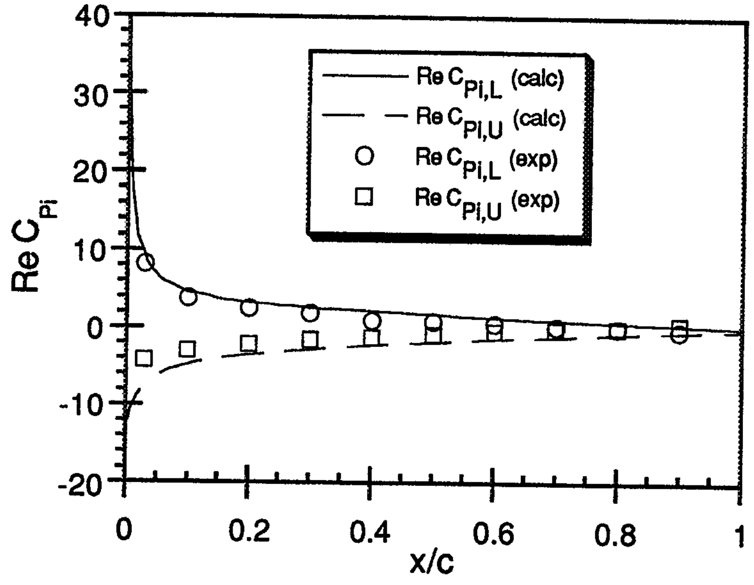

(a) Real Part, 35.2% Span

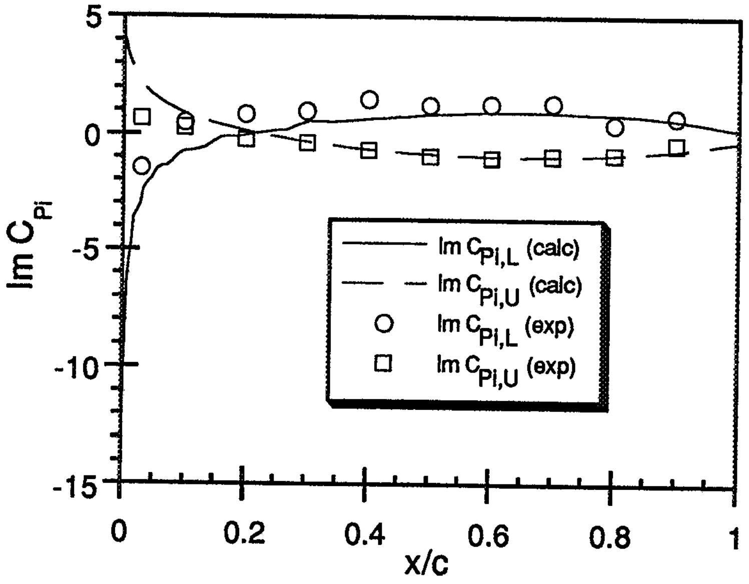

(b) Imaginary Part, 35.2% Span

Fig. 5.17: Unsteady Surface Pressure Distributions, $M_\infty = 0.6$, f=40 Hz

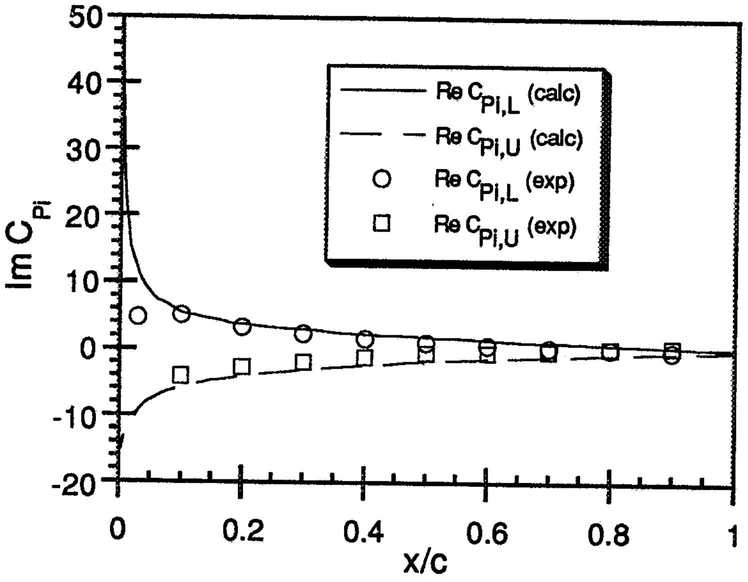

(c) Real Part, 72.1% Span

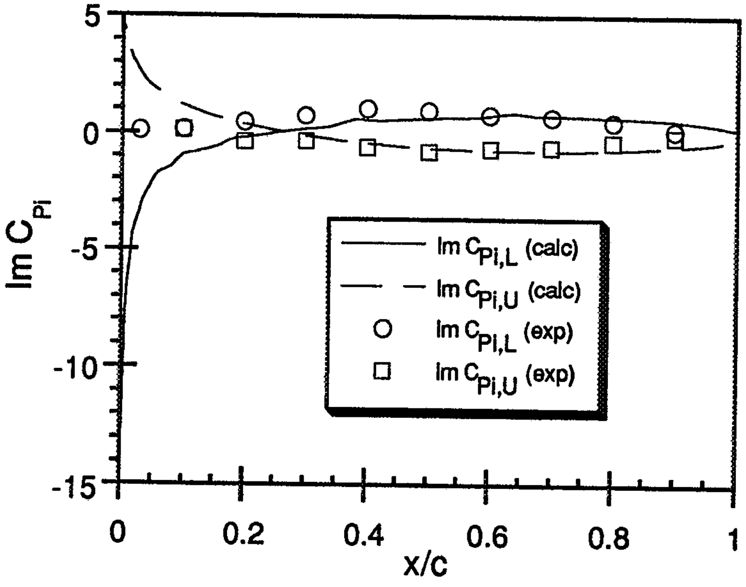

(d) Imaginary Part, 72.1% Span

Fig. 5.17: Unsteady Surface Pressure Distributions, $M_\infty = 0.6$, f=40 Hz (concluded)

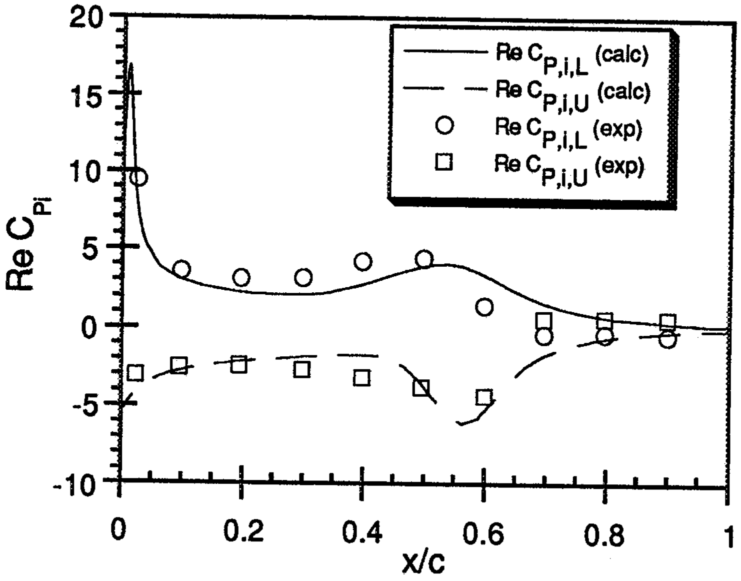

(a) Real Part, 35.2% Span

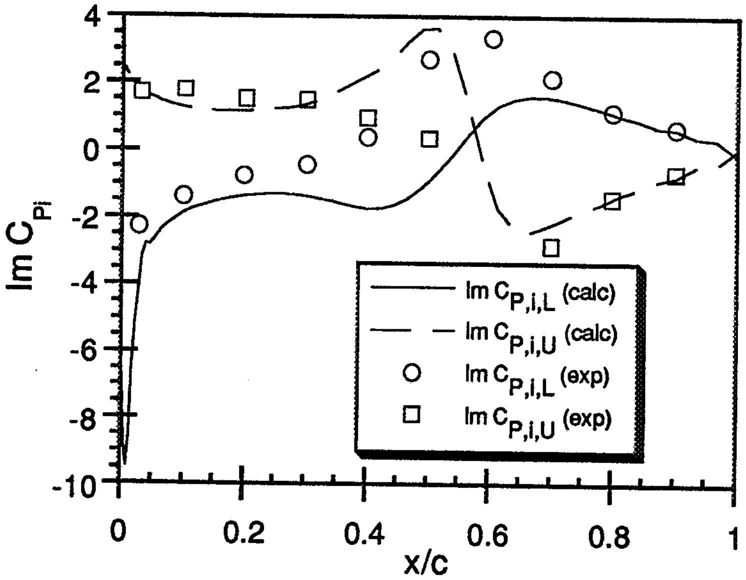

(b) Imaginary Part, 35.2% Span

Fig. 5.18: Unsteady Surface Pressure Distributions, $M_\infty = 0.9$, f=40 Hz

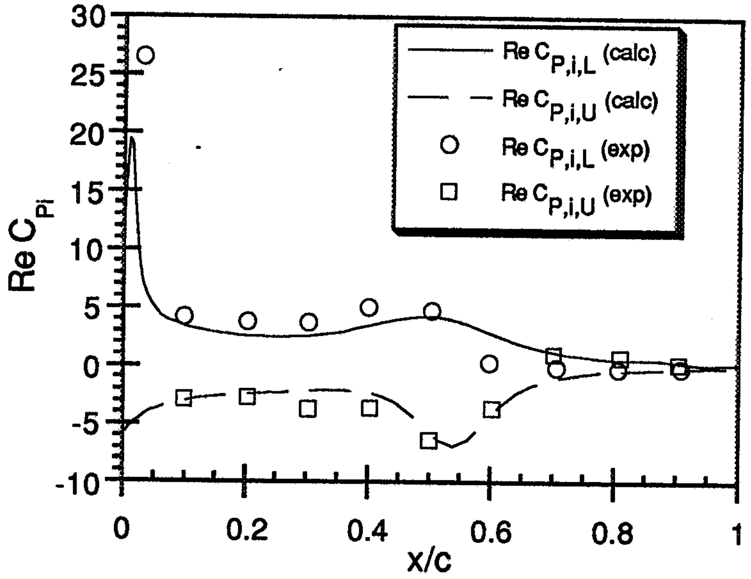

(c) Real Part, 51.2% Span

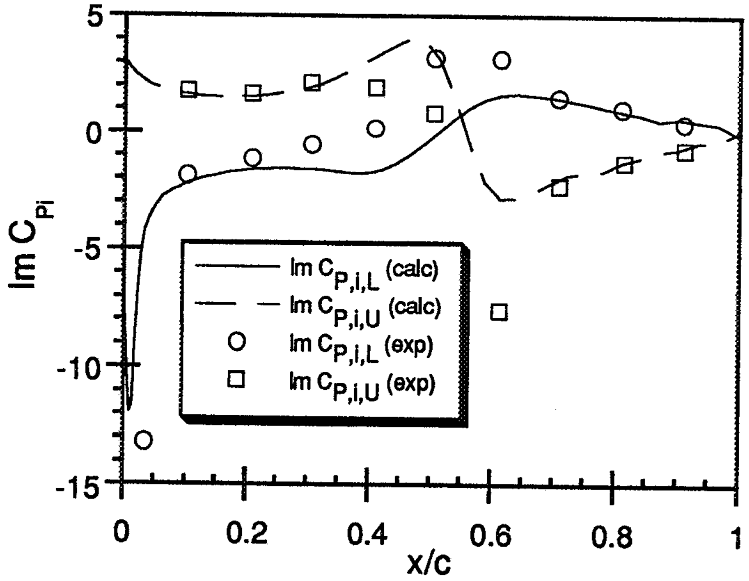

(d) Imaginary Part, 51.2% Span

Fig. 5.18: Unsteady Surface Pressure Distributions, $M_\infty = 0.9$, f=40 Hz (continued)

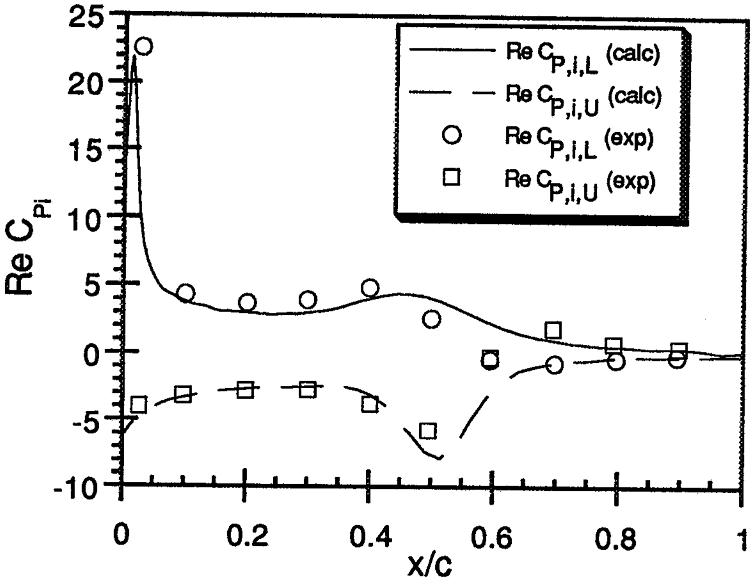

(e) Real Part, 64.1% Span

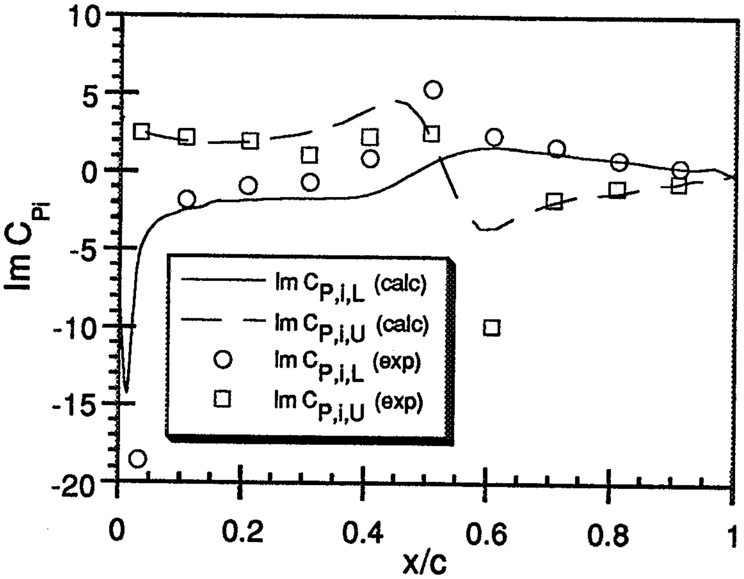

(f) Imaginary Part, 64.1% Span

Fig. 5.18: Unsteady Surface Pressure Distributions, $M_\infty = 0.9$, f=40 Hz (continued)

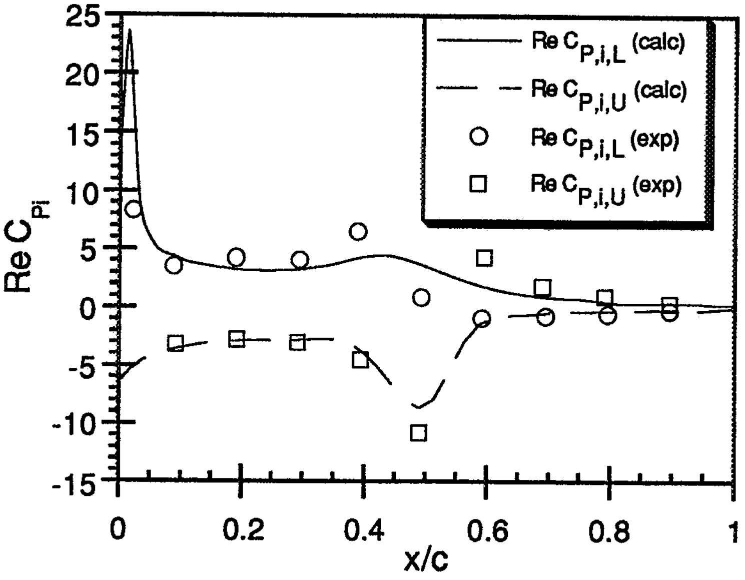

(g) Real Part, 72.1% Span

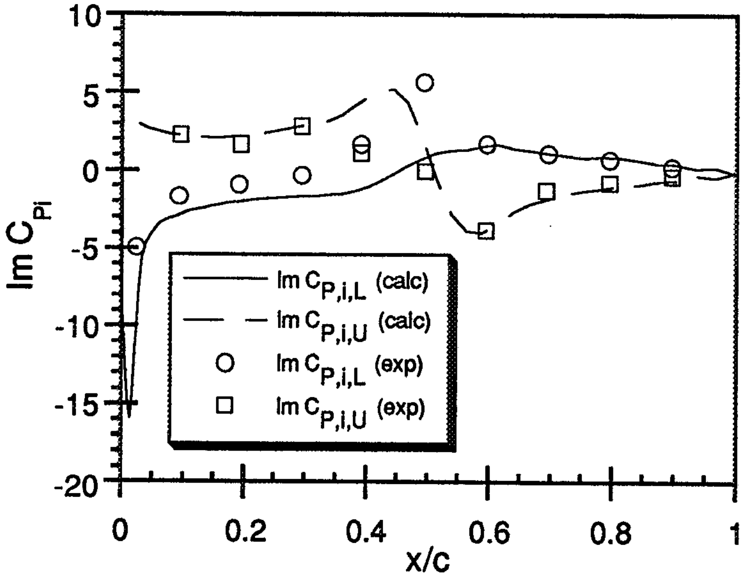

(h) Imaginary Part, 72.1% Span

Fig. 5.18: Unsteady Surface Pressure Distributions, $M_\infty = 0.9$, f=40 Hz (continued)

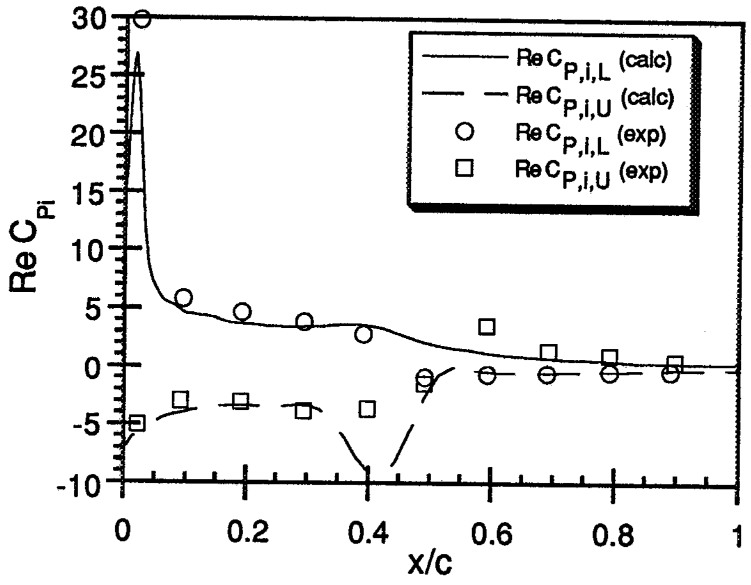

(i) Real Part, 87.5% Span

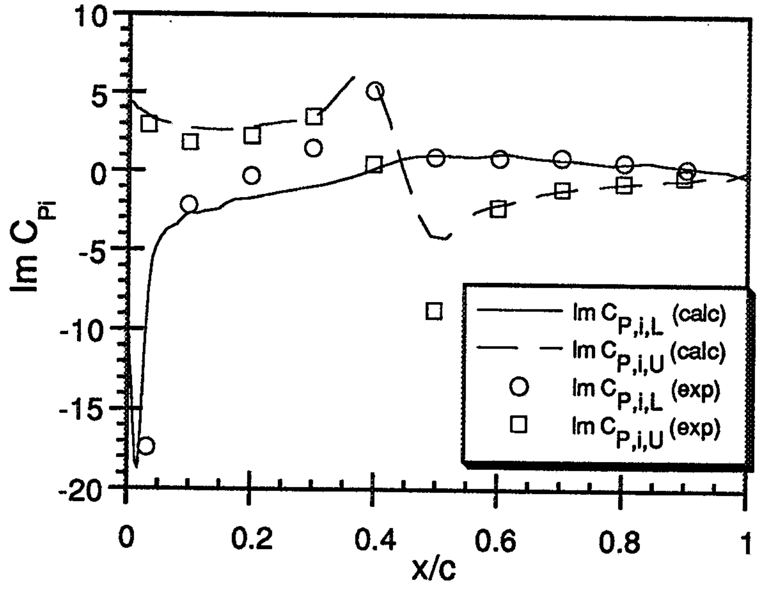

(j) Imaginary Part, 87.5% Span

Fig. 5.18: Unsteady Surface Pressure Distributions, $M_\infty = 0.9$, f=40 Hz (continued)

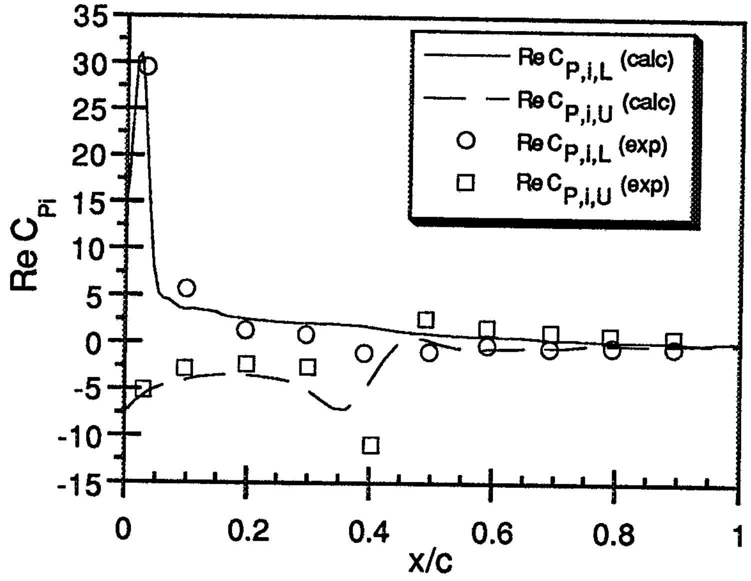

(k) Real Part, 97.7% Span

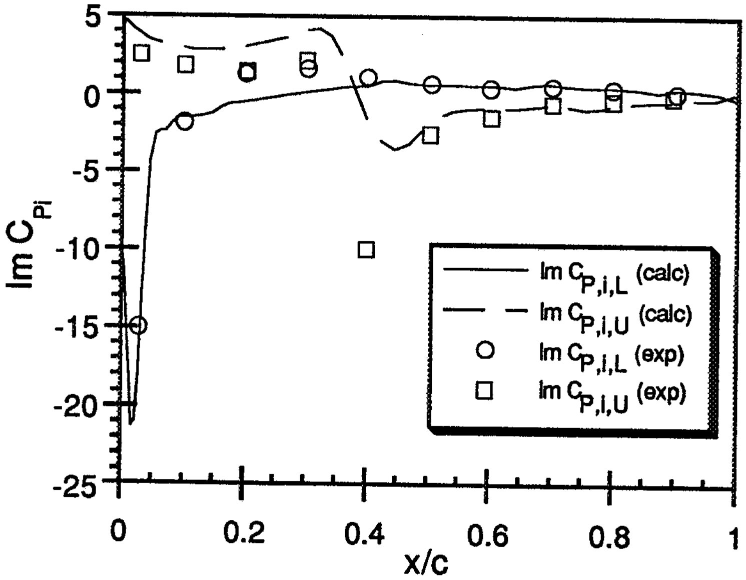

(l) Imaginary Part, 97.7% Span

Fig. 5.18: Unsteady Surface Pressure Distributions, $M_\infty = 0.9$, f=40 Hz (concluded)

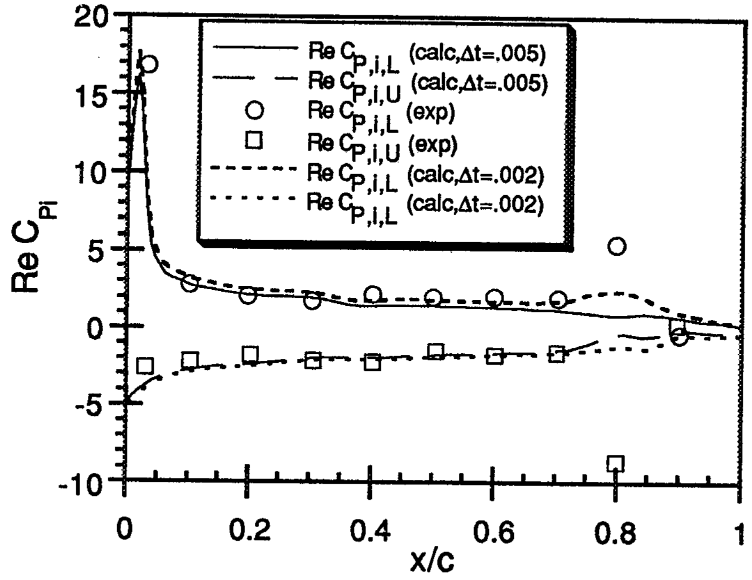

(a) Real Part, 35.2% Span

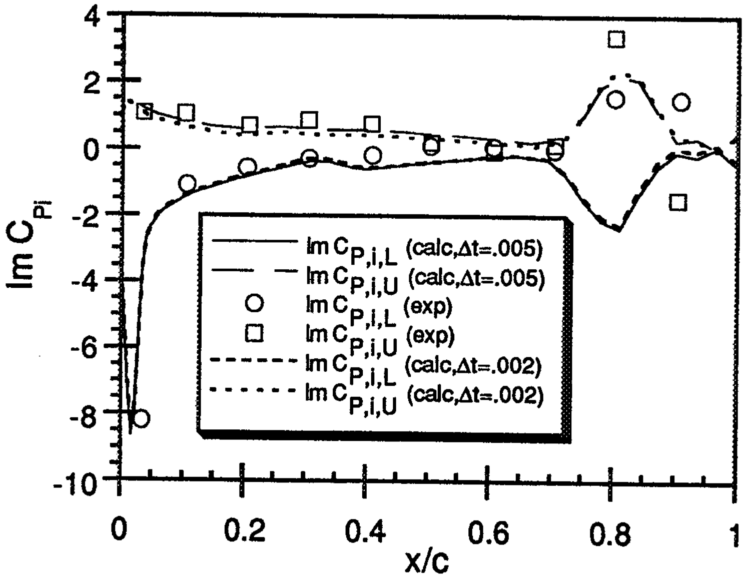

(b) Imaginary Part, 35.2% Span

Fig. 5.19: Unsteady Surface Pressure Distributions, $M_\infty = 0.95$, f=40 Hz

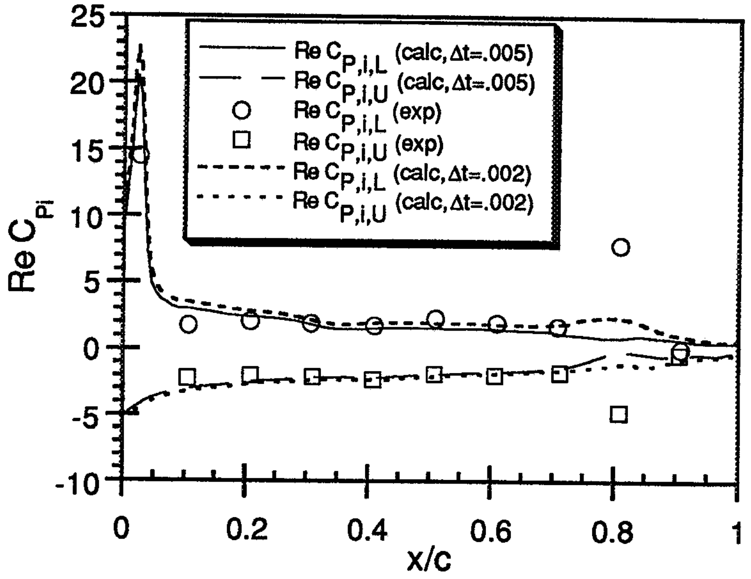

(c) Real Part, 51.2% Span

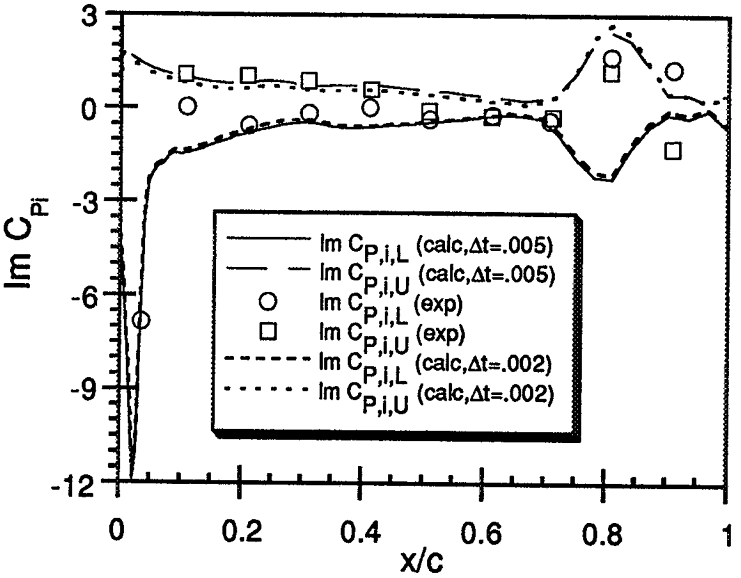

(d) Imaginary Part, 51.2% Span

Fig. 5.19: Unsteady Surface Pressure Distributions, $M_\infty = 0.95$, f=40 Hz (continued)

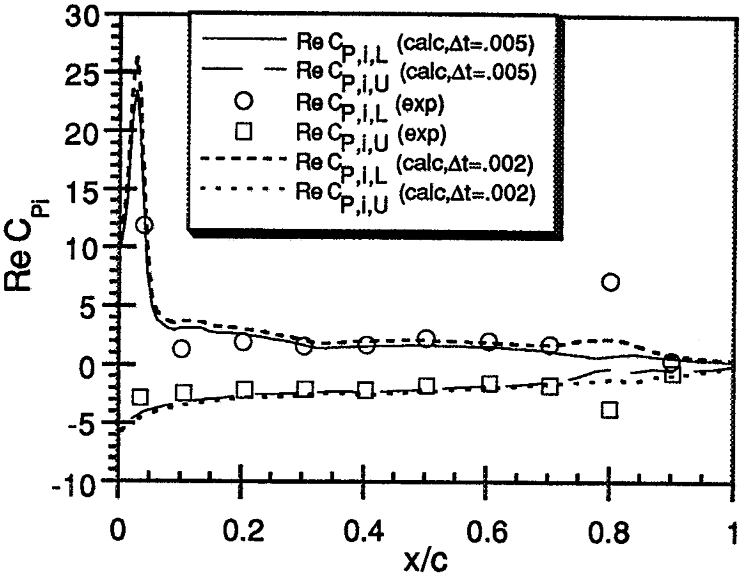

(e) Real Part, 64.1% Span

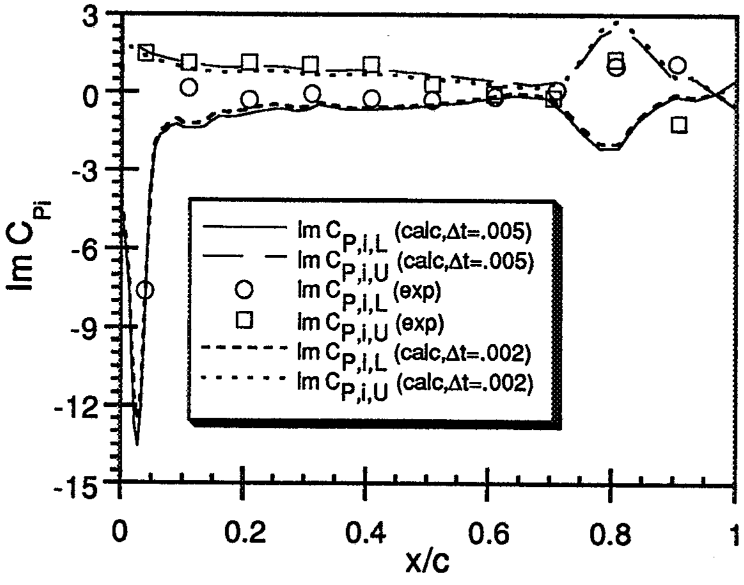

(f) Imaginary Part, 64.1% Span

Fig. 5.19: Unsteady Surface Pressure Distributions, $M_\infty = 0.95$, f=40 Hz (continued)

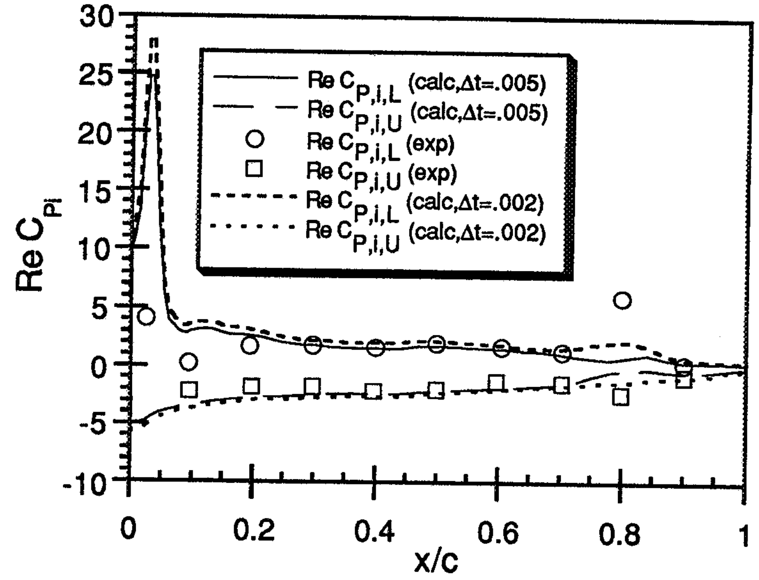

(g) Real Part, 72.1% Span

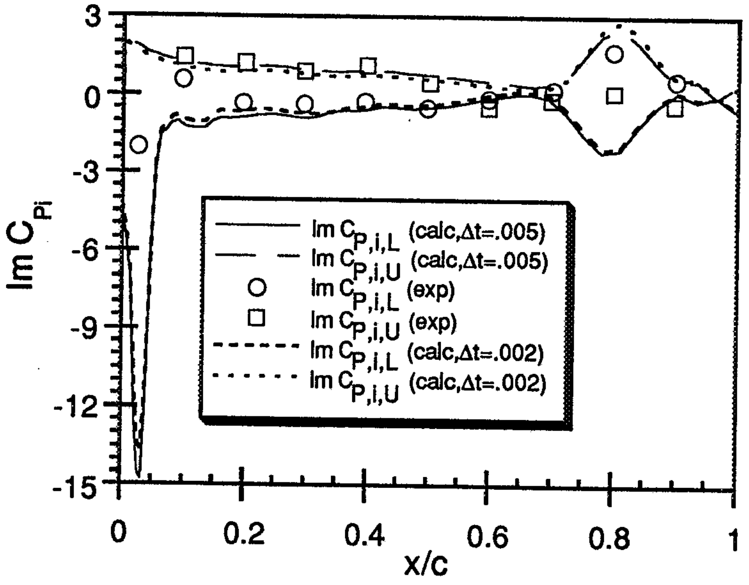

(h) Imaginary Part, 72.1% Span

Fig. 5.19: Unsteady Surface Pressure Distributions, $M_\infty = 0.95$, f=40 Hz (continued)

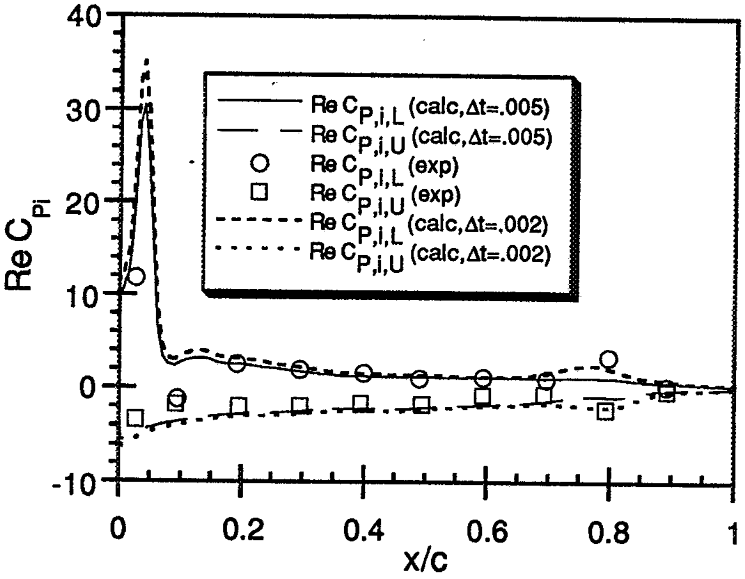

(i) Real Part, 87.5% Span

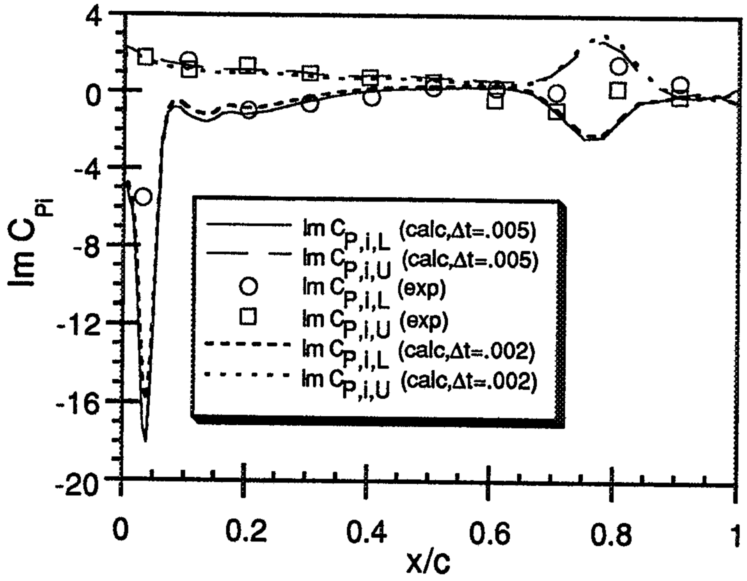

(j) Imaginary Part, 87.5% Span

Fig. 5.19: Unsteady Surface Pressure Distributions, $M_\infty = 0.95$, f=40 Hz (continued)

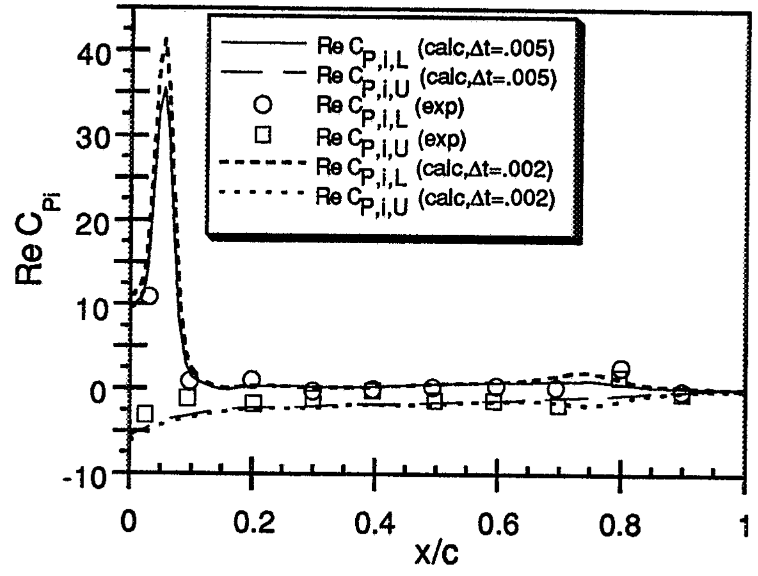

(k) Real Part, 97.7% Span

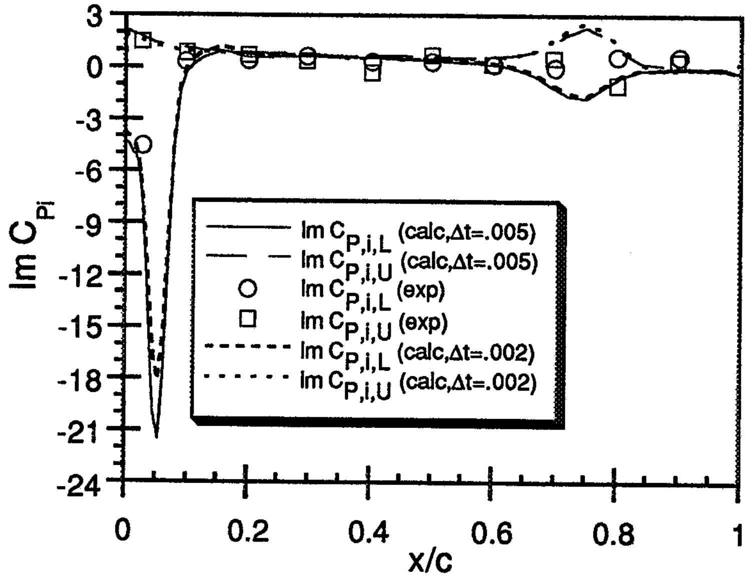

(l) Imaginary Part, 97.7% Span

Fig. 5.19: Unsteady Surface Pressure Distributions, $M_\infty = 0.95$, f=40 Hz (concluded)

CHAPTER VI

CONCLUSIONS AND RECOMMENDATIONS

6.1. Conclusions

An improved hybrid Navier-Stokes/Full-Potential method has been developed. This method has been applied to subsonic and transonic steady and unsteady flow cases. The following conclusions can be drawn from the present investigation:

- The present method is an economical way of studying steady and unsteady flows. The accuracy of Navier-Stokes computations can be retained with savings in CPU times of more than 40% in some cases.

- When coupled analysis are used, special attention must be paid to interface boundary conditions. Improper boundary conditions allow false reflections, which can slow down convergence to steady-state or lead to loss of temporal accuracy. It was found that the implementation of characteristic-based interface boundary conditions developed in the present work can adequately treat the interface, and allow signals to pass to and from one zone to another. This is especially important when shocks are present, because strong oblique disturbances must be transmitted through the interface.

- The interface boundary conditions developed in the present work are strictly valid only for steady flows. However, it has been found that they could be applied to unsteady flow cases with results similar to those obtained by full Navier-Stokes computations.

- For unsteady transonic flows, Navier-Stokes computations are clearly needed, because the strength and location of shocks are a major factor in determining unsteady loads. Full-Potential methods predict shocks aft of their actual location and overpredict their strength.

- The savings in CPU time were found to depend on the vector capability of the CPU, ranging from 27% on the Cray Y/MP-L up to 40% on a HP Apollo 700 workstation. For steady flow cases, the computational savings were slightly higher, because the hybrid method presented convergence rates higher than the full Navier-Stokes method.

6.2. Recommendations

- The present hybrid Navier-Stokes/Full Potential method has proven to be an effective way to maintain the accuracy of the Navier-Stokes simulations with substantial reductions in computational cost. The savings in CPU time were found to depend on the vector capability of the CPU, ranging from 27% on the Cray Y/MP-L up to 40% on a HP Apollo 700 workstation. For this reason, it is recommended that further improvements in vector processing machines be pursued by further vectorization of the FPE solver.

- Effective clock times could be reduced even more with respect to full Navier-Stokes computations on distributed processing machines, since the entire Full-Potential module could be solved in parallel without data exchange with the Navier-Stokes solver, for a given iteration. It is recommended that the implementation of the present hybrid method on such machines be investigated.

- It is recommended that further studies be conducted to ascertain the suitability of the interface boundary conditions developed in the present work to unsteady flows. These studies should include an investigation on the consistency of applying explicit time integration at the viscous/inviscid boundary, while using implicit solvers in the inner and outer regions.

- The shock capturing capability of the present method seems to be limited by the computational grid, in the inner region. The test case of the F-5 wing in pitching oscillations at M_∞=0.95, with a strong shock moving over the aft part of the wing, presents an opportunity for grid sensitivity studies. It is recommended that these sensitivity studies are performed, to ascertain whether the inability of the present method to predict the peak in the in-phase component of the unsteady pressure coefficients is due solely to the lack of adequate grid refinement in the aft part of the wing.

- Since the present method is modular, numerical experiments with different solvers could be undertaken. It is recommended that the ensemble FPE solver + interface boundary conditions be constructed as a 'plug-in' module to be applied to existing Navier-Stokes solvers as a means for quickly reducing the computational cost of existing Navier-Stokes methods.

- It is recommended that the present methodology be studied in connection with unstructured grid – based Navier-Stokes solvers. These methods are computationally intensive and are likely to benefit substantially from the computational savings allowed by the present technique.

In closing, it is hoped that the present hybrid technique, which combines the accuracy of Navier-Stokes methods in the viscous regions with the economy of potential flow methods in inviscid regions, will be used as a stepping stone for more ambitious efforts involving aeroelastic and unsteady aerodynamic analysis of complete aircraft configurations.

APPENDIX A

APPLICATION OF THE HYBRID NAVIER-STOKES/FULL-POTENTIAL METHOD TO AN ICED WING

In this Appendix, the application of the hybrid Navier-Stokes/Full-Potential Method to a rectangular wing with a simulated glaze ice accretion in steady flow is presented.

A.1. Configuration

The hybrid Navier-Stokes/Full-Potential Method has been applied to an unswept wing of aspect ratio 2.5 with a simulated glaze ice accretion as shown in Fig. A.1. This configuration has been experimentally studied by Bragg et al.[151–153]. The results for the same configuration without the simulated ice accretion were presented in Chapter V. The surface pressures were measured at five spanwise stations: 17%, 34%, 50%, 66% and 85% of the wing semi-span.

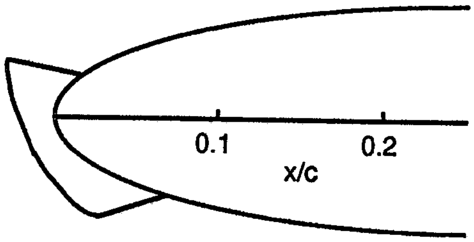

Fig. A.1: Simulated Glaze Ice Accretion

The computational grid used in the present study was an algebraic C-grid with 141 × 19 × 41 grid points, with 111 points over the airfoil (and ice) surface at each spanwise station. 14 spanwise stations were used along the wing, with 5 stations extending beyond the tip. The computational grid is illustrated in Fig. A.2. The Navier-Stokes and Full-Potential solvers were interfaced at KMATCH=20, so that about half of the number of points are located in each zone. The Mach number was 0.12, the Reynolds number 1.5 million, and the angles of attack were 4° and 8°. The CPU time for this configuration was about 24 sec. per iteration on a Hewlett-Packard Apollo 700 workstation. The CPU time for the same configuration on Georgia Tech's Cray Y-MP/E was about 9.6 sec. per iteration. These times are about 60% of the times required for a full Navier-Stokes analysis.

A.2. Surface Pressure Distributions

The computed surface pressure distributions at the computational span stations were linearly interpolated to the span stations where experimental data is available to allow direct one-to-one comparisons[141–153]. The resulting pressure coefficient distributions for the angles of attack 4° and 8° angle of attack are shown in Fig. A.3 and

A.4, respectively. The spurious peaks near the trailing edge at all the spanwise stations are due to inadequate grid resolution in that region. A good agreement may be observed between the numerical and experimental results, except for the spurious peaks near the trailing edge as mentioned above and for the strong peaks and oscillations near the separated region. It should be noted that essentially the same results are obtained with Navier-Stokes computations. For the 4° angle of attack configuration, the length of the separation bubble appears very well predicted, although the exact chordwise location where the it starts appears displaced, except near the tip. Due to the sharp pressure variations just before the separation bubble, this slight displacement causes the pressure level along the separated region to be somewhat underpredicted. For the 8° angle of attack configuration, the displacement of chordwise location where the separation bubble starts is observed only inboard, but the length of the separation bubble is not predicted as well as for the 4° configuration.

It should be noted that the experimental results used here were obtained with a small clearance between the upper and lower wind-tunnel walls and the wing surface. Consequently, wind-tunnel wall interference may partially account for the discrepancies noted above.

Further insight can be obtained by analyzing the lift coefficient distribution along the span, shown in Fig. A.5. Interestingly, the underprediction of lift due to the lower suction peak, observed for the clean wing configuration, is not observed for the 4° angle of attack iced configuration. This may be attributed to the sharp variation of pressure coefficient with formation of the separation bubble near the leading edge. Since the suction peak occurs in a much narrower region than in the non-iced configuration, the actual peak value becomes less important for the section lift. The underprediction of lift at 8° angle of attack iced configuration at inboard stations, in turn, appears to be due to the inaccurate prediction of the start of the separation bubble, associated with its relatively longer length for this configuration.

Overall, it is observed that our current results correlate well with experiments and are consistent with those obtained by a full Navier-Stokes code[8–10], while consuming only about 60% of the CPU time.

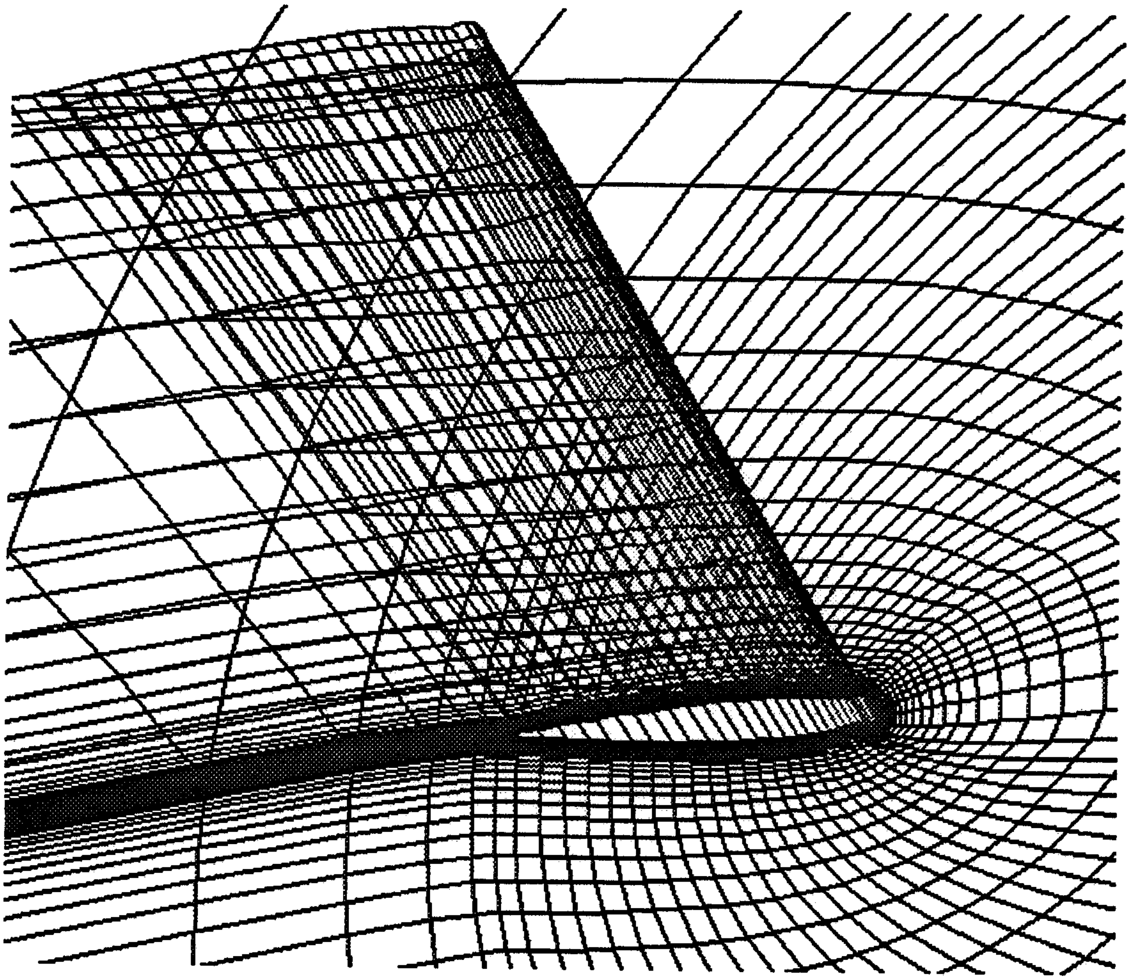

Fig. A.2: Computational Grid for Rectangular Wing with Simulated Glaze Ice Accretion

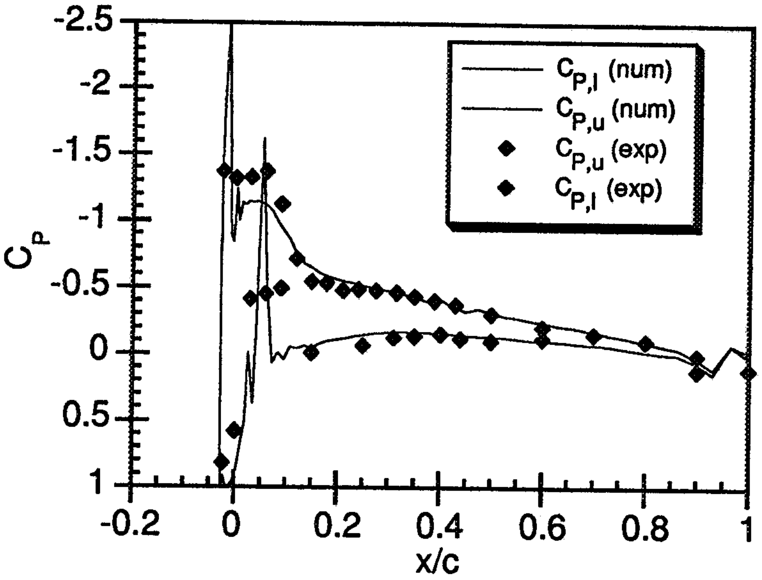

(a) 17% Span

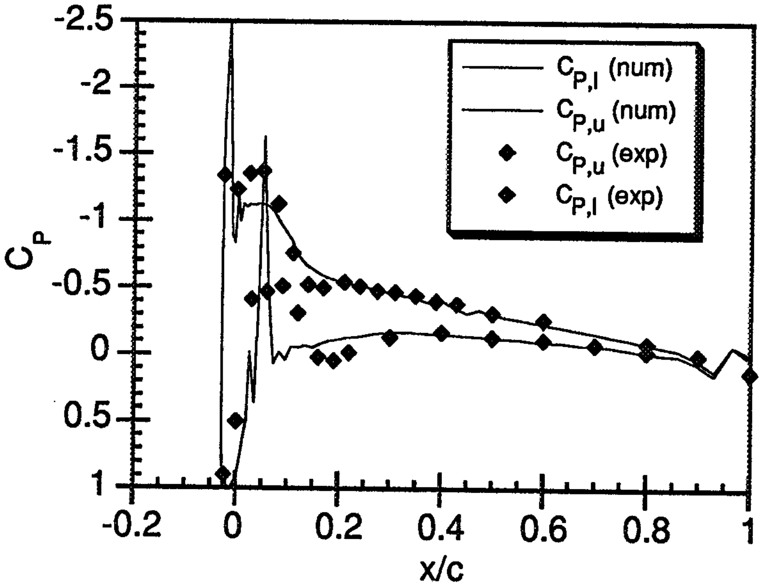

(b) 34% Span

Fig. A.3: Surface Pressure Distributions for Iced Wing at $\alpha=4°$

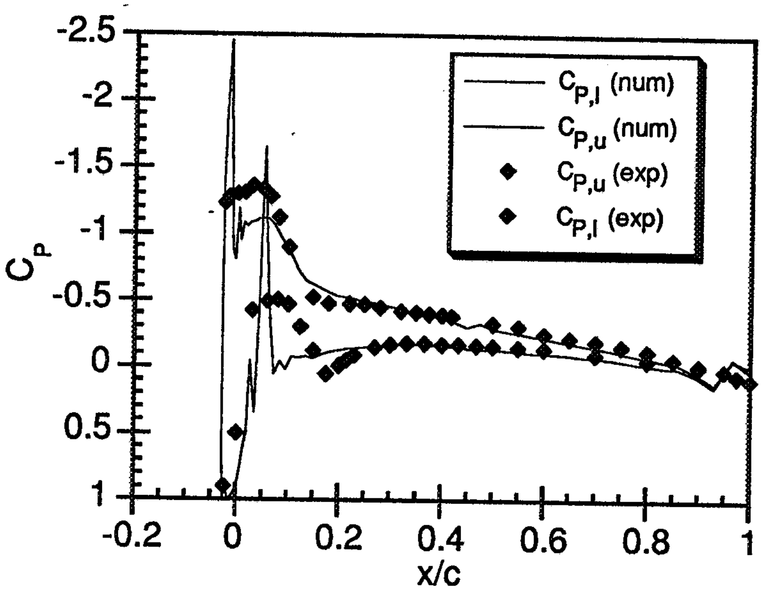

(c) 50% Span

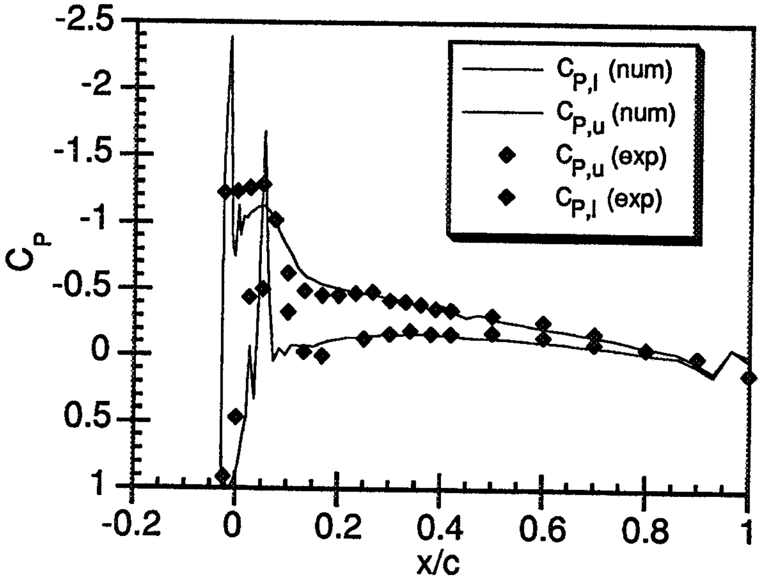

(d) 66% Span

Fig. A.3: Surface Pressure Distributions for Iced Wing at α=4° (continued)

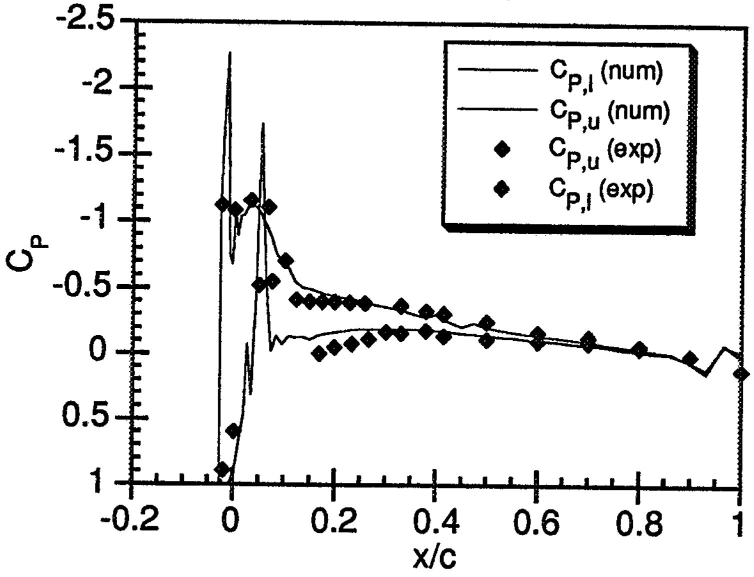

(e) 85% Span

Fig. A.3: Surface Pressure Distributions for Iced Wing at α=4° (concluded)

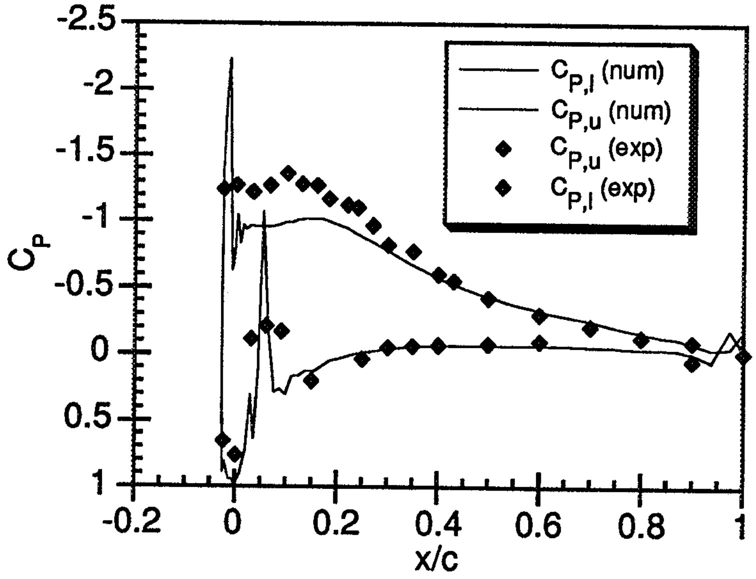

(a) 17% Span

Fig. A.4: Surface Pressure Distributions for Iced Wing at α=8°

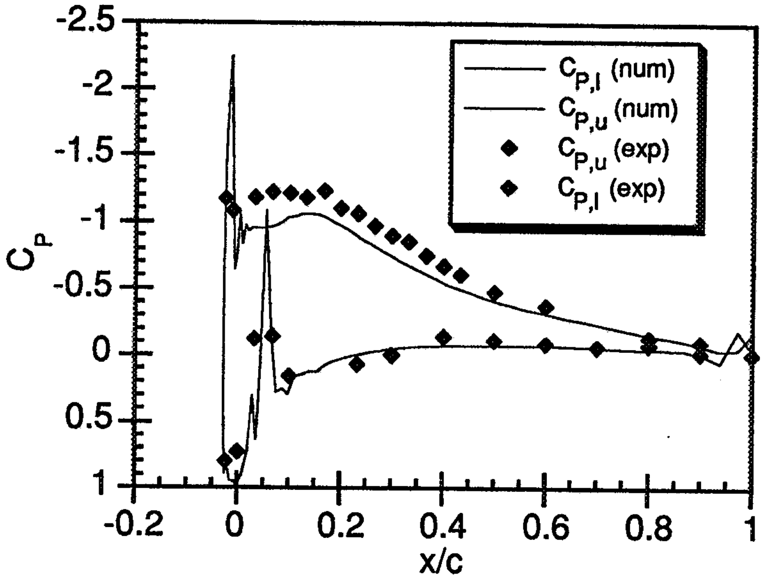

(b) 34% Span

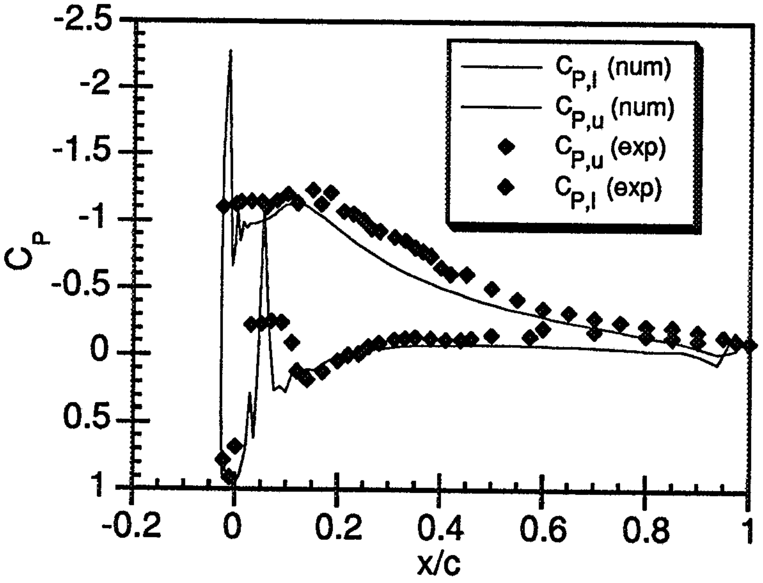

(c) 50% Span

Fig. A.4: Surface Pressure Distributions for Iced Wing at α=8° (continued)

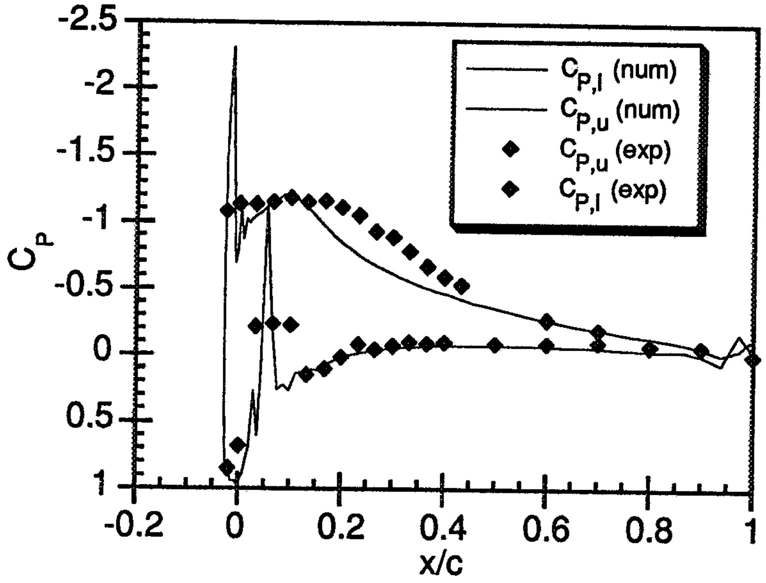

(d) 66% Span

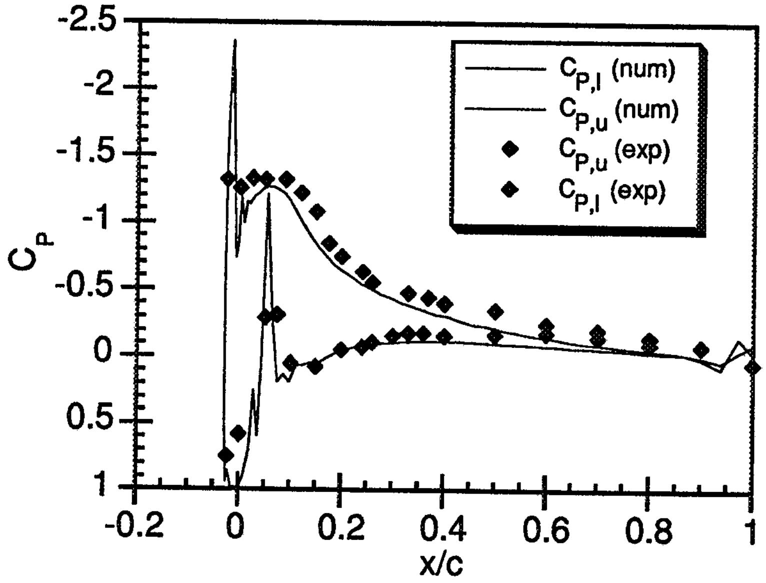

(e) 85% Span

Fig. A.4: Surface Pressure Distributions for Iced Wing at α=8° (concluded)

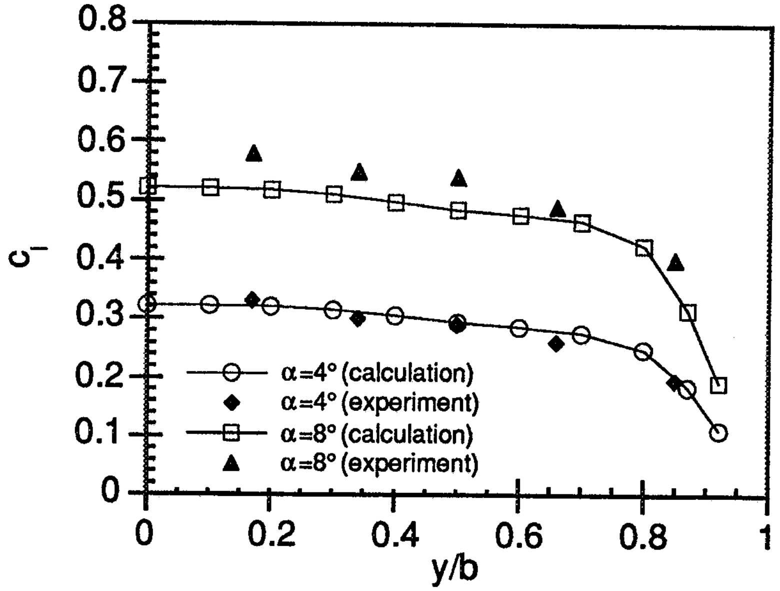

Fig. A.5: Lift Distribution for Iced Wing at α=4 and 8°

REFERENCES

1. Sankar, L. N., Bharadvaj, B. K. , and Tsung, F.-L., "A Three-Dimensional Navier-Stokes/Full-Potential Coupled Analysis for Viscous Transonic Flow," AIAA Paper 91-1595-CP, AIAA 10th Computational Fluid Dynamics Conference, Honolulu, Hawaii, June 1991; also *AIAA Journal*, Vol. 31, No. 10, October 1993.
2. Whitlow, W., Jr., "Computational Unsteady Aerodynamics for Aeroelastic Analysis," NASA TM-100523, December 1987.
3. Tsung, F.-L., Ph.D. Dissertation (in preparation), Georgia Institute of Technology, Atlanta, 1994.
4. Sankar, L. N., Malone, J. B., and Tassa, Y., "An Implicit Conservative Algorithm for Steady and Unsteady Three-Dimensional Transonic Potential Flows," AIAA Paper 81-1016. Proceedings of the AIAA Fifth Computational Fluid Dynamics Conference, Palo Alto, CA, June 1981, pp. 199–212.
5. Sankar, N. L., and Malone, J. B., "Solution Techniques for the Steady and Unsteady Transonic Full Potential Equation," Advances in Computational Transonics, edited by W. G. Habashi (Vol. 4 of *Recent Advances in Numerical Methods in Fluids)*, Pineridge Press, Swansea, Wales, 1985.
6. Wake, B. E., and Sankar, L. N., "Solution of Navier-Stokes Equations for the Flow About a Rotor Blade," *Journal of the American Helicopter Society*, Vol. 34, No. 2, 1989, pp. 13–23.
7. Sankar, L. N., and Kwon, O. J., "High-Alpha Simulation of Fighter Aircraft," Proceedings of the NASA High Angle-of-Attack Technology Conference, Vol. 1, NASA CP-3149, Pt. 2, NASA Langley Research Center, Hampton, VA, November 1990, pp. 689–702.
8. Kwon, O. J., and Sankar, L. N., "Numerical Study of the Effect of Icing on Finite Wing Aerodynamics," AIAA Paper 90-0757, January 1990.
9. Kwon, O. J., and Sankar, L. N., "Numerical Study of the Effect of Icing on Fixed and Rotary Wing Performance," AIAA Paper 91-0662, January 1991.
10. Kwon, O. J., and Sankar, L. N., "Numerical Investigation of Performance Degradation of Wings and Rotors Due to Icing," AIAA Paper 92-0412, January 1992.

11. Kwon, O.J. and Sankar, L.N., "Viscous Flow Simulation of a Fighter Aircraft," *Journal of Aircraft*, Vol. 29, No. 5, Sep-Oct. 1992, pp. 886–891.

12. Sankar, L. N., Phaengsook, N., and Bangalore, A., "Effects of Icing on the Aerodynamic Performance of High Lift Airfoils," AIAA Paper 93-0026, January 1993.

13. Pulliam, T. H., and Chaussee, D. S., "A Diagonal Form of an Implicit Approximate-Factorization Algorithm," *Journal of Computational Physics*, Vol. 39, 1981, pp. 347–363.

14. Beam, R. M. and Warming, R. F., "An Implicit Factored Scheme for the Compressible Navier-Stokes Equations," *AIAA Journal*, Vol. 16, April 1978, pp. 393–402.

15. Ballhaus, W. F., "Some Recent Progress in Transonic Flow Computations," In: Numerical Methods in Fluid Dynamics, Edited by H. J. Wirz and J. J. Smolderen, Hemisphere Publishing Co., Washington, DC, 1978, pp. 155–235.

16. Schmidt, W., "Progress in Transonic Flow Computations: Analysis and Design Methods for Three-Dimensional Flows," In: Numerical Methods in Fluid Dynamics, Edited by H. J. Wirz and J. J. Smolderen, Hemisphere Publishing Co., Washington, DC, 1978, pp. 155–235.

17. Edwards, J. and Malone, J., "Current Status of Computational Methods for Transonic Unsteady Aerodynamics and Aeroelastic Applications," In: Transonic Unsteady Aerodynamics and Aeroelasticity, AGARD CP-507, March 1992.

18. Caradonna, F. X., "Application of Transonic Flow Analysis to Helicopter Rotor Problems," In: Unsteady Transonic Aerodynamics, Edited by D. Nixon, *Progress in Astronautics and Aeronautics*, Vol. 120, American Institute of Aeronautics and Astronautics, Washington, DC, 1989, pp. 263–285.

19. Verdon, J. M., "Unsteady Aerodynamics for Turbomachinery Aeroelastic Applications," In: Unsteady Transonic Aerodynamics, Edited by D. Nixon, *Progress in Astronautics and Aeronautics*, Vol. 120, American Institute of Aeronautics and Astronautics, Washington, DC, 1989, pp. 287–347.

20. Azevedo, J. L. F., "Transonic Aeroelastic Analysis of Launch Vehicle Configurations," Ph.D. Dissertation, Department of Aeronautics and Astronautics, Stanford University, February 1988. (Also NASA CR-4186, October 1988).

21. Mabey, D. G., "Physical Phenomena Associated with Unsteady Transonic Flows," In: Unsteady Transonic Aerodynamics, Edited by D. Nixon, *Progress in Astronautics and Aeronautics*, Vol. 120, American Institute of Aeronautics and Astronautics, Washington, DC, 1989, pp. 1–55.

22. Landahl, M. T., Unsteady Transonic Flow, Pergamon Press, New York, 1951.

23. Bisplinghoff, R. L., Ashley, H. and Halfman, R. L., Aeroelasticity, Addison-Wesley, 1955.

24. Tijdeman, H. and Destuynder, R., Comments on Transonic and Wing-Store Unsteady Aerodynamics, AGARD-R-636, January 1976.

25. Ashley, H., "Role of Shocks in the 'Sub-Transonic' Flutter Phenomenon," *Journal of Aircraft*, Vol. 17, No. 3, March 1980, pp. 187.

26. Tijdeman, H., and Seebass, R., "Transonic Flow Past Oscillating Airfoils," *Annual Review of Fluid Mechanics*, Vol. 12, 1980, pp. 181–222.

27. R. Goorjian, P. M., "Computations of Unsteady Transonic Flow," In: Advances in Computational Transonics, edited by W. G. Habashi (Vol. 4 of *Recent Advances in Numerical Methods in Fluids)*, Pineridge Press, Swansea, Wales, 1985.

28. McCroskey, W. J., Kutler, and Bridgeman, J. O., "Status and Prospects of Computational Fluid Dynamics for Unsteady Transonic Viscous Flows," In: Transonic Unsteady Aerodynamics and its Aeroelastic Applications, AGARD CP-374, 1985.

29. Edwards, J. W., and Thomas, J. L., Computational Methods for Unsteady Transonic Flows, AIAA Paper 87-0107, January 1987. Also in: Unsteady Transonic Aerodynamics, Edited by D. Nixon, *Progress in Astronautics and Aeronautics*, Vol. 120, American Institute of Aeronautics and Astronautics, Washington, DC, 1989, pp. 211–261.

30. Hixon, R., "Application of a Generalized Minimum Residual Method to the Calculation of 2D and 3D Unsteady Flows," Ph.D. Dissertation, Georgia Institute of Technology, Atlanta, April 1993.

31. Mykytow, W. J., "Transonic Unsteady Aerodynamics and its Aeroelastic Applications," In: Unsteady Aerodynamics — Fundamentals and Applications to Aircraft Dynamics, AGARD CP-386, 1985.

32. Mabey, D. G., and Chambers, J. R., "Unsteady Aerodynamics — Fundamentals and Applications to Aircraft Dynamics," AGARD AR-222, May 1985.

33. Edwards, J. T., "Technical Evaluation Report on 1991 Specialists' Meeting on Transonic Unsteady Aerodynamics and Aeroelasticity," In: Transonic Unsteady Aerodynamics and Aeroelasticity, AGARD CP-507, March 1992.

34. Mykytow, W. J., "A Brief Overview of Transonic Flutter Problems," In: Unsteady Airloads in Separated and Transonic Flow, AGARD CP-226, July 1977.

35. Albano, E. and Rodden, W. P., "A Doublet-Lattice Method for Calculating Lift Distributions on Oscillating Surfaces in Subsonic Flows," *AIAA J.*, Vol. 7, 1969, pp. 279–285.

36. Kraus, W., "Panel Methods in Aerodynamics," In: Numerical Methods in Fluid Dynamics, Edited by H. J. Wirz and J. J. Smolderen, Hemisphere Publishing Co., Washington, DC, 1978, pp. 237–297.

37. Murman, E. M. and Cole, J. D., "Calculation of Plane Steady Transonic Flows," *AIAA Journal*, Vol. 9, 1971, pp. 114–121.

38. Ehlers, F. E., "A Finite Difference Method for Solution of Transonic Flow about Harmonically Oscillating Wings," NASA CR-2257, July 1974. OK

39. Ballhaus, W. F., and Lomax, H., "The Numerical Simulation of Low Frequency Unsteady Transonic Flow Fields," In: *Lecture Notes in Physics*, Vol. 35, Springer-Verlag, New York, 1975, pp. 57–63.

40. Ballhaus, W. F., and Steger, J. L., "Implicit Approximate-Factorization Schemes for the Low-Frequency Transonic Equation," NASA TM-X-73082, Nov. 1975. OK

41. Ballhaus, W. F. and Goorjian, P. M., "Implicit Finite Difference Computations of Unsteady Transonic Flows about Airfoils", *AIAA Journal*, Vol. 15, Dec. 1977, pp. 1728–1735.

42. Tijdeman, H., Schippers, P., and Persoon, A. J., "Unsteady Airloads on an Oscillating Supercritical Airfoil," In: Unsteady Airloads in Separated and Transonic Flow, AGARD CP-226, July 1977.

43. Tijdeman, H., van Nunen, J. W. G., Kraan, A. N., Persoon, A. J., Poestkoke, R., Roos, R., Schippers, P., and Siebert, C. M., "Transonic Wind Tunnel Tests on an Oscillating Wing with External Stores, Part I: General Description," Air Force Flight Dynamics Laboratory, AFFDL-TR-78-194, Part I, Wright-Patterson AFB, Ohio, December 1978. (Also NLR-TR-78106-U, Part I)

44. Tijdeman, H., van Nunen, J. W. G., Kraan, A. N., Persoon, A. J., Poestkoke, R., Roos, R., Schippers, P., and Siebert, C. M., "Transonic Wind Tunnel Tests on an Oscillating Wing with External Stores, Part II: Clean Wing," Air Force Flight Dynamics Laboratory, AFFDL-TR-78-194, Part II, Wright-Patterson AFB, Ohio, March 1979. (Also NLR-TR-78106-U, Part II)

45. Bland, S. R., "AGARD Two-Dimensional Aeroelastic Configurations," AGARD-AR-156, 1979.

46. Bland, S. R., "AGARD Three-Dimensional Aeroelastic Configurations," AGARD-AR-167, 1982.

47. Lambourne, N. C., "Compendium of Unsteady Aerodynamic Measurements," AGARD Report No. 702, 1982.

48. Magnus, R. and Yoshihara, H., "Unsteady Transonic Flow over an Airfoil," *AIAA Journal*, Vol. 14, Dec. 1975, pp. 1622–1628.

49. Lerat, A., and Sidès, J., "Calcul Numérique d'Écoulements Transsoniques Instationnaires," In: Unsteady Airloads in Separated and Transonic Flow, AGARD CP-226, July 1977.

50. Goorjian, P. M., "Implicit Computations of Unsteady Transonic Flow Governed by the Full Potential Equation in Conservative Form", AIAA Paper 80-0150, Jan. 1980.

51. Sankar, N.L. and Tassa, Y., "An Algorithm for Unsteady Transonic Potential Flow Past Airfoils", Proceedings of the Seventh International Conference on Numerical Methods in Fluid Dynamics, Stanford University, June 1980, p.367–372.

52. Shankar, V., Ide, H., Gorski, J., and Osher, S., "A Fast, Time-Accurate, Unsteady Full Potential Scheme," *AIAA Journal,* Vol. 25, No. 2, Feb. 1987, pp. 230-238. (Also AIAA Paper 85-1512).

53. Malone, J. B., Ruo, S. Y., and Sankar, N. L., "Computation of Unsteady Transonic Flows about Two-Dimensional and Three-Dimensional AGARD Standard Configurations," In: Transonic Unsteady Aerodynamics and its Aeroelastic Applications, AGARD CP-374, 1985.

54. Malone, J. B., Sankar, L. N., and Sotomayer, W. A., "Unsteady Aerodynamic Modeling of a Fighter Wing in Transonic Flow," Journal of Aircraft, Vol. 23, No. 8, August 1986, pp. 611–620.

55. Hafez, M., and Lovell, D., "Entropy and Vorticity Corrections for Transonic Flows," AIAA Paper 83-1926.

56. Osher, S., Hafez, M., and Whitlow, W., Jr., "Entropy Correction Satisfying Approximations for the Full Potential Equation of Transonic Flow," *Mathematics of Computation,* Vol. 44, No. 169, Jan. 1985, pp. 1–29.

57. Hafez, M., Whitlow, W., Jr., and Osher, S., "Improved Finite-Difference Schemes for Transonic Potential Flow Calculations," *AIAA Journal,* Vol. 25, No. 11, Nov. 1987.

58. Whitlow, W., Jr., Hafez, M., and Osher, S., "An Entropy Correction Method for Unsteady Full Potential Flows with Strong Shocks," *Journal of Fluids and Structures*, Nov. 1987.

59. Whitlow, W., "Application of a Nonisentropic Full Potential Method to AGARD Standard Airfoils," AIAA Paper 88-0710, Jan. 1988.

60. Kwak, D., "Nonreflecting Far-Field Boundary Conditions for Unsteady Transonic Flow Computations," *AIAA Journal*, Vol. 19, No. 11, Nov. 1981, pp. 1401-1407.

61. Whitlow, W., Jr., and Seidel, D. A., "Nonreflecting Boundary Conditions for the Complete Unsteady Transonic Small-Disturbance Equation, *AIAA Journal*, Vol. 23, No. 2, Feb. 1985, pp. 315-317.

62. Rizzetta, D. P., and Yoshihara, H., "Oscillating Supercritical Airfoils in the Transonic Regime with Viscous Interactions," In: Boundary Layer Effects on Unsteady Airloads, AGARD CP-296, February 1981.

63. Couston, M., Angélini, J. J., and Mulak, P., "Application de l'Équation des Petites Perturbations Transsoniques aux Calculs d'Écoulements Bidimensionnels Instationnaires," La Recherche Aérospatiale, 1979, No. 5, pp. 325–341.

64. Couston, M., Angélini, J. J., Le Balleur, J.-C., and Girodroux-Lavigne, P., "Prise en Compte d'Effets de Couche Limite Instationnaire dans un Calcul Bidimensionnel Transsonique," In: Boundary Layer Effects on Unsteady Airloads, AGARD CP-296, February 1981.

65. Le Balleur, J.-C., "Numerical Viscous-Inviscid Interaction in Steady and Unsteady Flows," In: Numerical and Physical Aspects of Aerodynamic Flows II, Edited by T. Cebeci, Springer-Verlag, Berlin, 1984.

66. Rizzetta, D. P., and Borland, C. J., "Numerical Solution of 3-D Unsteady Transonic Flow over Wings," AIAA Paper 80-1369, July 1980.

67. Borland, C. J., Rizetta, D. P., and Yoshihara, H., "Numerical Solution of Three-Dimensional Unsteady Transonic Flow over Swept Wings," *AIAA Journal*, Vol. 20, March 1982, pp. 340–347.

68. Borland, C. J., and Rizetta, D. P., "Nonlinear Transonic Flutter Analysis," *AIAA Journal*, Vol. 20, November 1982, pp. 1606–1615.

69. Edwards, J. W., Bland, S. R., and Seidel, D. A., "Experience with Transonic Unsteady Aerodynamic Calculations," In: Transonic Unsteady Aerodynamics and its Aeroelastic Applications, AGARD CP-374, January 1985.

70. Goorjian, P. M., and Guruswamy, G. P., "Unsteady Transonic Aerodynamic and Aeroelastic Calculations about Airfoils and Wings," In: Transonic Unsteady Aerodynamics and its Aeroelastic Applications, AGARD CP-374, January 1985.

71. Guruswamy, G. P., Goorjian, P. M., and Tu, E., "Transonic Aeroelasticity of Wings with Tip Stores," *Journal of Aircraft*, Vol. 24, No. 10, Oct. 1987, pp. 688–695.

72. Goorjian, P. M., and Guruswamy, G. P., "Unsteady Transonic Flow Simulation on a Full-Span-Wing-Body Configuration," AIAA Journal, Vol. 26, No. 12, December 1988, pp. 1450–1456.

73. Batina, J.T., "Efficient Algorithm for Solution of the Unsteady Transonic Small-Disturbance Equation," *Journal of Aircraft*, Vol. 25, No. 7, July 1988, p. 598–605.

74. Cunningham, H.J, Batina, J.T., and Bennett, R.M., "Modern Wing-Flutter Analysis by Computational Fluid Dynamics Methods," *Journal of Aircraft*, Vol. 25, No. 10, Oct. 1988, pp. 962–968.

75. Batina, J.T., Seidel, D.A., Bland, S.R., and Bennett, R.M., "Unsteady Transonic Flow Calculations for Realistic Aircraft Configurations," *Journal of Aircraft*, Vol. 26, No. 1, Jan. 1989, pp. 21–28.

76. Batina, J.T., "Unsteady Transonic Algorithm Improvements for Realistic Aircraft Applications," *Journal of Aircraft*, Vol. 26, No. 2, Feb. 1989, pp. 131–139.

77. Batina, J.T., "Unsteady Transonic Small-Disturbance Theory Including Entropy and Vorticity Effects,"*Journal of Aircraft*, Vol. 26, No. 6, June 1989, pp. 531–538.

78. Bennett, R.M., Batina, J.T., and Cunningham, H.J., "Wing-Flutter Calculations with the CAP-TSD Unsteady Transonic Small-Disturbance Program," *Journal of Aircraft*, Vol. 26, No. 9, Sept. 1989, p.876–882.

79. Steger, J. L., "Implicit Finite Difference Simulation of Flow about Arbitrary Two-Dimensional Geometries," *AIAA Journal*, Vol. 16, July 1978, pp. 679–86.

80. Levy, L. L., "Experimental and Computational Steady and Unsteady Transonic Flows About a Thick Airfoil," *AIAA Journal*, Vol. 16, No. 6, June 1978, pp. 564–572.

81. Levy, L. L., and Bailey, H. E., "Computation of Airfoil Buffet Boundaries," *AIAA Journal*, Vol. 19, December 1981, pp. 1488–1490.

82. Steger, J. L., "Calculation of Transonic Aileron Buzz," AIAA Paper 79-0134, January 1979.

83. Sankar, L. N., Malone, J. B., and Schuster, D. M., "Euler Solutions for Transonic Flow Past a Fighter Wing," *Journal of Aircraft*, Vol. 24, No. 1, Jan. 1987, pp. 10–16.

84. Sotomayer, W. A., Sankar, L. N., and Malone, J. B., "A Comparison of Numerical Algorithms for Unsteady Transonic Flow," *Computer Methods in Applied Mechanics and Engineering*, Vol. 64, Nos.1–3, October 1987, pp. 237–265.

85. Sankar, L. N., Wake, B. E., and Lekoudis, S. G, "Solution of the Unsteady Euler Equations for Fixed and Rotor Wing Configurations," *Journal of Aircraft*, Vol. 23, No. 4, April 1986, pp. 283–289.

86. Pulliam, T. H., and Steger, J. L., "Implicit Finite-Difference Simulations of Three-Dimensional Compressible Flow," *AIAA Journal*, Vol. 18, 1980, pp. 159–167.

87. Smith, M. and Sankar, L. N., "Evaluation of a Fourth-Order Compact Operator Scheme for Euler/Navier-Stokes Simulations of a Rotor in Hover," AIAA Paper 91-0766, Jan. 1991.

88. Tseng, W., Tsung, F.-L., and Sankar, L. N., "Numerical Simulation of Dynamic Lift Enhancement Using Oscillatory Leading Edge Flaps," AIAA Paper 93-0177, 31st AIAA Aerospace Sciences Meeting and Exhibit, Reno, NV, January 11-14, 1993.

89. Roe, P. L., "Approximate Riemann Solvers, Parameter Vectors and Difference Schemes," *Journal of Computational Physics*, Vol. 43, 1981, pp. 357–372.

90. Roe, P. L., "Characteristic-Based Schemes for the Euler Equations," *Annual Review of Fluid Mechanics,* Vol. 18, 1986, pp. 337–365.

91. Bangalore, A., Phaengsook, N., and Sankar, L. N., "Application of a Third Order Upwind Scheme to Viscous Flow over Clean and Iced Wings," AIAA Paper 94-0485, January 1994.

92. Hariharan, N., and Sankar, L. N., "Higher Order Numerical Simulation of Rotor Flow Field," 50th Annual Forum of the American Helicopter Society, May 1994.

93. Berezin, C. R., "An Improved Navier-Stokes/Full-Potential Coupled Analysis for Rotors," AIAA Paper 94-0736, January 1994.

94. Hixon, R., Tsung, F.-L., and Sankar, L. N., "Comparison of Two Methods for Solving Three-Dimensional Unsteady Compressible Viscous Flows," *AIAA Journal*, Vol. 32, No. 10, October 1994.

95. Guruswamy, G.P., "Unsteady Aerodynamic and Aeroelastic Calculations of Wings Using Euler Equations," *AIAA Journal*, Vol. 28, No. 3, March 1990, pp. 461–469.

96. Holst, T. L., Kaynak, U., Gundy, K. L., Thomas, S. D., Flores, J., and Chaderjian, N. M., "Transonic Wing Flows Using an Euler/Navier-Stokes Zonal Approach," *Journal of Aircraft*, Vol. 24, No. 1, Jan 1987, pp. 17–24.

97. Kaynak, U., Holst, T. L., Cantwell, B. J., Sorenson, R. L., "Numerical Simulation of Transonic Separated Flows over Low Aspect Ratio Wings," *Journal of Aircraft*, Vol. 24, No. 8, August 1987, pp. 531–539.

98. Flores, J., Reznick, S. G., Holst, T. L., and Gundy, K., "Transonic Navier-Stokes Solutions for a Fighter-Like Configuration," *Journal of Aircraft*, Vol. 25, No. 10, pp. 875–881.

99. Steger, J. L., and Warming, R. F., "Flux Vector Splitting of the Inviscid Gasdynamic Equations with Application to Finite-Difference Methods," *Journal of Computational Physics*, Vol. 40, No. 2, April 1980, pp. 263–293.

100. van Leer, B., "Flux-Vector Splitting for the Euler Equations," *Lecture Notes in Physics*, Vol. 170, 1982, pp. 507–512.

101. Thomas, J. L., Van Leer, B., and Walters, R. W., "Implicit Split-Flux Schemes for the Euler Equations," AIAA Paper 85-1680, July 1985. Also *AIAA Journal*, Vol. 28, No. 6, June 1990, pp. 973–974.

102. Anderson, W. K., Thomas, J. L., and Van Leer, B., "Comparison of Finite Volume Flux Vector Spittings for the Euler Equations," *AIAA Journal*, Vol. 24, No. 9, Sept. 1986, pp. 1453–1460.

103. Anderson, W. K., and Thomas, J. L., "Multigrid Acceleration of the Flux-Split Euler Equations," *AIAA Journal*, Vol. 26, No. 6, June 1988, pp. 649–654.

104. Anderson, W. K., Thomas, J. L., and Rumsey, C. L., "Extension and Applications of Flux-Vector Splitting to Unsteady Calculations on Dynamic Meshes," AIAA Paper 87-1152, 1987.

105. Thomas, J. L., Krist, S. T., and Anderson, W. K., "Navier-Stokes Computations of Vortical Flows over Low Aspect Ratio Wings," *AIAA Journal*, Vol. 28, No. 2, Feb. 1990, pp. 205–212.

106. Biedron, R. T., and Thomas, J. L., "Navier-Stokes Computations for an F/A-18 Forebody with Actuated Control Strake," Proceedings of the NASA High Angle-of-Attack Technology Conference, Vol. 1, NASA CP-3149, Pt. 1, NASA Langley Research Center, November 1990. ok

107. Luckring, J. M., Ghaffari, F., and Bates, B. L., "Status of Navier-Stokes Computations about the F/A-18 with Structured Grids," Proceedings of the NASA High Angle-of-Attack Technology Conference, Vol. 1, NASA CP-3149, Pt. 2, NASA Langley Research Center, November 1990. ok

108. Rizk, Y., Schiff, L. B., and Gee, K., "Numerical Simulation of the High Angle of Attack Flow Around the F-18 Aircraft," Proceedings of the NASA High Angle-of-Attack Technology Conference, Vol. 1, NASA CP-3149, Pt. 2, NASA Langley Research Center, November 1990, pp. 723–735. ok

109. Berger, M. J., "Data Structures for Adaptive Grid Generation," *SIAM Journal of Scientific and Statistical Computing*, Vol. 7, No. 3, July 1986, pp. 904–916.

110. Barth, T., "Aspects of Unstructured Grids and Finite-Volume Solvers for the Euler and Navier-Stokes Equations," In: Special Course on Unstructured Grid Methods for Advection Dominated Flows, AGARD Report 787, May 1992.

111. Löhner, R., "An Adaptive Finite Element Scheme for Transient Problems in CFD," *Computer Methods in Applied Mechanics and Engineering*, Vol. 61, 1987, pp. 323–338.

112. Mavriplis, D. J., "Adaptive Mesh Generation for Viscous Flows Using Delaunay Triangulation," Journal of Computational Physics, Vol. 90, 1990, pp. 271–291.

113. Müller, J.-D., Roe, P. L., and Deconinck, H., "A Frontal Approach for Node Generation in Delaunay Triangulation," In: Special Course on Unstructured Grid Methods for Advection Dominated Flows, AGARD Report 787, May 1992.

114. Batina, J., "Accuracy of an Unstructured -Grid Upwind-Euler Algorithm for the ONERA M6 Wing," *Journal of Aircraft*, Vol. 28, No. 6, June 1991, pp. 397–402.

115. Batina, J., "Implicit Flux-Split Euler Schemes for Unsteady Aerodynamic Analysis Involving Unstructured Dynamic Meshes," *AIAA Journal*, Vol. 29, No. 11, Nov. 1991, pp. 1836–1843.

116. Batina, J., Lee, E., Kleb, W., and Rausch, R., "Unstructured Grid Methods Development for Unsteady Aerodynamic and Aeroelastic Analysis," In: Transonic Unsteady Aerodynamics and Aeroelasticity, AGARD CP-507, March 1992.

117. Rausch, R., Batina, J., and Yang, H., "Spatial Adaptation Procedures on Tetrahedral Meshes for Unsteady Aerodynamic Flow Calculations," AIAA Paper 93-0670, January 1993.

118. Chaderjian, N. M., and Guruswamy, G. P., "Transonic Navier-Stokes Computations for an Oscillating Wing Using Zonal Grids," *Journal of Aircraft*, Vol. 29, No. 3, May-June, 1992, pp. 326–335.

119. Cricelli, A. S., Ekaterinaris, J. A., and Platzer, M. F., "Unsteady Airfoil Flow Solutions on Moving Zonal Grids," AIAA Paper 92-0543, 1992.

120. Obayashi, S., and Guruswamy, G. P., "Navier-Stokes Computations for Oscillating Control Surfaces," AIAA Paper 92-4431, In: AIAA Atmospheric Flight Mechanics Conference, Hilton Head Island, SC, August 10-12, 1992. Also *Journal of Aircraft*, Vol. 31, No. 3, May-June 1994.

121. Klopfer, G. H., and Obayashi, S., "Virtual Zone Navier-Stokes Computations for Oscillating Control Surfaces," AIAA Paper 93-3304, 11th AIAA Computational Fluid Dynamics Conference, Orlando, FL, July 6–9, 1993.

122. Ekaterinaris, J. A., "Effects of Spatial Order of Accuracy on the Computation of Vortical Flowfields," AIAA Paper 93-3371, 11th AIAA Computational Fluid Dynamics Conference, Orlando, FL, July 6–9, 1993.

123. Wang, Z. J., "A Unified Conservative Zonal Interface Treatment for Arbitrarily Patched and Overlapping Meshes," AIAA Paper 94-0320, January 1994.

124. Kandil, O. A., and Kamdil, H. A., "Pitching Oscillations of a 65 deg. Delta Wing in Transonic Vortex-Breakdown Flow," AIAA/ASME/ASCE/AHS/ASC 32nd Structures, Structural Mechanics and Materials Conference, Hilton Head, SC, April 18–20, 1994.

125. Chardejian, N., and Schiff, L., "Navier-Stokes Prediction of Coupled/Large Amplitude Forced and Free-to-Roll Delta Wing Oscillations," AIAA Paper 94-1884, 12th AIAA Applied Aerodynamics Conference, Colorado Springs, June 20-22, 1994.

126. Kandil, O., Kandil, H., and Kalisch, M., "Unsteady Transonic Flow Around a Delta Wing Undergoing Pitching Oscillation," AIAA Paper 94-1887, 12th AIAA Applied Aerodynamics Conference, Colorado Springs, June 20-22, 1994.

127. Bennett, R. M., Eckstrom, C. V., Rivera, J. A., Jr., Dansberry, B. E., Farmer, M. G., and Durham, M. H., "The Benchmark Aeroelastic Models Program — Description and Highlights of Initial Results," In: Transonic Unsteady Aerodynamics and Aeroelasticity, AGARD CP-507, March 1992.

128. Edwards, J. W., "Transonic Shock Oscillations Calculated with a New Interactive Boundary-Layer Coupling Method," AIAA Paper 93-0777, January 1993.

129. Radespiel, R., Rossow, C., and Swanson, R. C., "An Efficient Cell-Vertex Multigrid Scheme for the Three-Dimensional Navier-Stokes Equations," AIAA Paper 89-1953-CP, AIAA 9th Computational Fluid Dynamics Conference, Buffalo, NY, June 13–15, 1989.

130. Jameson, A., Schmidt, W., and Turkel, E., "Numerical Solutions of the Euler Equations by Finite-Volume Method Using Runge-Kutta Time-Stepping Schemes," AIAA Paper 81-1259, AIAA 14th Fluid and Plasma Dynamics Conference, Palo Alto, 1981.

131. Jameson, A., "Time Dependent Calculations Using Multigrid with Applications to Unsteady Flows Past Airfoils and Wings," AIAA Paper 91-1596-CP, AIAA 10th Computational Fluid Dynamics Conference, Honolulu, Hawaii, June 24–26, 1991.

132. Baldwin, B. S., and Lomax, H., "Thin Layer Approximation and Algebraic Model for Separated Turbulent Flows," AIAA Paper 78-257, January 1978.

133. Prichard, D. E., "Development of a Full Potential Solver for Rotor Aerodynamics Analysis," Ph.D. dissertation, Georgia Institute of Technology, May 1990.

134. Holst, T., and Ballhaus, W. F., "Fast Conservative Schemes for the Full Potential Equation Applied to Transonic Flows,"*AIAA Journal*, Vol. 17, No. 2, February 1979, pp. 145–152.

135. Stone, H. L., "Iterative Solution of Implicit Approximations of Multidimensional Partial Differential Equations," *SIAM Journal of Numerical Analysis*, Vol. 5, No. 3, September 1968.

136. Mazaheri, K., and Roe, P. L., "New Light on Numerical Boundary Conditions," AIAA Paper 91-1600-CP, AIAA 10th Computational Fluid Dynamics Conference, Honolulu, Hawaii, June 1991.

137. Mello, O. A. F., and Sankar, L. N., "A Hybrid Navier-Stokes/Full-Potential Method for the Prediction of Iced Wing Aerodynamics," AIAA Paper 94-0489, AIAA 32nd Aerospace Sciences Meeting, Reno, Nevada, January 1994.

138. Engquist, B., and Majda, A., "Absorbing Boundary Conditions for the Numerical Simulation of Waves," *Mathematics of Computation*, Vol. 31, No. 139, July 1977, pp. 629–651.

139. Hedstrom, G. W., "Nonreflecting Boundary Conditions for Nonlinear Hyperbolic Systems," *Journal of Computational Physics*, Vol. 30, 1979, pp. 222–237.

140. Gustafsson, B., and Kreiss, H.-O., "Boundary Conditions for Time Dependent Problems with an Artificial Boundary," *Journal of Computational Physics*, Vol. 30, 1979, pp. 333–351.

141. Rudy, D. H., and Strikwerda, J. C., "A Nonreflecting Outflow Boundary Condition for Subsonic Navier-Stokes Calculations," *Journal of Computational Physics*, Vol. 36, 1980, pp. 55–70.

142. Engquist, B., and Majda, A., "Numerical Radiation Boundary Conditions for Unsteady Transonic Flow," *Journal of Computational Physics*, Vol. 40, March 1981, pp. 91–103.

143. Bayliss, A., and Turkel, E., "Outflow Boundary Conditions for Fluid Dynamics," *SIAM Journal of Scientific and Statistical Computing*, Vol. 3, No. 2, 1982, pp. 250–259.

144. Bayliss, A., and Turkel, E., "Far Field Boundary Conditions for Compressible Flows," *Journal of Computational Physics*, Vol. 48, 1982, pp. 182–199.

145. Thomas, J. L., and Salas, M. D., "Far-Field Boundary Conditions for Transonic Lifting Solutions to the Euler Equations," *AIAA Journal*, Vol. 24, No. 7, July 1986, pp. 1074–1080.

146. Thompson, K. W., "Time Dependent Boundary Conditions for Hyperbolic Systems," *Journal of Computational Physics*, Vol. 68, 1987, pp. 1-24.

147. Roe, P. L., "Remote Boundary Conditions for Unsteady Multidimensional Aerodynamic Computations," *Computers & Fluids*, Vol. 17, No. 1, 1989, pp. 221–231

148. Giles, M., "Nonreflecting Boundary Conditions for Euler Equation Calculations," *AIAA Journal*, Vol. 28, No. 12, December 1990, pp. 2050–2058.

149. Giles, M., "Quasi-3-D Non-Reflecting Boundary Conditions for Euler Equations Calculations," AIAA Paper 91-1603-CP, AIAA 10th Computational Fluid Dynamics Conference, Honolulu, Hawaii, June 1991.

150. Karni, S., "Accelerated Convergence to Steady State by Gradual Far-Field Damping," AIAA Paper 91-1604-CP, AIAA 10th Computational Fluid Dynamics Conference, Honolulu, Hawaii, June 1991.

151. Bragg, M. B., and Khodadoust, A., "Effect of Simulated Glaze Ice on a Rectangular Wing," AIAA Paper 89-0750, January 1989.

152. Khodadoust, A., and Bragg, M. B., "Measured Aerodynamic Performance of a Swept Wing with a Simulated Ice Accretion," AIAA Paper 90-0490, January 1990.

153. Khodadoust, A., "An Experimental Study of the Flowfield on a Semispan Rectangular Wing with a Simulated Glaze Ice Accretion," Ph.D. Thesis, University of Illinois at Urbana-Champaign, 1993.

154. Obayashi, S., Guruswamy, G. P., and Goorjian, P. M., "Streamwise Upwind Algorithm for Computing Unsteady Transonic Flows Past Oscillating Wings," *AIAA Journal,* Vol. 29, No. 10, October 1991.

VITA

Olympio Achilles de Faria Mello was born in Santiago, Rio Grande do Sul, Brazil, on April 16, 1961. He is the son of Guilherme Achilles de Faria Mello and Ana Freitas de Achilles Mello. He graduated from Colégio Impacto Tijuca (high school) in 1978. In 1981, during his undergraduate studies, he joined the Brazilian Air Force, where he has currently the rank of Captain. He received his Bachelor's degree in Aeronautical Engineering from Instituto Tecnológico de Aeronáutica, in São José dos Campos, São Paulo, Brazil, in December, 1983, and subsequently started working in the Aeronautical Division of the Institute of Research and Development of the Brazilian Aerospace Technical Center (CTA), in São José dos Campos. In 1984 he was certified as Helicopter Receiving Engineer by the Flight Test Division of the CTA. He received his Master of Science in Aerospace Engineering degree from the University of Maryland at College Park in August, 1988 and subsequently returned to his position at the CTA. In August, 1990 he returned to the University of Maryland at College Park to continue his graduate studies, and moved to Georgia Tech in September, 1991, where he received his second Master of Science in Aerospace Engineering degree in June, 1993. He is married to Valéria Arantes Achilles de Faria Mello. Their son, Guilherme, was born in Atlanta, Georgia, on February 25, 1993.